DISSERTATION

DEVELOPMENT OF A HIGH POWER CHIRPED PULSE AMPLIFICATION LASER FOR DRIVING SECONDARY SOURCES

Submitted by

Cory M. Baumgarten

Department of Physics

In partial fulfillment of the requirements

For the Degree of Doctor of Philosophy

Colorado State University

Fort Collins, Colorado

Summer 2019

Doctoral Committee:

Advisor: Jorge Rocca

Jacob Roberts
Siu Au Lee
Mario Marconi

ABSTRACT

DEVELOPMENT OF A HIGH POWER CHIRPED PULSE AMPLIFICATION LASER FOR DRIVING SECONDARY SOURCES

Laser applications which require high energy ultrashort laser pulses have been limited in repetition rate. This dissertation describes the development of high repetition rate, high energy, all diode pumped ultrashort pulse Yb:YAG lasers and their use in two selected applications. Yb:YAG is an attractive gain medium for high average power, ultrashort pulse laser operation. This material, with long upper level lifetime, is well suited for direct pumping by high power, narrow bandwidth laser diodes, and combined with a small quantum defect, minimal heating of the material is produced. Additionally, the thermal conductivity and optical properties of Yb:YAG dramatically improve when cooled to cryogenic temperatures. The main focus of this dissertation is the development of an all diode-pumped, chirped pulse amplification, ultrashort pulse laser based on a cryogenically-cooled Yb:YAG amplifier design. This laser system operates at λ = 1.03 μm and is capable of producing 1.4 J pulses before compression at 500 Hz and 1 kHz repetition rate. During 500 Hz operation, the laser used a combination of room temperature and cryogenically-cooled Yb:YAG amplifiers to generate pulses of 1 J energy compressed to sub-5ps duration. At 1 kHz, pulse energies of 1 J with sub-10ps transform limited pulse durations were obtained. The simultaneously high pulse energies and repetition rates obtained in this work will be beneficial for a host of applications including tabletop sources of coherent short wavelength radiation, high power femtosecond sources operating in the near and mid-infrared, and high gradient laser plasma accelerators. The work in this dissertation specifically demonstrates the use of cryogenically cooled Yb:YAG lasers in the development of soft x-ray lasers and a near-infrared optical parametric amplifier for the testing damage threshold of multilayer coatings.

The generation of coherent radiation in the soft x-ray regime was historically limited to 10 Hz. Compact, table-top soft x-ray lasers have enabled a range of applications including nano-scale imaging and lithography, the investigation of hot dense plasmas, and nano-scale fabrication. Recently, compact sources of coherent soft x-ray laser radiation were demonstrated at repetition rates of one hundred shots per second using the laser technology described in this dissertation. As a demonstration of the Yb:YAG laser's excellent beam quality and high average power, this system was used to pump a high repetition rate soft x-ray laser. The optical pump laser and the resulting soft x-ray laser, operated at a record 400 Hz repetition rate with strong lasing in the λ = 18.9 nm line of Ni-like Mo.

This work also demonstrates a Yb:YAG laser driven, optical parametric chirped pulse amplification (OPCPA) laser system operating at 100 Hz in the near-infrared, which was used to perform laser induced damage threshold measurements of optical coatings. OPCPAs have emerged as a next generation ultrafast laser source for generating sub-femtosecond laser pulses useful for probing molecular electron dynamics as well as creating ultra-intense, femtosecond laser pulses for exploring exotic states of matter and for the development of next generation laser plasma accelerators. The OPCPA developed as part of this work operates at wavelengths ranging from λ = 1.5-2 μm with final amplification stages pumped at 100 Hz with a chirped pulse amplification laser based on cryogenically-cooled Yb:YAG. The OPCPA was used to obtain damage thresholds of optical coatings in what to our knowledge constitutes the first results of picosecond damage performed in this wavelength range.

TABLE OF CONTENTS

Chapter 1

Introduction

Strickland and Mourou's demonstration of optical chirped pulse amplification (CPA) in 1985 laid the groundwork for the development of ultrafast, high energy lasers. [1] The fundamental concept of CPA is to reduce the laser pulse intensity during the amplification process. This is done by imparting a frequency dependent time delay, called a chirp, to the pulse prior to amplification which temporally stretches the pulse in a controlled manner. The lower pulse intensity during amplification prevents nonlinear, intensity dependent effects from developing which can be detrimental to the integrity of the laser beam and even lead to damage of optical elements within the laser system. After amplification, the chirp is removed from the pulse returning the initial short pulse duration.

Shortly after the first demonstration of CPA, the spectroscopic and lasing characteristics of Ti:Al_2O_3 were first reported. [2] The material boasts a high stimulated emission cross section and broad bandwidth allowing for amplification to high pulse energies and ultrashort pulse durations. In 1999, the CPA scheme was used in conjunction with the favorable properties of Ti:Al_2O_3 to produce a laser system with a peak power greater than a petawatt (PW). [3] Since this demonstration, the number of PW class lasers has proliferated [4] with many groups using Ti:Al_2O_3 reporting multi-PW operation [5–8]. Many of these systems are only capable of single shot operation, yet a higher photon flux is needed for many applications to be viable [9]. Recently, progress has been made to increase the average power of Ti:Al_2O_3 based lasers, with repetition rates >1 Hz and PW-class pulse intensities having been reported [10–12].

The difficulty in producing simultaneously high pulse energy and repetition rates stems from the pump lasers necessary to supply energy to the Ti:Al_2O_3 gain medium. As a consequence of the high stimulated emission cross section and broad emission bandwidth, Ti:Al_2O_3 has a short upper level lifetime and energy has to be supplied by a bright, short pulse pump laser. This pump source is typically a flash lamp pumped Nd:glass system whose output is

frequency doubled to well match the peak absorption wavelength of Ti:Al_2O_3 around λ = 500 nm. The broadband flash lamps produce significant thermal loading in the host material and the poor thermal conductivity of glass prevents the efficient dissipation of heat. These factors therefore limit the repetition rate of the whole system.

High power laser diodes provide a more efficient means of pumping high average power solid state lasers. Laser diodes provide narrow bandwidth pumping that is well matched to the upper laser manifold of Yb-doped solid-state laser gain media, resulting in minimal excess heating from unabsorbed pump light. These pump sources are low peak power when compared to flash lamps and require a laser material with a long upper level lifetime to efficiently store energy. Yb:YAG has emerged in recent decades as a gain material that is well suited for high power short pulse laser operation due to its long upper level lifetime (~1 ms) and its absorption band which is suitable for λ = 940 nm diode laser pumping. In addition, its material properties allow for efficient heat removal with minimal thermo-optic distortions.

Figure 1.1 shows the current state of high average power, high energy, short pulse, diode pumped Yb-doped lasers around the time when the work of this thesis was conducted. The graph shows the results of diode pumped laser systems operating at $\lambda \approx 1$ μm, with energies >10 mJ, repetition rates >10 Hz, and transform limited pulse durations below 10 ps. It can be seen that tremendous progress has been made in picosecond to femtosecond lasers with pulse energies in the tens to hundreds of millijoule range and average powers of up to 1 kW, and these results were obtained using a variety of different schemes. A popular and successful geometry is the room temperature, thin-disk active mirror design, which was first applied to diode-pumped solid-state lasers in 1994. [35] Recently, this scheme has been used in a regenerative amplifier ring cavity producing pulse energies as high as 200 mJ at a repetition rate of 5 kHz [26] and when used in a multi-pass amplifier has achieved 600 mJ at 1 kHz repetition rate [30]. Other geometries include the coherent combination of Yb-doped fibers which has produced 12 mJ pulse energies with 700 W of average power [36] as well as 2.3 mJ with 1.83 kW of average power [37], the Innoslab geometry which has reported 54 mJ energy at 10 kHz [29], and cryogenic-

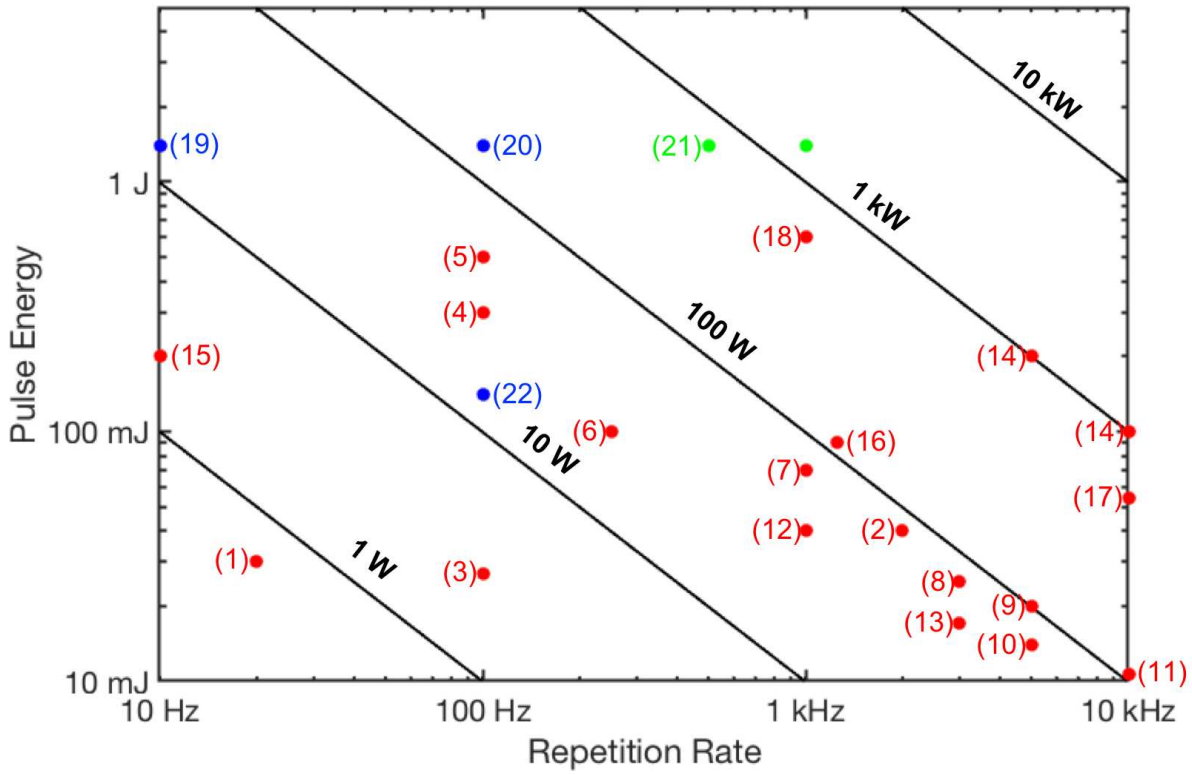

Figure 1.1: A summary of diode-pumped Yb-doped lasers at $\lambda \approx 1$ µm with high pulse energy (>10 mJ), repetition rate (>10 Hz), and pulse durations compressible to sub-10 ps. Red indicates work reported elsewhere, blue indicates previously reported work from Colorado State University's cryogenically-cooled Yb:YAG laser, and green indicates the work presented in this dissertation. (1): [13], (2): [14], (3): [15], (4): [16], (5): [17], (6): [18], (7): [19], (8): [20], (9): [21], (10): [22], (11): [23], (12): [24], (13): [25], (14): [26], (15): [27], (16): [28], (17): [29], (18): [30], (19): [31], (20): [32], (21): [33], (22): [34]

cooling [18, 22, 28, 33] which is the focus of the work presented in this dissertation. Many of these schemes use Yb:YAG as the lasing medium, but other host materials such as Yb:YLF [13], Yb:KYW [38], and Yb:CaF_2 [39,40] which support broader bandwidths and thereby shorter pulse duration are also being pursued for high power operation.

Scaling to higher pulse energy while maintaining high average power by using diode pumped ultrafast lasers is of interest not only for the applications discussed in the following sections, but will be a key technology for enabling numerous scientific, medical, and industrial applications. [9, 41, 42] While many of the techniques for producing energetic photons, isotopes, and neutrons have been demonstrated in current high energy, low repetition rate laser systems, new

high average power ultrafast lasers will make these applications viable by providing a higher flux of photons and energetic particles. This will make materials processing, x-ray imaging procedures, and medical therapies time and cost efficient, and will ease experimental stability requirements by decreasing data acquisition times. Beyond these goals, higher repetition rates provide new opportunities for incorporating machine learning to provide feedback in experiments with high energy lasers. [41, 43] Not only can this feedback be used to maintain the long-term stability of the laser system or experiment, but it provides the potential to efficiently optimize experiments over large parameter spaces.

Diode pumped ultrafast lasers, such as the one described in this dissertation, are of interest for applications including the tabletop generation of coherent soft x-ray radiation via plasma-based lasers, high harmonic generation (HHG), and potentially free electron lasers (FEL) [44]. Other uses include compact, high gradient laser plasma accelerators (LPA) as well as high power optical parametric chirped pulse amplification (OPCPA) lasers for use in spectroscopy and HHG. The generation of high repetition rate, plasma based soft x-ray lasers (SXRL) and LPAs for next generation electron accelerators will be expanded upon in Section 1.1.2 and Section 1.1.4 respectively. OPCPA and its applications will be briefly discussed in Section 1.1.3 while a more detailed description of optical parametric amplification will be presented in Chapter 3.

The work presented in this dissertation describes a CPA laser capable of producing >1 J of pulse energy at a repetition rate of 500 Hz with a pulse duration below 5 ps. This system was expanded to obtain joule-level energies at 1 kHz and initial results are presented with stable long duration operation expected soon. The approach for achieving >1 J, picosecond pulses at kHz-level repetition rates utilizes a cryogenically-cooled, thick-disk Yb:YAG active mirror multi-pass amplifier. This design takes advantage of the enhanced material and spectroscopic properties of Yb:YAG when cooled to cryogenic temperature while maintaining the efficient heat removal characteristic of thin-disk amplifiers. This CPA laser was used to demonstrate soft x-ray lasing at λ = 18.9 nm in Ni-like Molybdenum at a repetition rate of 400 Hz. Additionally, an earlier 100 Hz version of this laser was used as the pump source for a near-infrared OPCPA laser which was

tunable from λ = 1.5 - 2 μm and was used to perform laser induced damage testing (LIDT) of optical coatings at λ = 1.6 μm.

1.1 Motivating Applications

The technological advancements provided by high power short pulse lasers are important for the development of various scientific applications. Some of these have already been realized, including the generation of high power, coherent soft x-ray radiation from tabletop systems as well as powerful femtosecond sources in the near and mid-infrared. While others, like high gradient laser plasma accelerators, are still in the early stages of development and require further progress of laser technology to become operational.

1.1.1 Soft X-ray Sources

The numerous absorption features in the spectral region of the ultraviolet through the x-ray has made it difficult to access due to the short penetration depth of radiation in this wavelength regime. Because of these absorption resonances and the efficiency of photo-absorption at these wavelengths, coherent sources of extreme ultraviolet (EUV) and soft x-ray radiation are excellent tools for the spectroscopic study of elements and molecules. While no consensus exists on the exact definitions of EUV and soft x-ray, Atwood defines EUV to be photon energies of 30 eV to 250 eV (~40 nm to ~5 nm) and soft x-rays as extending from 250 eV to several keV (~5 nm to ~0.3 nm). [45] Furthermore, the radiation's short wavelength allows for microscopy and lithography of small-scale features and is well understood by considering the Rayleigh criterion for an imaging optic

$$R_{Rayl.} = \frac{0.61\lambda}{NA} \tag{1.1}$$

where NA is the numerical aperture of the objective. From this criterion, the direct relation between feature resolution and the wavelength of the illumination source can clearly be seen. For this reason, manufacturers of next generation microprocessors have begun utilizing EUV sources for their lithographic processes. When this small spatial resolution is combined with

ultrafast time durations, on the order of femtoseconds to attoseconds, it is possible to probe molecular and even electron dynamics. [46–48]

To obtain radiation at these EUV and soft x-ray wavelengths there exist large, facility sized sources, such as synchrotrons and FELs. In synchrotrons, radiation is generated by relativistic electrons moving in a circular path. This radiation is emitted as a broad bandwidth cone of light tangential to the direction of acceleration. Initially, this radiation was simply seen as a source of power loss in early accelerators, but quickly the value of such high flux x-ray sources was realized. Today's 3rd generation synchrotrons are dedicated user facilities that incorporate a number of features, such as straight sections with additional magnetic components like undulators or wigglers, to improve the output radiation's coherence or increase photon energy. The radiation emitted can be filtered to make it more spatially coherent and monochromatic, providing a tunable high power source of x-rays. FELs are another facility sized source of coherent x-ray radiation. FELs use a linear accelerator to create a beam of energtic electrons which then pass through either an undulator or wiggler which impart a periodic magnetic field. Injected electrons oscillate and emit photons which are in phase with the oscillating electrons, yielding a coherent beam of x-rays. FELs are tunable and produce high brightness sources of coherent x-rays. Due to the cost and scale of synchrotrons and FELs there are a small number of these facilities with limited user access.

Alternative approaches for EUV and soft x-ray generation are laboratory scale sources which include HHG and laser driven SXRLs. In HHG, a femtosecond laser pulse is focused in a target, usually a neutral gas cell, where a nonlinear interaction occurs between the laser electric field and the atoms. This generates photons whose frequencies are odd integer multiples of the driving laser frequency and are spatially and temporally coherent. The resulting spectrum is a broad "comb" of individual frequencies ranging from the driving laser's frequency up to the cutoff frequency which is characterized as [49]

$$E_c = I_p + 3.17U_p \tag{1.2}$$

where I_p is the ionization potential of the atom and U_p is the ponderomotive energy, which is proportional to $I\lambda^2$ with I being the laser intensity and λ being the center wavelength of the laser. It can be seen that increasing the laser wavelength extends the cutoff to higher energies allowing for broader spectrums with shorter wavelengths. The desire for higher average power HHG sources with cutoff energies in the EUV regime has spurred the development of intense femtosecond lasers in the mid-infrared (MIR) using techniques like OPCPA.

Another approach to generating short wavelength radiation in a laboratory environment is through laser driven, plasma based SXRL. The first lasers generated with this technique used extremely powerful, facility sized lasers, but in recent decades numerous techniques have been developed to improve the conversion efficiency of drive laser energy into SXRL energy. This has produced compact, tabletop SXRL sources. These lasers typically are much more monochromatic and have higher pulse energies than those generated via HHG but don't obtain as short of pulse durations and operate at lower repetition rates. While many methods exist for laser driven, plasma based soft x-ray lasers including recombination and photoionization, the most successful method is electron impact excitation.

1.1.2 Collisionally Pumped Soft X-Ray Lasers

Electron impact excitation at EUV and soft x-ray wavelengths operate analogously to common ion lasers in the visible wavelength regime such as Argon and Krypton ion lasers. In the case of the Argon ion laser, an Argon atom is first singly ionized by an intense electric discharge and then excited to the upper energy levels from the ground state by collisions with free electrons. A population inversion is created when the upper laser levels have a much longer radiative decay time than the lower laser levels, and the system forms a three level laser. While most lasers in the visible and near infrared (NIR) have excitation energies on the order of a few eV, SXRLs operate on transitions greater than 30 eV, much greater than the ionization potential of a neutral atom. This means that laser action at these short wavelengths will occur with ions which have an energy level structure that allows transitions at higher energies. If electron exci-

tation is to occur through collisions with energetic free electrons, then it is necessary to create an environment which has a high density of free electrons with energies greater than the excitation energy of the ion. This suggests use of hot dense plasmas, and most atomic SXRLs are generated in this environment. Given that these plasmas rapidly expand and cool, their gain is very short lived. Furthermore, there are no high reflective mirrors in this wavelength regime which precludes the use of a resonator cavity to build pulse energy. For these reasons, nearly all SXRLs operate with amplification of spontaneous emission in a single or double pass. To efficiently utilize this mode of operation, the plasma is formed into a column with a high aspect ratio, i.e. the length is much larger than the width. Throughout the plasma, radiation is emitted spontaneously, but at one end, some amount of radiation will be directed along the length of the column. This radiation will lead to stimulated emission along the plasma length. Using this geometry, gain saturation can be achieved.

To generate SXRLs from outer shell electrons, highly ionized atoms exhibit the energy level structure necessary for high energy laser transitions. In particular, ions with closed shell electron structures are favored as they are most abundant over wide range of conditions. The two most investigated ion states being the n = 3, 10 electron ions and the n = 4, 28 electron ions, where n is the principal quantum number. These states are referred to as the neon-like (Ne-like) and nickel-like (Ni-like) states respectively. These particular ionization states are preferred because the closed nature of the electron shell at these points creates an "ionization bottleneck" in which substantially more energy is required to remove the next electron from the ion. As an example, we can consider the ionization energy necessary to remove one electron from a selenium ion in the 11 electron, Na-like state and the 10 electron, Ne-like state. The former has an ionization energy of 1036 eV while the latter has an energy of 2540 eV. Therefore, by selecting an electron temperature near 1 keV a large fraction of the ions will be in the desired Ne-like state from which collisions with free electrons will create a population inversion.

The first demonstrations for using an optical laser to obtain inversion in a Ne-like plasma were reported from Lawrence Livermore National Laboratory in 1985. [50, 51] In this experi-

ment, the kilojoule class Novette laser was frequency doubled to λ = 527 nm, and two 450 ps laser pulses were focused onto a selenium foil to a cylindrical focal spot that measured 200 μm wide by 2.2 cm long with an intensity 5 x 10^{13} W/cm^2. This ionized the selenium atom 24 times to a Ne-like ion and produced gain at two transitions, λ = 20.64 nm and 20.98 nm, with a gain-length product of 5.5 ± 1.0 cm^{-1}. In a Ne-like plasma, lasing is obtained between the $2p^5 3p$ upper laser level and $2p^5 3s$ lower level. Inversion occurs due to monopole electron impact excitation between the $2p^5 3p$ and $2p^6$ ground state and radiative decay to the ground state is dipole forbidden, while the $2p^5 3s$ to $2p^6$ transition is radiatively allowed and has a short lifetime. These initial SXRLs used nanoseconds long pulse durations and energies in excess of several hundred joules. [52, 53] In order to obtain soft x-ray lasing with more modest tabletop optical lasers a number of schemes were developed to improve efficiency. These include the use of the Ni-like isoelectric sequence to scale to shorter wavelengths with less pulse energies, a pre-pulse to separate the plasma formation from the plasma heating, transient collisional excitation to obtain substantially higher gain, and grazing incidence pumping to deposit optical laser energy in the optimal plasma density region.

To produce shorter wavelengths and decrease pulse energy requirements, collisional pumping of Ni-like ions was explored. [56, 57] Ni-like ions have an advantage over Ne-like ions due to the lower ionization potential associated with the n = 4 closed shell configuration in nickel versus the n = 3 configuration in neon. Figure 1.2 shows the wavelength as a function of ionization degree for the Ni-like (blue) and Ne-like (red) isoelectronic sequences. [54, 55] The figure shows a scaling to shorter wavelengths quicker in the Ni-like series, and as such, was chosen as a path to obtain shorter wavelengths. Figure 1.3a shows the energy level structure of molybdenum 14 times ionized. While the degree of ionization and lasing wavelength indicated are specific to Mo 14^+ the energy level structure is the same for all Ni-like ions. Here, $3d^{10}$ level forms the ground state while lasing occurs between the $3d^9 4d$ and $3d^9 4p$ excited states, and wavelength scaling in the Ni-like series has been used to demonstrate lasing down to λ = 3.56 nm in Ni-like Au. [58]

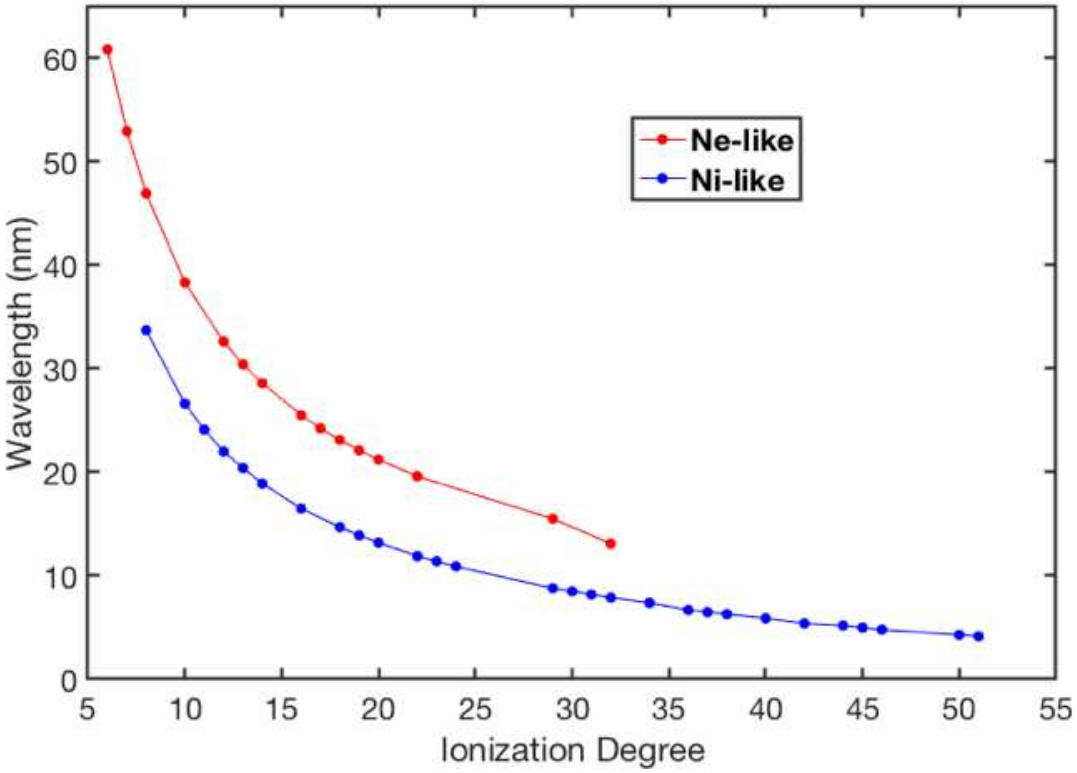

Figure 1.2: Plot of laser wavelength as a function of ionization degree for the 3p to 3s transition in Ne-like ions (red) and the 4d to 4p transition in Ni-like ions (blue). Based on data from [54, 55]

Scaling to shorter wavelengths was also advanced by implementing a pre-pulse technique in which the excitation process is divided into two parts, plasma formation and heating. In this process, the plasma is first formed by an initial pulse which ablates the target and allows the plasma to expand. This is followed several nanoseconds later by a main pulse which then heats the plasma and creates the conditions necessary for laser action. To appreciate the value of this technique, it is important to understand the role of refraction effects on SXRLs. The index of refraction of a plasma can be described by the following equation

$$\eta = \sqrt{1 - \frac{n_e}{n_c}} \tag{1.3}$$

where n_e is the electron density and n_c is the critical density which is defined as

$$n_c = \frac{4\pi^2 \epsilon_0 m_e c^2}{e^2 \lambda^2} \tag{1.4}$$

where ϵ_0 is the permittivity of free space, m_e is the electron mass, e is the electron charge, and λ is driving laser wavelength.

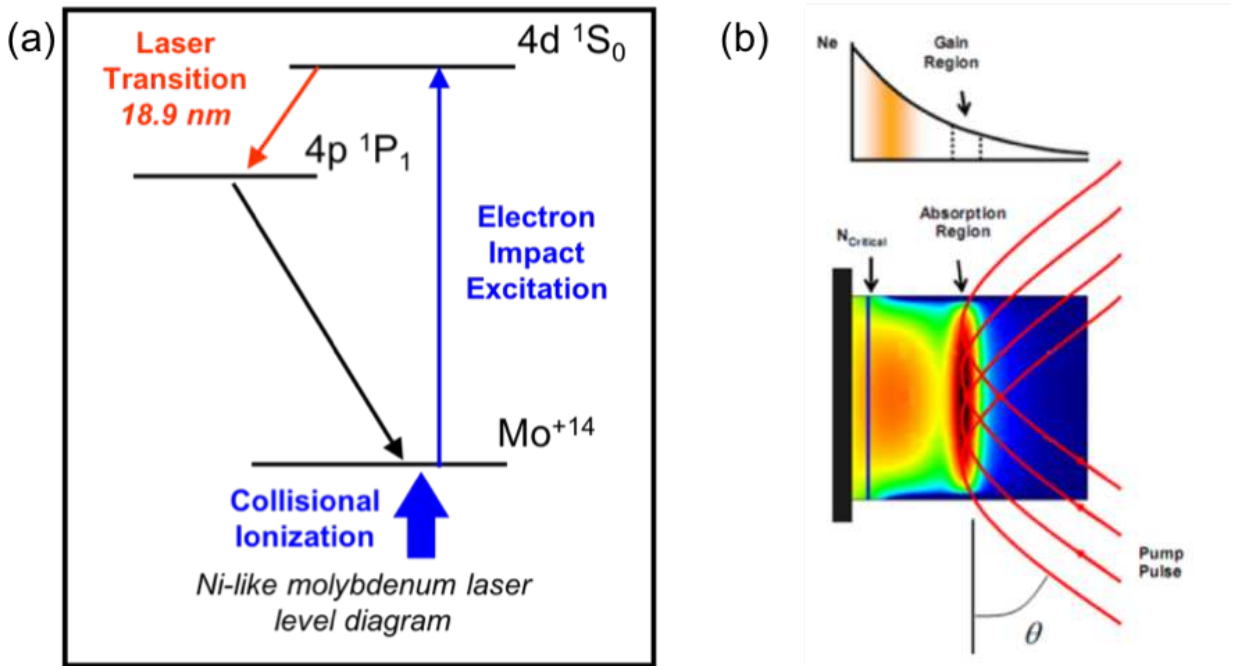

Figure 1.3: a) the excited state energy levels for a 14 times ionized, Ni-like molybdenum ion. b) shows the electron density profile as a function of distance from the target (top) and the geometry of a grazing incidence pumping scheme (bottom)

In [59], London approximated the electron density to decrease parabolically in the direction of plasma expansion. This matches well with measured electron density profiles, and is shown at the top of Figure 1.3b. For a driving laser pulse incident on a slab target at normal incidence, plasma expansion occurs predominantly in the direction normal to the target surface and the majority of optical laser energy is deposited near the critical density.

From equation (1.3), this electron density distribution creates an index profile at a minimum near the critical density and increases with distance from the target surface with the steepest index gradients near the critical density where energy deposition is greatest. This causes x-ray

radiation to refract out of the high gain plasma column before significant amplification can be achieved. Nilsen et al. made the first use of a pre-pulse pumping scheme to overcome refraction effects. [60] In this demonstration, the Nova laser was used to illuminate the target with a 600 ps FWHM main pulse with 1.1 kJ of energy which was focused to a 120 μm wide by 5.4 cm long line. A 600 ps FWHM, 6 J pulse preceded the main pulse by 4-7 ns. Using this pumping scheme, lasing was observed for the first time in Ne-like chromium and iron. Illumination by a low energy pre-pulse allows the plasma to expand and cool creating a larger, more uniform plasma with lower density and reduced density gradients. Lower densities were necessary for lasing in these elements and the lower gradients reduced losses from refraction, thereby increasing the effective lasing length of the plasma. While the pre-pulse technique allowed experimenters to access more laser transitions and mitigate refraction losses, the pulse energy requirements still inhibited SXRL generation with tabletop optical lasers.

A dramatic decrease in driving laser energy resulted from the implementation of transient collisional excitation. This scheme was first theoretically predicted in Afanas′ev and Shlyaptsev in 1989. [61] They found that in a transient regime (where the characteristic times of the excited state relaxation and ionization are greater than or on the order of the characteristic time of changes in the plasma parameters) a plasma which is rapidly heated can achieve very high gain values, with $g \approx 10^2$ cm^{-1}. In the initial SXRL work described to this point, targets were irradiated with pulses on the order of a nanosecond. This creates a quasi-steady state plasma in which inversion is created by depopulation of the lower laser level. In contrast, inversion in the transient regime occurs by heating the plasma at a rate faster than the upper level relaxation time. This produces a much higher population inversion that lasts for a short period of time before relaxation redistributes the upper level population. To create the conditions for transient inversion, a high energy, ultrashort picoseconds duration pulse is needed to heat the plasma. In 1997, Nickles et al. successfully demonstrated a transient inversion pumping scheme to generate lasing in Ne-like titanium. [62] In this work, experimenters used a 7 J, 1.5 ns pre-pulse to form the plasma and a 4 J, 600 fs heating pulse delayed by 1.5 ns to create a transient pop-

ulation inversion. Amplification was observed with pulse energies as low as 4-6 J in the pre-pulse and 1.5 J in the short heating pulse, and small signal gain coefficients as high as 19 cm^{-1} were reported. This marked a dramatic increase in gain (~7 times higher) from previous experiments [63] that operated in a quasi-steady state regime and saw a significant reduction in pulse energy from the 200-550 J used in [63]. While this work was successful at lowering the lasing threshold for collisionally pumped SXRL by over an order of magnitude, the authors reported that the achievable amplification was still limited by refraction losses.

In pumping schemes which use normally incident laser pulses, a majority of the energy is deposited in the region near the critical density. As a consequence, this region suffers most from refraction losses. In 2003, it was reported that these limitations could be overcome by pumping at grazing incidence. [64] This geometry, illustrated in Figure 1.3b, makes use of the refraction effects present in the plasma to deposit laser energy at an optimal electron density in which high gain can be achieved with minimal refraction loss. This grazing incidence angle can be expressed for small grazing angles as

$$\theta = \sqrt{\frac{n_{em}}{n_c}} \tag{1.5}$$

where θ is the angle between the target and the incident laser radiation, n_c is the critical density, and n_{em} is the density at the turning point of the beam where the majority of energy is deposited. From equation (1.5) it can be seen that by adjusting the incidence angle θ energy can be deposited at different regions of the plasma. Additionally, this pumping scheme inherently accomplishes traveling wave excitation, which is important when the transient excitation time is shorter or on the order of the time it takes soft x-ray radiation to traverse the plasma.

The use of grazing incidence pumping opened the door for efficient soft x-ray lasing with modest pulse energy, tabletop optical lasers. In 2005, Keenan et al. reported lasing at λ = 18.9 nm in Ni-like Mo using a total pump energy of 150 mJ at repetition rate of 10 Hz. [65] In this demonstration, a 70 mJ, 200 ps duration pre-pulse was focused to a 15 μm x 5 mm line at normal incidence onto a molybdenum target. This was followed 500 ps later by an 80 mJ, 1.5 ps heating pulse which was incident on the target at an angle of θ = 14°. A maximum small signal gain

coefficient of 55 cm^{-1} was reported for targets up to 2 mm long with the output energy for longer target lengths indicating saturation like effects. In the same year, researchers at Colorado State University reported fully saturated lasing at λ = 18.9 nm using a total pulse energy of 1.35 J at a repetition rate of 5 Hz. [66] Over the coming years, grazing incidence pumping was used to demonstrate lasing with joule-level pulse energies from tabletop lasers in the Ne-like and Ni-like sequences at wavelengths ranging from λ = 32.6 nm down to 7.36 nm. [67–72] Studies were also conducted to improve the temporal and spatial coherence of these sources by seeding them with high harmonic femtosecond pulses. This resulted in high brightness, temporally and spatially coherent lasers at wavelengths which ranged from λ = 13.2 to 32.6 nm. [73–75]

The high pulse energies available from tabletop SXRLs have enabled numerous applications, including nanoscale imaging [76–78], interferometer of dense plasmas [79], and surface science [80]. Yet other processes such as nanopatterning [81, 82], nanomachining [83], and microscopy all benefit from SXRL sources with high average powers. Therefore, increasing the available photon flux necessitates scaling the driving laser to higher repetition rates while maintaining similarly high, joule level pulse energies. Research at Colorado State University has been leading the development of high average power SXRL. In 2009, lasing at λ = 18.9 nm was demonstrated used an all diode pumped driving laser system at a repetition rate of 10 Hz. [31] This all diode pumping scheme allows for reduced thermal loading of the driving laser gain material and facilitates higher repetition rate operation as opposed to conventional flash lamp pumped systems. Using this high repetition rate pump source, researchers were able to demonstrate stable, long duration SXRL operation. In 2013 hour-long, mW level operation of a 50 Hz, 18.9 nm laser as well as 30-minute operation at 100 Hz were reported. [84] The viability of this system for high power SXRL applications was exhibited by using this coherent source to lithographically print nanoscale features using a Talbot self-imaging technique. This work was further extended in 2016 with a demonstration of an 18.9 nm laser operating at 400 Hz repetition rate [33], and these results are presented in this work.

1.1.3 Optical Parametric Chirped Pulse Amplification

The development of high power CPA lasers is also important for the development of high average power optical parametric chirped pulse amplification (OPCPA) lasers. OPCPA is seen as a valuable tool for its ability to produce intense few cycle pulses and is the basis of many new petawatt (PW) lasers being developed around the world [85, 86] as well as holding the potential for being the next generation of high average power, tabletop femtosecond lasers. [87] This technology incorporates optical parametric amplification (OPA) with the extremely successful CPA technique to produce a broadband, tunable source of ultrafast laser pulses.

The mechanics of OPA are detailed in Section 3.1, but a brief overview of the process is necessary here to understand the benefits high power picosecond Yb:YAG lasers afford. The process is illustrated in Figure 1.4. Here a high energy pump beam and lower energy signal beam are made to interact within a suitable nonlinear crystal. The process is parametric, and therefore, energy is very briefly stored in a virtual energy level under the condition that the quantum state of the system cannot change. As a consequence, energy and momentum must be conserved in this process. By minimizing the mismatch in the momentum of three waves involved in the process, i.e. phase matching, energy can efficiently be converted from a high energy pump photon into two lower energy photons, one at the signal wavelength and another at the so-called idler wavelength. Due to the conservation of energy, this emitted idler photon energy is equal to the difference of the pump and signal photon energies. This process is tunable in that so long as the energy and phase matching conditions are met within the medium, it is possible to amplify and generate beams of varying wavelengths. Due to the instantaneous nature of OPA, the pulses involved must spatially and temporally interact within the crystal, and for efficient amplification, the pump and signal pulses must have similar temporal pulse durations. Therefore, to efficiently amplify a broadband femtosecond laser pulse and avoid optical damage, it is necessary to stretch the pulse in time to match the pulse duration of the pump beam. This process of temporally stretching a short signal pulse, parametrically amplifying this chirped pulse,

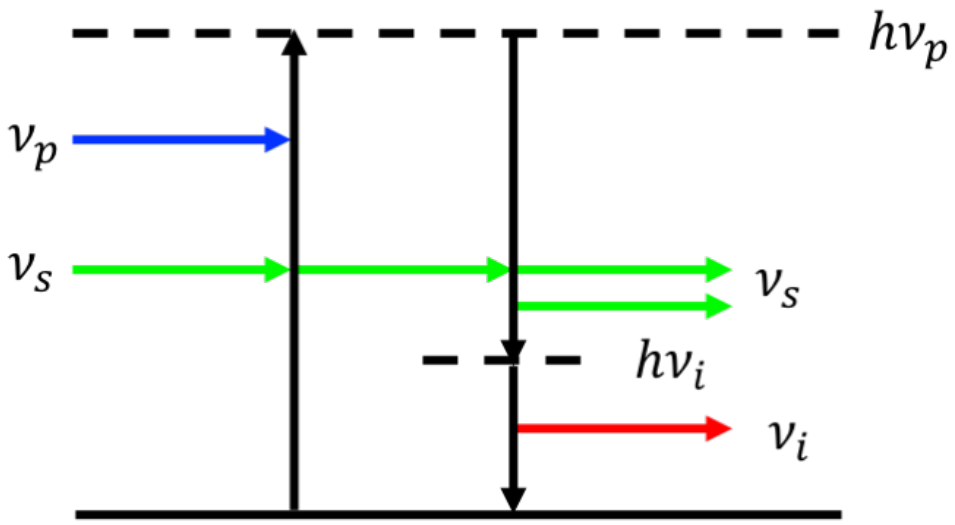

Figure 1.4: An energy level diagram illustrating OPA. A pump photon $h\nu_p$ excites a virtual energy level. In the process, an additional signal photon $h\nu_s$ is emitted in phase with the input signal photon and under conservation of energy and momentum, an idler photon $h\nu_i$ is emitted.

and recompressing to near the transform limit to obtain high peak pulse intensities is called OPCPA.

Many high peak power OPCPAs rely on high energy Nd:glass pump lasers, which after frequency doubling, are used to parametrically amplify pulses in either potassium dihydrogen phosphate (KDP) or lithium triborate (LBO) and are able to capitalize on the broad bandwidths, excellent pulse contrast, and reduced thermal load OPCPA affords to produce high energy laser pulses. While these lasers are extremely successful in achieving high peak powers, they are limited in repetition rate by the Nd:glass laser material. Aside from just obtaining high pulse energies, there exists a desire to leverage the wavelength tunability, broad bandwidth, and low thermal loading of the OPCPA technique to develop lower energy, high average power femtosecond lasers. These systems are of interest for use in ultrafast spectroscopy [88–90] as well as for scaling HHG to higher average power and extending its cutoff energy to the soft x-ray regime by developing MIR OPCPAs [91–93]. These higher average power OPCPAs require a similarly high average power pump laser, and the development of high power picosecond Yb based CPA lasers has been identified as a key technology for the advancement of high power OPCPA lasers, which are seen as the next generation of femtosecond laser technology. [87] Conventionally,

pump pulses with durations of hundreds of picoseconds have been used in this type OPCPA laser, but Fattahi et al. identified key advantages of using near-1-ps duration pump pulses in the amplification process. [87] Because the interaction process scales with the pump intensity, the use of shorter pump pulses increases the gain of these amplifiers and reduces the length of the crystals used. This has the added benefit of simplifying the pulse stretching and compression inherent in CPA, limits dispersion in the material, and improves pulse contrast.

Due to the benefits outlined above, a tunable OPCPA laser was developed by our group to investigate optical coatings at 1.6 μm. This wavelength range is of interest for the development of eye safe, high power lasers but no work has currently been published concerning the performance of multilayer dielectric coatings at this wavelength. This system was used to perform laser induced damage testing of specially designed high reflective (HR) and antireflective (AR) optical coatings. Full details of this laser system and optical coating damage results are the focus of Chapter 3.

1.1.4 Laser Plasma Accelerators

The technology gained in the development of high power ultrafast lasers will be crucial for the next generation of high gradient particle acclerators. Current particle accelerators are reaching a scaling limit in which the economic costs outweigh the potential for new physics. Synchrotron colliders such as the 26.7 km circumference Large Hadron Collider (LHC) rely on powerful superconducting magnetics to collide groups of protons or heavy ions in counter-propagating circular paths. Linear particle accelerators such as the 2-mile-long Stanford Linear Accelerator Center (SLAC) accelerate particles using oscillating electric potentials. Both of these technologies are ultimately limited by their achievable acceleration gradient. Hence their scale (and cost) must increase in size to enable the higher particle energies necessary for probing new physics. Therefore, an alternative to constructing ever larger colliders is to pursue schemes with the potential for higher acceleration gradients.

Laser Plasma Acceleration (LPA) has emerged in recent decades as a powerful alternative to conventional accelerator technologies. In 1979, Tajima and Dawson proposed a novel way of accelerating electrons which involved using an intense laser pulse to generate a periodic electron density within a plasma. [94] In this scheme, an intense electromagnetic pulse is injected into a plasma waveguide, which can be generated by ionizing hydrogen or helium inside a gas-filled capillary discharge waveguide. This intense laser pulse causes the electrons to move out of the beam path, and, as ions are much more massive, their position is left relatively unchanged. This creates regions of oscillating electron density known as a laser wake or plasma wave which oscillates at the plasma frequency which is defined as

$$\omega_p = \sqrt{\frac{e^2 n_e}{\varepsilon_0 m_e}} \tag{1.6}$$

where e is the electron charge, n_e is the electron density, ε_0 is the permittivity of free space, and m_e is the electron mass. The resulting electric field used for accelerating electrons generated by the plasma oscillations is

$$E_0 = \frac{c m_e \omega_p}{e} \tag{1.7}$$

For typical electron densities of $\sim 10^{18}$ cm^{-3}, this yields an accelerating electric field on the order of 100 GV/m, which is three orders of magnitude greater than what can be achieved with conventional radio frequency (RF) linear accelerators. With a high intensity laser pulse and proper plasma conditions, the ponderomotive force of the laser pulse can deflect all electrons transversely out of the beam path, resulting in an ion cavity behind the pulse which is completely devoid of electrons. [96] The electrons form a sheath around this cavity which is why this operation regime is commonly referred to as the "bubble" regime. The trajectories of some of the electrons surrounding the ion cavity can penetrate the barrier and experience a large accelerating force. If they gain sufficient energy, they will become trapped and be further accelerated by the field. These electrons are referred to as self-trapped electrons. By seeding electrons into the wakefield with the proper phase, it is possible to accelerate these electrons to relativistic

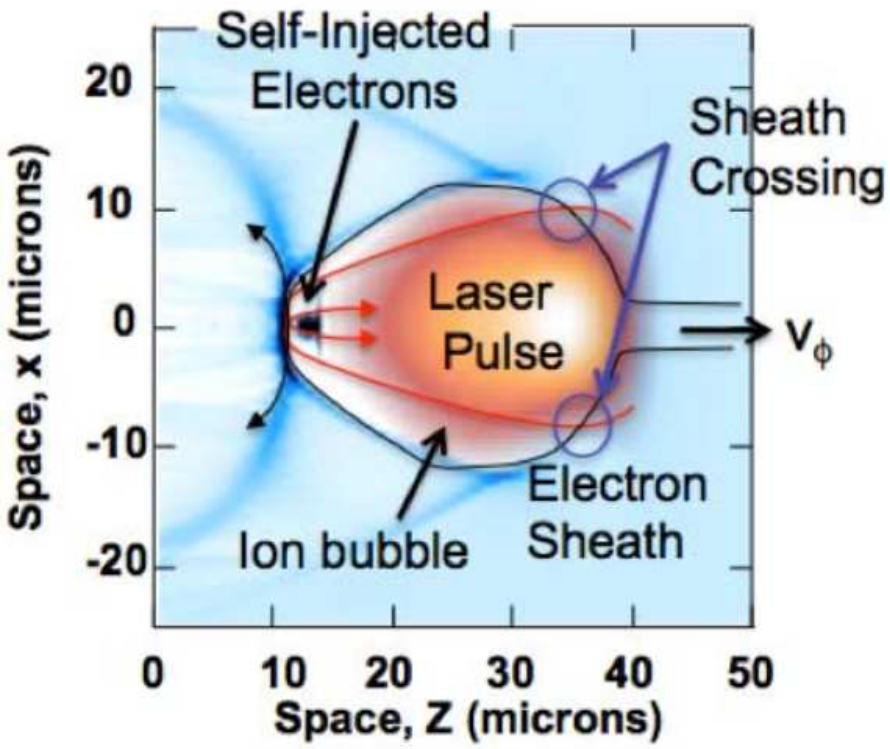

Figure 1.5: Image showing a laser wakefield plasma in the "bubble" regime. (from [95])

velocities in interactions lengths a fraction of the size of today's RF accelerators. To date accelerated electron energies up to 7.8 GeV have been achieved using LPA techniques [97], and with the hope for more compact particle accelerators, an intense effort has begun to develop the next generation light source to enable high brightness accelerators based on LPA. [98]

This high brightness requirement necessitates laser systems with simultaneously high pulse intensities and average powers, and many design architectures have been proposed to reach these goals, including a Tm:YLF based femtosecond laser system [98, 99], the coherent combination of many high power fibers [98, 100], and a Colorado State University (CSU) led high power Ti:Sapphire system. [98] Figure 1.6 illustrates the CSU design for a joule-level, kilohertz repetition rate, femtosecond duration, Ti:Sapphire based system proposed to meet the near term laser requirements for LPA. Here, a 1 J, 1 kHz cryogenically cooled bulk Yb:YAG laser, could be used to seed two high power cryogenically-cooled, thick-disk active mirror bulk Yb:YAG amplifiers, similar to the ones presented in Section 2.5, to produce a combined 10 J pulse energy.

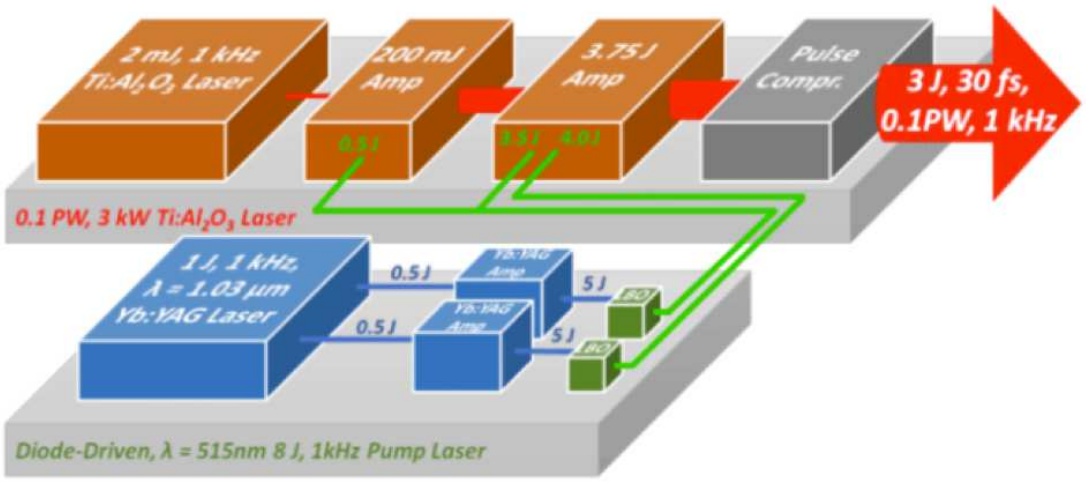

Figure 1.6: A conceptual schematic of the CSU proposed 0.1 PW Ti:Sapphire laser pumped by a cryogenically-cooled Yb:YAG amplifier akin to the power amplifiers detailed in this work. (from [98])

8 J of λ = 515 nm light is expected after frequency doubling in LBO, and this green light would be used to efficiently pump a cryogenically cooled Ti:Sapphire laser, ultimately producing 3 J pulse energies and 30 fs after compression.

1.2 Chirped Pulse Amplification Lasers

Chirped pulse amplification (CPA) is the primary method for generating femtosecond and picosecond laser pulses with high energy. CPA involves temporally stretching a pulse prior to amplification and subsequently recompressing it back to its original pulse duration after reaching high energy. This reduces the pulse intensity during the amplification process, mitigating the damaging effects pulses with high intensity can cause to optical elements, and results in a high intensity short pulse useful for applications. The CPA technique was first conceived in the context of radar in 1960 [101] but was first applied in the optical regime by Strickland and Mourou in 1985. [1] For their achievement and the profound impact CPA has had on laser development and basic research, Strickland and Mourou were awarded the 2018 Nobel Prize in Physics.

To understand the importance of CPA, it is instructive to consider the effects and limitations associated with the direct amplification of ultrashort laser pulses. When a laser pulse has

enough intensity, it begins interacting with the medium through which it is traveling. This is evidenced by the nonlinear refractive index due to the Kerr effect [102] which adds an additional intensity dependent term to refractive index of the material, which can be written as

$$n = n_0 + n_2 I \tag{1.8}$$

where n_0 is the weak-field or linear refractive index, n_2 is the second-order or nonlinear refractive index, and I is the field intensity. This additional term can lead to self-focusing effects that can cause the beam to collapse and result in optical damage. The nonlinear effects accumulated throughout the laser amplifier can be estimated by calculating the B-integral (beam breakup integral), expressed as

$$B = \frac{2\pi}{\lambda} \int n_2 I(z) dz \tag{1.9}$$

where n_2 is the nonlinear refractive index of a given material and $I(z)$ is the laser pulse intensity in that material.

The B-integral determines the total nonlinear phase shift of the system and contributions can come from optical components such as windows, laser gain media, Pockels cells, etc. Conventionally, it is best to keep the value of a systems B-integral below 1 to avoid detrimental nonlinear effects. At higher B-integral values, the beam can experience self-focusing or filamentation. The latter effect occurs when small perturbations in the beam's intensity profile experience exponential growth during nonlinear propagation in the amplifier. This creates localized hot spots in the beam that can lead to degradation of the beam and amplify to levels exceeding the damage fluence of components in the laser system. The optical coatings used to transmit or reflect the beam at interfaces of differing refractive indices typically have the lowest damage fluence of all the optics in the system and are most susceptible to damage by these intensity dependent effects.

There exist two means by which the laser pulse intensity can be reduced. One is to expand the beam size. This method requires large area optics for the laser system, and it becomes

increasingly difficult to produce high quality optics with large surface areas. This can make the optics prohibitively expensive. The increased beam size also limits the efficiency of the amplifier because it is necessary to operate near or above the saturation fluence of the gain medium to efficiently extract energy from the system. Thus, increasing beam size is not the optimum method for reducing pulse intensity. The second option is to increase the laser pulse duration during amplification, and this is the essence of CPA.

Figure 1.7 shows an overview of the CPA process. The implementation of the technique begins with generation of a low energy, ultrafast pulse in a laser oscillator. The oscillator pulses are temporally stretched before amplification. After the pulse energy is increased in one or more amplification stages, the pulse is then recompressed to its original duration, resulting in a high energy ultrashort pulse.

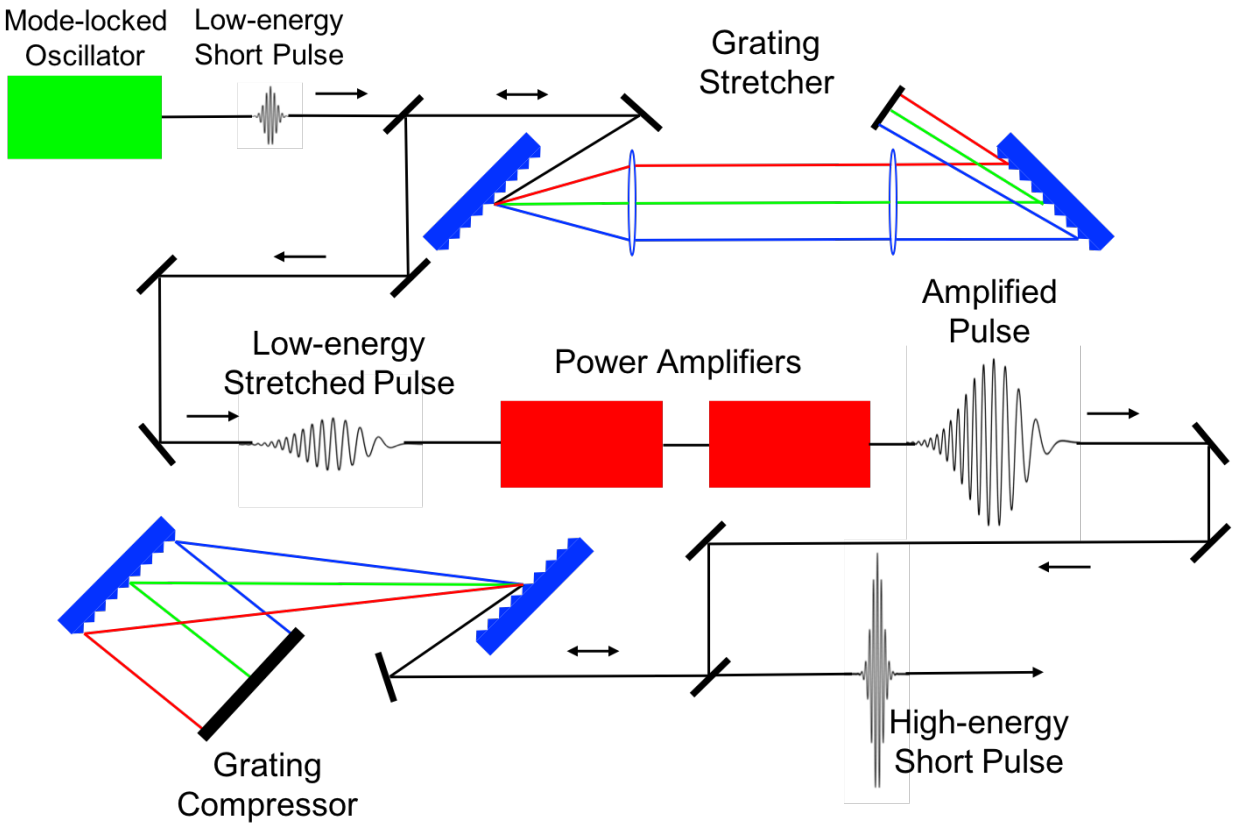

Figure 1.7: An overview of a chirped pulse amplification (CPA) laser system.

Low energy short pulses used to seed the amplifiers in a CPA laser system are usually generated in a mode-locked oscillator. In a typical multimode cavity, many longitudinal modes are allowed to oscillate in the cavity with no fixed phase relation. The process of mode-locking requires these longitudinal modes to oscillate with a fixed phase relation causing constructive interference between these modes and produces a train of pulses in time separated by the cavity round trip time. Using this technique, pulses as short as 5 fs [103] have been produced in solid state lasers. While these laser oscillators typically have a repetition rate of tens of MHz, they have low pulse energy and therefore usually function as a seed for further amplification.

Laser pulse stretching can be achieved in an optical element which provides a wavelength dependent time delay, i.e. a "chirp" to the pulse. This dispersion can be imparted by various methods including diffraction grating pairs, fibers, Bragg gratings, chirped mirrors, etc, with diffraction grating pairs being one of the most common methods for laser pulse stretching and recompression. In 1969, Treacy [104] showed that light incident on a system of two parallel diffraction gratings will always exit with negative dispersion (also known as anomalous dispersion), meaning that shorter wavelengths will travel a shorter distance. This dispersion is opposite in sign from the dispersion accumulated when a laser pulse travels through most transparent optical materials, which are said to have positive (normal) dispersion, and these compressors were first used to compensate for material dispersion of broad band ultrashort pulse lasers. [105] In 1985, Strickland and Mourou used an optical fiber to impart a positive linear chirp to a short pulse prior to amplification, and then using a Treacy style compressor to impart negative dispersion to obtain near transform limit pulses after amplification. However, gratings cannot accurately compensate for the dispersion in optical fibers. In 1987 Martinez reported a method for stretching pulses by using a grating pair with a pair of lenses to form a telescope between the gratings. [106] In such a stretcher, dispersion with opposite sign (positive dispersion) can be achieved (see Figure 1.7). This breakthrough allowed much better matching between stretching and compression of ultra-short pulses. Since this initial demonstration, CPA has become the primary method for generating high intensity pulsed lasers.

Since the 1990s, solid state lasers have come to supersede dye lasers as the gain material of choice for the development of ultrashort pulse lasers. Solid state materials boast a higher saturation fluence as compared to dye lasers, allowing for a significant reduction in size and higher stored energy densities. By far the material that has been most popular for developing high peak power lasers is titanium^{3+} sapphire (Ti:Al_2O_3). [5–8] The material has a broad fluorescence linewidth of 230 nm (FWHM) peaked around 780 nm and a high stimulated emission cross section. [107] This has allowed the development of lasers with pulse durations as short as 5 fs. [103] Ti:Al_2O_3 is also attractive as a gain medium due to the sapphire host material which has excellent thermal conductivity and mechanical rigidity making it an excellent material for high average power operation. The main drawback is its short upper level lifetime of 3.2 μs. This means that most high peak power Ti:Al_2O_3 systems are pumped by frequency doubled Q-switched neodymium^{3+} (Nd^{3+}) doped lasers.

Nd doped glass in particular is used for pumping systems with high pulse energies. [108–110] By using glass as the host material, there is greater flexibility in the sizes and shapes available, from fibers to large slabs. Nd:glass lasers typically operate at a wavelength of λ = 1.05-1.06 μm depending on the glass host used and have a fluorescence linewidth between 15-30 nm (FWHM), allowing for short pulse operation. [107,109] These lasers also have an upper level lifetime of several hundred microseconds and broad absorption bands as compared to Nd doped crystals such as Nd:YAG. [111] However, YAG has a significantly higher thermal conductivity, which is an important advantage in the implementation of high power lasers, where heat dissipation is a major roadblock to overcome. These spectroscopic features make Nd-doped materials well suited for flash lamp pumping, which have a broad spectral emission and can be pulsed at several hundred microseconds. Flash lamp pumping is very successful for high pulse energy operation but is limited in its ability for high repetition rate operation.

Figure 1.8a shows the emission of a Xenon flash lamp operating at two different current densities, while Figure 1.8b shows the absorption spectrum of two Nd-doped phosphate glasses. It can be seen that the broad emission of the flash lamps will only be absorbed by narrow tran-

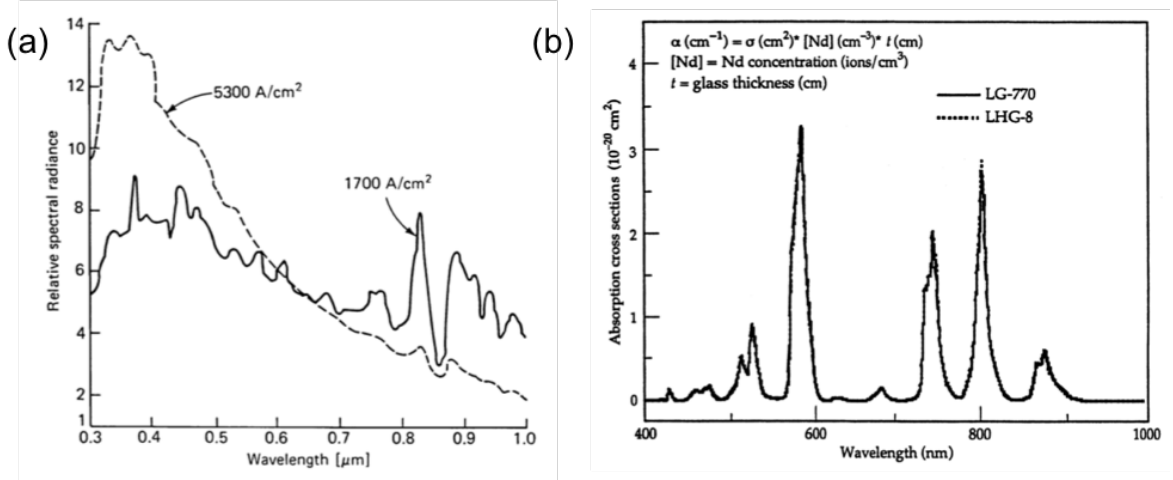

Figure 1.8: a) Typical emission spectrum of a Xenon flashlamp operating at two different current densities. b) shows the absorption spectrum of two Nd-doped phosphate glasses. (from [107])

sition bands in Nd-doped gain media with the excess light contributing to heating of the laser material. Furthermore, the low thermal conductivity of glasses, typically 0.7-1.4 W/mK [107], reduces the ability to control the temperature within the material at high repetition rate operation. The buildup of heat leads to thermally induced optical effects, which will be discussed in detail in Section 1.2.3, such as thermal lensing which occurs when thermal gradients within the laser medium develop across the beam profile. This temperature variation is associated with a change in the refractive index of the material and can lead to focusing effects and potentially optically induced damage. Thermally induced birefringence can also occur from this buildup of heat. This creates a nonuniform polarization change across the laser beam profile and can lead to losses and beam degradation when the laser passes through a polarizing element. While Nd:YAG has the necessary thermo-mechanical properties to allow high power operation, it cannot be grown to the sizes available in glass media. Typically, apertures of Nd:YAG are limited to under 2 cm, and therefore, to scale high pulse energy lasers to high repetition rates, new materials and pumping schemes must be investigated.

1.2.1 Laser Diode Pumping

Over the past few decades, diode laser technology has advanced to the point that there are now commercially available, high power laser diodes suitable for pumping many laser gain media, with Nd^{3+} and ytterbium^{3+} (Yb^{3+}) being two common rare earth ion dopants. These ions are preferred because they can easily be pumped at λ = 808 nm by InGaAsP or GaAlAs diodes for Nd^{3+} and λ = 940-980 nm by InGaAs diodes for Yb^{3+}. As will be discussed in the next section, Yb^{3+} has become the preferred dopant for high power diode pumped solid state lasers due to its simple electronic structure, small quantum defect (the difference between pump photon energy and laser photon energy), and long upper level lifetime. High power diode development is important because diodes possess many characteristics which are advantageous for efficient laser operation.

One of the principal advantages of laser diode pumping as opposed to flash lamp pumping is the monochromatic output of diode sources. Many commercially available diodes have a spectral linewidth of ~5 nm, although volume Bragg grating (VBG) stabilized diodes are available with linewidth of ~1 nm. This narrow linewidth along with center wavelengths which are well matched to the absorption peaks of the gain medium allow for nearly all of the pump light to contribute to populating the upper laser level. This results in highly efficient conversion of pump energy to stored energy with little additional heating from unabsorbed pump light, which is crucial for high power laser operation.

Along with their spectral properties, laser diodes are much more efficient than conventional flash lamps with electrical to optical efficiencies greater than 70 % having been reported. [112] Laser diodes are also much more compact than flash lamp systems. Figure 1.9a shows a 6 kW average power laser diode stack which is composed of 60 bars each producing 100 W of λ = 940 nm light. The entire assembly is only 5” x 3” x 0.75” and allows for compact end pumping of a Yb:YAG amplifier. The vertical stack is microchannel cooled for efficient heat removal. Due to the cross section of the bars, emitted light is highly divergent, as shown in Figure 1.9b. Typically, a cylindrical micro lens is used to collimate the vertical (fast) axis of each emitter. This

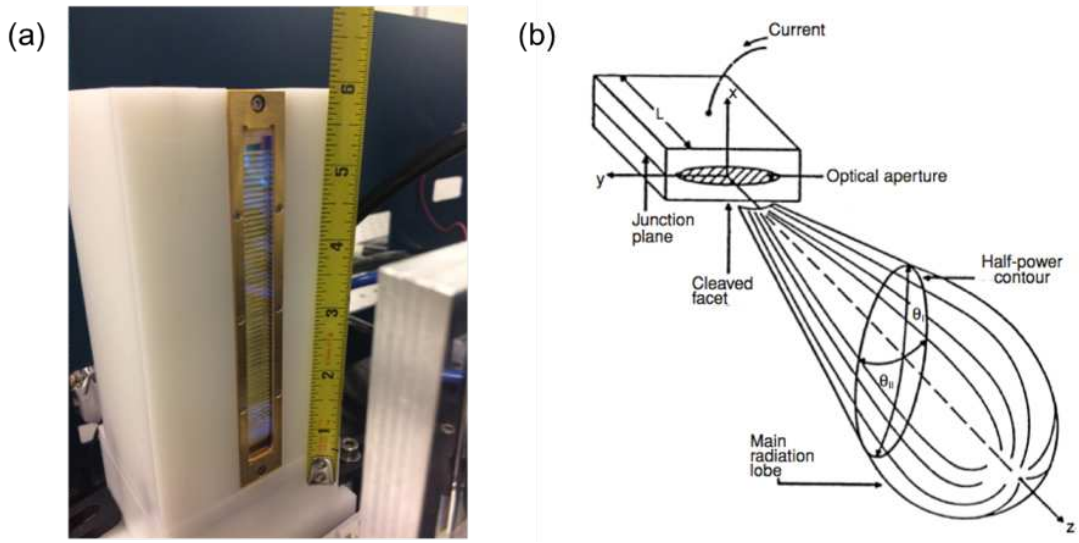

Figure 1.9: a) 6 kW peak power, 940 nm laser diode used for high power pumping of the cryogenic Yb:YAG amplifier detailed in Section 2.5 b) the radiation pattern from a laser diode bar. (from [107])

produces a beam divergence of ~1 degree in the vertical direction and a horizontal (slow axis) divergence angle of ~10 degrees. In addition to laser diode stacks, high power fiber coupled laser diodes are also commercially available and allow for compact, directional laser pumping. The directionality of diodes allows for novel pumping schemes, such as end-pumping in which the pump and seed laser propagate along the same axis. This provides better mode matching of the pump and seed lasers throughout the gain medium and helps minimize thermal effects that can degrade beam quality.

1.2.2 Yb-doped Gain Media

The drawback of laser didoes as compared to flash lamp systems is their relatively low peak power. This requires using a gain medium with a long upper level lifetime. As was mentioned before, the two rare earth ion dopants neodymium and ytterbium are well suited for diode pumping due to the inherent wavelength matching between available diodes and the materials' absorption bands. Yb^{3+} materials such as Yb:YAG have upper level lifetimes of 950 μs, which is over four times longer than similar Nd^{3+} materials like Nd:YAG, which has a lifetime of 230 μs. This allows for better pump energy storage. Furthermore, Yb:YAG has an absorption

bandwidth of 18 nm FWHM [113] when pumped at λ = 940 nm, which is nearly an order of magnitude greater than the 2 nm absorption bandwidth of Nd:YAG at λ = 808. This eases diode linewidth and center wavelength stability requirements.

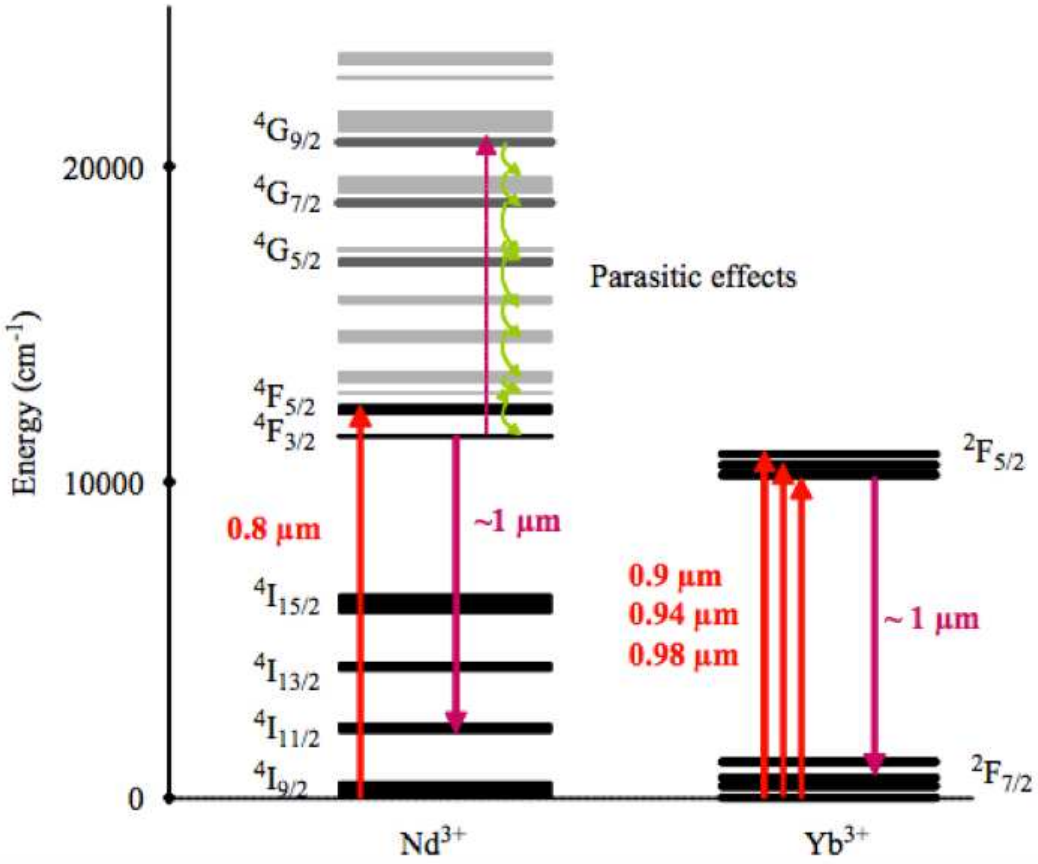

Figure 1.10: The relevant energy levels of Nd^{3+} and Yb^{3+} gain media with typical pump and lasing transitions, as well as parasitic effects. (from [113])

Figure 1.10 shows the energy levels typical of Nd^{3+} and Yb^{3+}. Lasing occurs around 1 µm between the $^4F_{3/2}$ and $^4I_{11/2}$ manifolds in Nd^{3+} and between the $^2F_{5/2}$, and $^2F_{7/2}$ manifolds in Yb^{3+}. The first observation is the quantum defect, which is the difference between pump and emission photon energies, for both materials. When expressed as the fraction of the lasing wavelength to the pump wavelength, Nd:YAG has a quantum defect of 24 % when pumped at λ = 808 nm, while Yb:YAG has a value of 9 % when pumped at λ = 940 nm. This wavelength

difference is the primary direct source of heating in the material. Therefore, minimizing this difference is vital for high power laser operation. The simplified electronic energy levels of Yb^{3+} also help to avoid parasitic effects such as up conversion, excited state absorption, and cross-relaxation, which all occur in Nd-doped media. These upper level de-excitations are also non-radiative and contribute to further thermal loading of the system. Thus, the Yb^{3+} ion is a prime candidate for high power ultrafast laser development.

There exist numerous Yb-doped gain media with different host materials that exhibit many of the spectroscopic properties discussed above. These materials demonstrate long upper level lifetimes and small quantum defects, but differences in material properties make some more suitable for high power operation. Examples of host materials include KYW, KGW, YLF, CaF_2, and YAG, and some of their spectroscopic and mechanical properties are listed in Table 1.1.

Table 1.1: Spectroscopic and mechanical properties of various Yb-doped materials. From [19, 38, 40, 107, 113–115]

Host	λ_e (nm)	λ_{abs} (nm)	$\Delta\lambda$ (nm)	σ_e (10^{-20}cm^2)	τ_L (ms)	κ (W/m*K) (undoped)
YAG	1030	941	11	2.1	0.95	8.6
KYW	1025	981	16	3	0.6	3.3
KGW	1023	981	20	2.8	0.6	3.3
YLF	1017	959	>30	0.75	2.08	5.2
CaF_2	1049	980	70	0.17	2.4	9.7

Many of these materials have been explored as options for high power laser operation. [39, 116, 117] Hosts such as YLF and CaF_2 are intriguing due to their broad emission bandwidth and good thermal conductivities, κ, as alternatives to Ti:Al_2O_3 for high energy femtosecond pulses, yet the low stimulated emission cross section of these materials means they have a high saturation fluence and low gain. From [118], the saturation fluence for the atomic medium can be expressed as

$$F_s = \frac{\hbar\omega}{2^*\sigma} \tag{1.10}$$

where $\hbar\omega$ is the photon energy, σ is the stimulated emission cross section, and 2^* is the "saturation factor". This factor is defined as $2^* \equiv 1$ if the lower laser level rapidly depletes, i.e. a four level laser system, or as $2^* \equiv 2$ if the lower laser level accumulates a population during laser action, i.e. a three level laser system. The saturation fluence of a material such as Yb:CaF_2 can exceed 100 J/cm^2 which is well above the damage threshold of the host material and makes it unsuitable for implementation in high power amplifiers where it is necessary to operate above the saturation fluence for efficient energy extraction. Therefore, their use has been limited to short pulse high power oscillators [119,120] or low energy amplifiers [13,23]. Similarly, KYW and KGW with their low thermal conductivities have only seen use in mode-locked oscillators [121, 122] or low energy amplifiers [116, 117]. Of the available host materials, Yb:YAG has been the most attractive material for high energy, high repetition rate picosecond laser operation.

1.2.3 Yb:YAG

Yttrium aluminum garnet ($Y_3Al_5O_{12}$), or simply YAG, has been a popular host material for decades due to its attractive spectroscopic, mechanical, and thermal properties. YAG has a cubic crystalline structure making it optically isotropic and boasts excellent structural stability across all temperatures up to its melting point. It is also harder than most laser materials and is well suited to accept substitution of trivalent rare earth ions. Furthermore, since YAG has been studied as a laser host since the 1960s [123] and found wide use with Nd^{3+} and Yb^{3+} dopants, the fabrication of high quality single crystal and ceramic YAG is mature, making large aperture YAG-based gain media commercially available. In recent decades, Yb:YAG has found wide use in high power picosecond CPA lasers using a number of different designs including water-cooled thin-disks [24, 26], slabs [29], and at cryogenic temperatures [19, 28, 33]. Of these applications at high average powers, cryogenic Yb:YAG is particularly well suited for high pulse energy operation.

A disadvantage of Yb:YAG's simple two manifold electronic structure and low quantum defect is that the lower laser level is thermally populated at room temperature. From Maxwell-

Boltzmann statistics, the fraction of ions in the lower level is 5.3 % at 300 K due to thermal excitation from the ground state, making room temperature Yb:YAG a quasi-three level laser. This means there is a minimum amount of pump energy required for the system to reach transparency and reduces the efficiency of the laser. When cooled to cryogenic temperatures, i.e. ~77 K, this fraction reduces to 10^{-5} and is nearly completely depopulated, making it a four level laser system.

In addition to the improved efficiency of cryogenic operation, a number of mechanical and thermo-optic properties of Yb:YAG dramatically improve. From Table 1.1, we see that at room temperature Yb:YAG has a thermal conductivity of 8.6 W/m*K, which is better than many of the other host materials listed. However, it is still significantly worse than other host crystals like sapphire which has a thermal conductivity of 33 W/m*K at room temperature. When cooled to cryogenic temperatures, the conductivity of Yb:YAG increases by over a factor of 4. In addition to the properties listed in Table 1.1, the thermal expansion coefficient, α, as wells as the thermo-optic coefficient, $\partial n/\partial t$, improve at cryogenic temperatures. The former has a value of 7.8 x 10^{-6} K^{-1} at 300 K and decreases to a value of 0.9 x 10^{-6} K^{-1} at 77 K, while the latter has a value of 6.14 x 10^{-6} K^{-1} and decreases to a value of 1.95 x 10^{-6} K^{-1} at 77 K.

To illustrate the significance the improvement in thermal conductivity has on system performance, Figure 1.11 shows the results from a thermal simulation of two 50 x 50 x 5 mm YAG crystals being heated by a circular 50 W heat source which measures 16 mm in diameter. For these simulations the back (left) surface temperatures were fixed at 77 K, in a), and 300 K, in b), and all heat flow was conducted through this surface. This boundary condition is analogous to the heat transfer present in the active mirror geometry used in the amplifiers described in Chapter 2. This amplifier geometry is described in detail in Section 1.2.4. Figure 1.11a and Figure 1.11b show the temperature profile through the center of the crystal, with both colormaps plotted on the same scale. It's readily apparent that the crystal cooled to 77 K experiences much less heating throughout the bulk with the cryogenically cooled crystal experiencing a maximum temperature difference of 8 K while the room temperature crystal has a maximum temperature

difference of 62 K. This results in less significant temperature gradients which is further illustrated in Figure 1.11c. This figure shows the maximum temperature across the center of the crystal. As we will see below, this reduction in temperature gradients at cryogenic temperatures has a dramatic impact on the mitigation of thermo-optic effects that can lead to beam degradation as well as laser induced damage.

To understand the importance of these improved material properties under cryogenic operation, it is instructive to consider the case of a cylindrical laser rod with a uniform heat load and radial cooling. For this situation, the temperature distribution in the rod can be expressed as

$$T(r) - T(r_0) = \left(\frac{q}{4\kappa}\right)(r_0^2 - r^2) \tag{1.11}$$

where q is the heat density source and r_0 is the radius of the rod. From this equation, we see that the temperature at any point in the rod is inversely proportional to the thermal conductivity. An increase in thermal conductivity will lower the overall temperature of the rod and by extension decrease the radial thermal gradients within the rod. If we assume that κ is constant with temperature, we can express the refractive index at some radial distance within the rod as having a contribution due to thermal gradients, Δn_t, and mechanical stress, Δn_s

$$n(r) = n_0 + \Delta n_t(r) + \Delta n_s(r) \tag{1.12}$$

The temperature dependent refractive index change can be expressed as

$$\Delta n_t(r) = q_0 - \frac{qr^2}{4\kappa}\left(\frac{\partial n}{\partial t}\right) \tag{1.13}$$

where q_0 is a constant that is dependent on the rod geometry and heat density, while $\partial n/\partial t$ is the thermo-optic coefficient. The contribution to the refractive index change due to stress can be expressed as

$$\Delta n_s(r) = \Delta n_{r,\theta}(r) = \frac{-\alpha n_0^3 q}{2\kappa} C_{r,\theta} r^2 \tag{1.14}$$

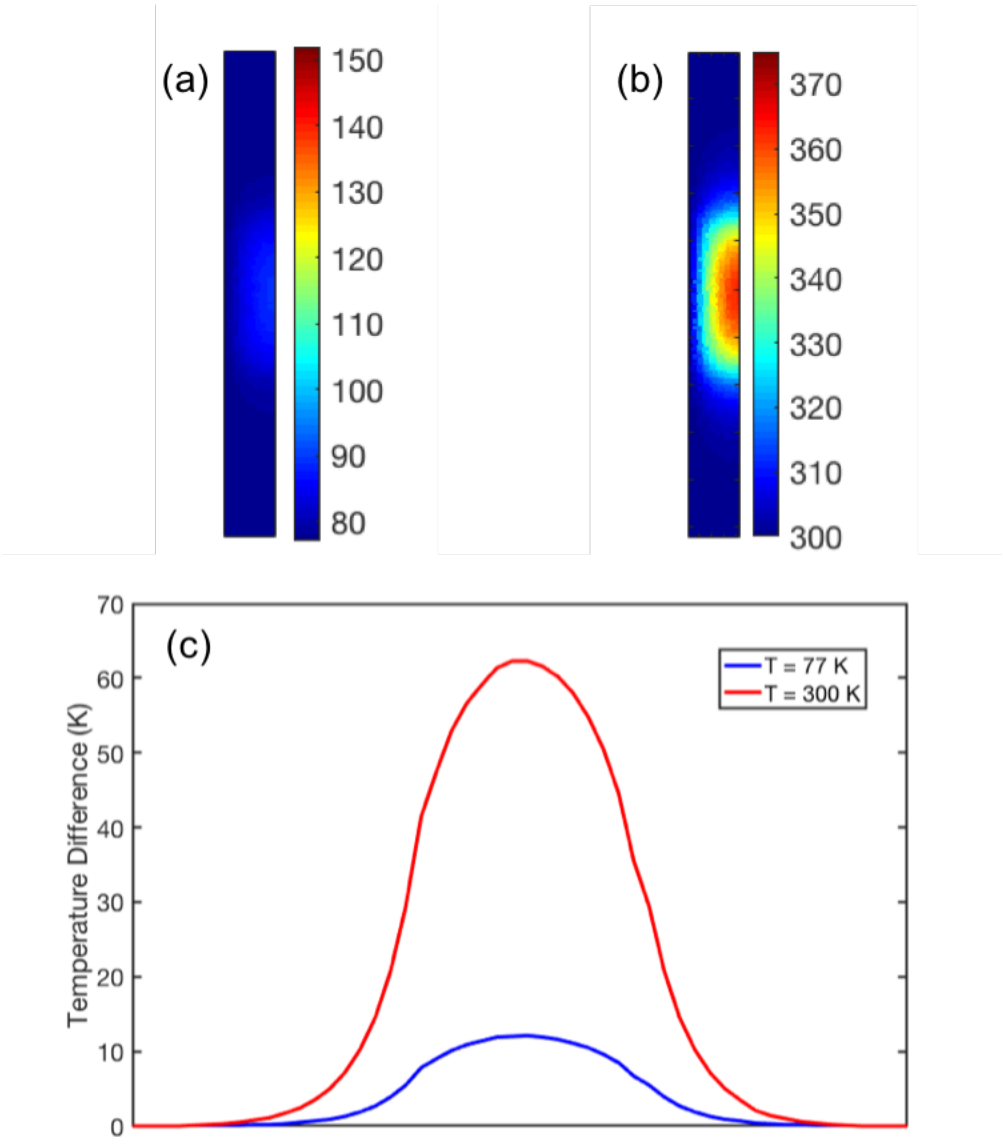

Figure 1.11: shows a simulation of the temperature distribution in a 2”x 2”x 0.2” Yb:YAG disk with a thermal load of 50 W deposited in a 16 mm circular region in the center of the disk with a) the back surface fixed to a temperature of 77 K and b) fixed to 300 K. a) and b) are plotted on the same scale. c) is a 1D cut showing the maximum temperature across the crystal.

where α is the thermal expansion coefficient and $C_{r,\theta}$ is a constant given by the elasto-optic coefficient of the material. This index change due to stress can have two consequences. First, the refractive index changes in equations (1.13) and (1.14) display a parabolic dependence on radius, and a beam traveling along the axis of the rod will experience a lensing effect. An additional source of loss can come from depolarization of the beam due to the nonuniform index change in r and θ.

For an optically isotropic medium such as YAG in this geometry, the refractive index change due to stress can induce birefringence of the crystal which has a radial and tangential component. This index change can be seen in Figure 1.12a where the undistorted index, n_0, is uniform in all directions, that's to say its index ellipsoid in this two dimensional projection forms a circle. When stress is applied to the crystal, differing index changes can occur in r and θ and distort the index ellipsoid (in two dimensions) into an ellipse. For a beam linearly polarized in either the x or y direction, rays on the x and y axes will not experience a change in their polarization state, while all other rays will become elliptically polarized, as seen in Figure 1.12b. This can be a great source of loss if the beam travels through a polarizing element and significantly modify the beam's spatial profile. This is commonly referred to as depolarization loss. From equation (1.14), it can be seen that both components are linearly dependent on the expansion coefficient, α, and inversely dependent of the thermal conductivity κ. The decrease in thermal expansion coupled with the increase in thermal conductivity by cryogenic cooling of Yb:YAG combine to reduce the refractive index change due to mechanical stress by a factor of 12 when compared to room temperature operation. Therefore, by cryogenically cooling the Yb:YAG gain medium these thermal lensing effects can be significantly reduced.

In addition to the improved mechanical and thermo-optic properties, Yb:YAG also experiences dramatic improvements in its spectroscopic properties when cooled to cryogenic temperatures. Figure 1.13a shows the stimulated emission cross section of Yb:YAG and Figure 1.13b shows the emission bandwidth of the laser transition at temperatures ranging from room temperature to 70 K. [124]

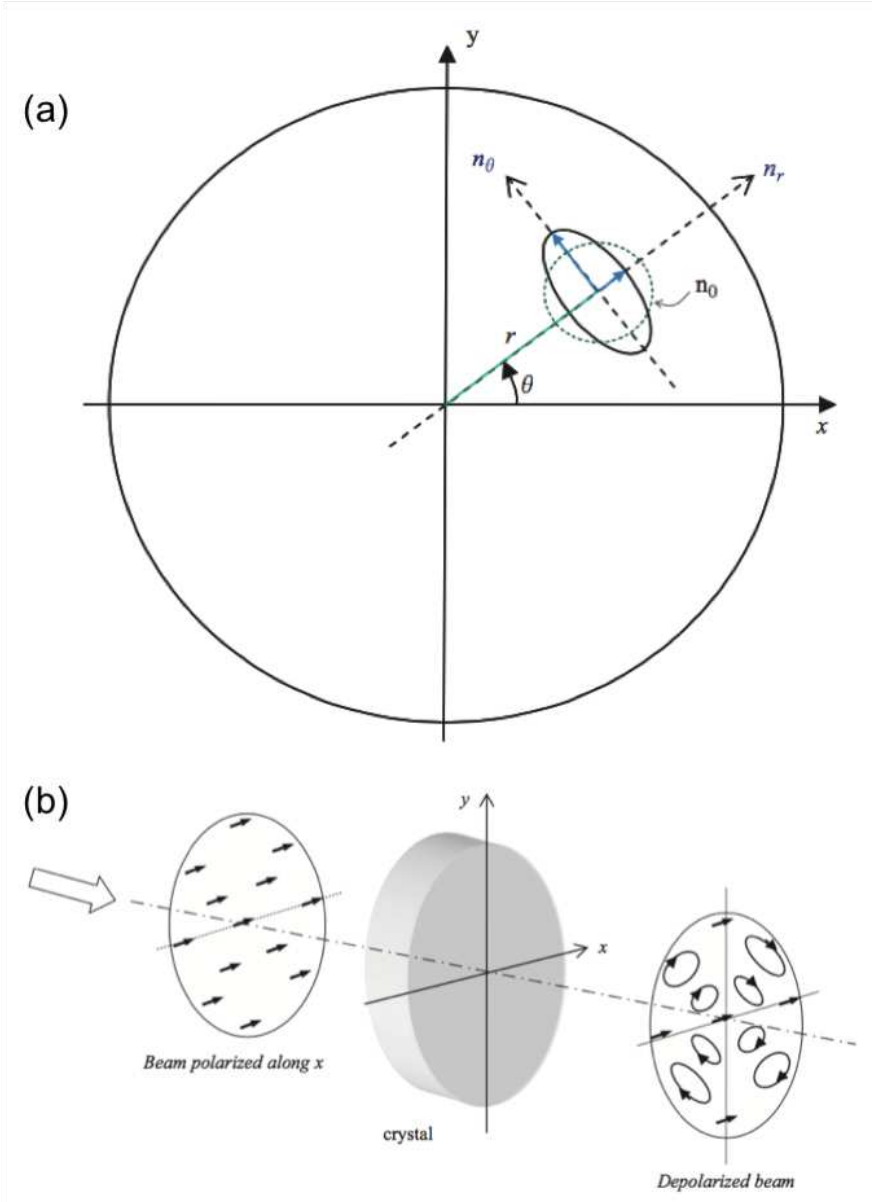

Figure 1.12: a) shows the nonuniform modification to the refractive index due to stress. b) shows the change in polarization a linearly polarized beam experience when traversing a crystal with stress induced birefringence (from [113])

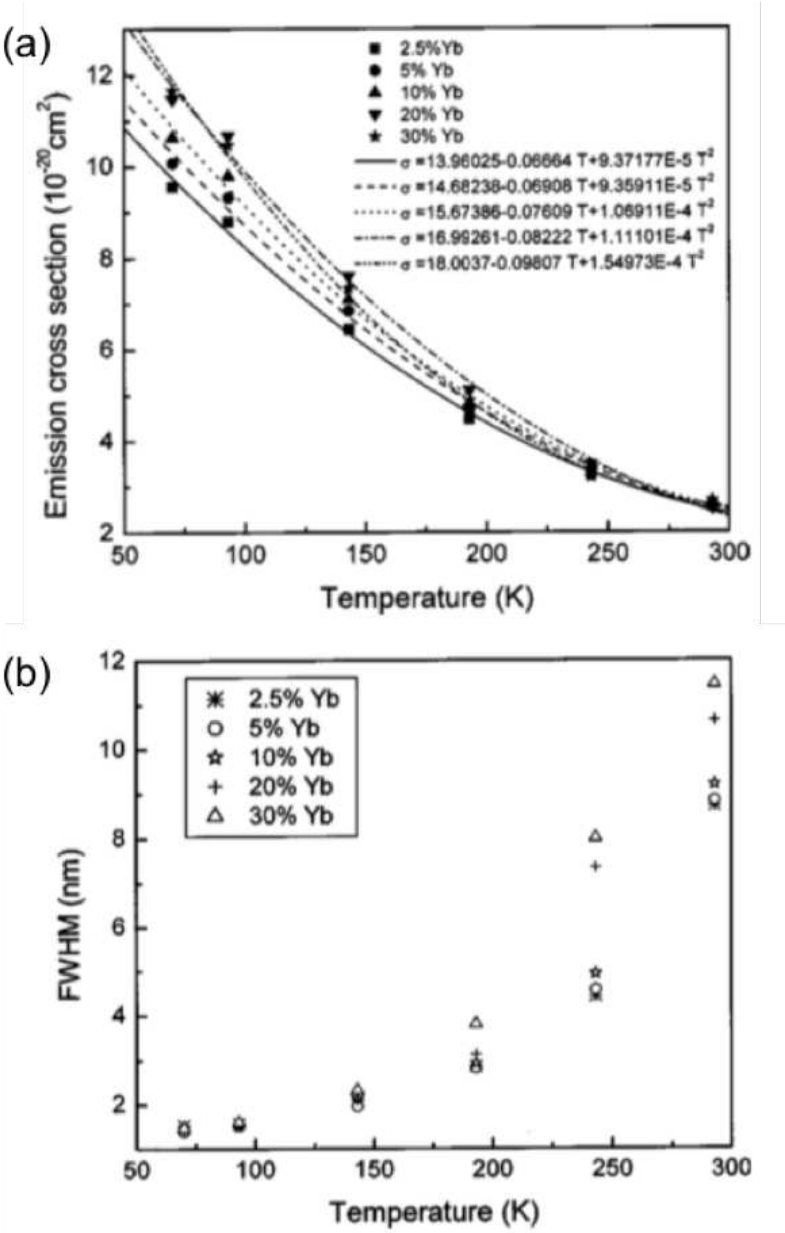

Figure 1.13: a) Stimulated emission cross section of Yb:YAG b) shows the emission bandwidth for temperatures ranging from 70 K to room temperature. (from [124])

From Figure 1.13a it can be seen that the stimulated emission cross section increases by about a factor of 5, and from equation (1.10), we see that the saturation fluence, F_s, decreases from a value of 9.2 J/cm^2 at room temperature to a value of 1.95 J/cm^2 for 5 % Yb:YAG at 77 K. To better understand the importance of these improvements, we can consider the one-dimensional case of amplification of a temporally square pulse. From [125] we have the following expression for the single-pass gain

$$G = \frac{F_s}{F_0} ln\left(1 + \left[exp\left(\frac{F_0}{F_s}\right) - 1\right] exp(\gamma l)\right) \tag{1.15}$$

where F_0 is the input pulse fluence, γ is the small signal gain coefficient, and l is the length of the amplifying medium. For the case when $F_0 \gg F_s$ and using the definition for the small signal gain coefficient, $\gamma = \Delta N \sigma_e$, where ΔN is the inverted population, this reduces to

$$G \cong 1 + \left(\frac{F_s}{F_0}\right)\gamma l \tag{1.16}$$

From equation (1.16), we see that in the regime above saturation the gain varies linearly with the length of the medium, meaning that every excited state is contributing to the amplification of the pulse and constitutes the most efficient removal of energy from the system. This increase in single pass gain allows for amplifiers with fewer passes and thereby decreases losses and reduces the design complexity of the system. It also minimizes thermo-optic effects on the beam which can compound from successive trips through the optical distortions of the amplifying medium. The reduction in saturation fluence also makes it possible for efficient energy extraction without the risk of optical coating damage.

Along with the increase in emission cross section at cryogenic temperatures, there is a corresponding narrowing in the emission bandwidth as illustrated in Figure 1.13b. The bandwidth of the peak lasing wavelength narrows from a FWHM of ~10 nm at room temperature to ~1.5 nm at liquid nitrogen temperature. Although, it is important to remember that this is not equivalent to the bandwidth of the fully amplified pulse which will suffer from gain narrowing as a

part of the amplification process. In Chapter 2 it is shown that the combination of a room temperature preamplifier and cryogenic power amplifiers allows for the generation of joule level pulses with enough bandwidth to support <5 ps pulses, thereby mitigating the worst gain narrowing effects of cryogenic operation. Another important temperature dependent property of Yb:YAG which must be taken into account when using a dual temperature amplification scheme is that the peak emission wavelength of the medium shifts to the blue as it is cooled. Dong et al. determined the wavelength shift from room temperature to cryogenic temperature to be approximately ~0.6 nm [124], while Körner et al. determined this value to be closer to 1 nm. [126] Therefore, it is necessary to match the peak wavelength of the room temperature preamplifier to the center wavelength of the cryogenic power amplifiers.

The absorption cross section is a final factor to consider when evaluating the viability of amplification in cryogenic Yb:YAG. Brown et al. [127] and Körner et al. [126] measured the absorption cross section as a function of temperature. Figure 1.14 shows the results of Brown et al.'s measurement of 9.8 at.% Yb:YAG at 300 K (Figure 1.14a) and 75 K (Figure 1.14b). [127] Both Brown and Körner found the cross section at the peak of the 940 nm absorption band to increase by a factor of 2 when cooled to liquid nitrogen temperatures and that the absorption peaks similarly suffer narrowing at these colder temperatures. Although, the narrowing of this absorption feature only changes from a FWHM of 18.3 nm at 300 K to 12.6 nm at 75 K and the peak of this band remains nearly unchanged. Thus, pumping this feature with commercially available λ = 940 nm diodes, which typically have a bandwidth of 3-5 nm, is suitable at 77 K. Another apparent feature present in these spectra is the dramatic increase of the absorption at the zero-phonon line around λ = 969 nm which increases by roughly an order of magnitude when cooled. This line has a bandwidth of 2.8 nm at 300 K, making it usable at room temperature, but only with more expensive volume Bragg grating (VBG) stabilized diodes. This has the advantage of further decreasing the quantum defect and thermal load by 30 %, yet even with stabilized diodes, this feature becomes impractical for use at 77 K because the bandwidth reduces to < 0.2 nm.

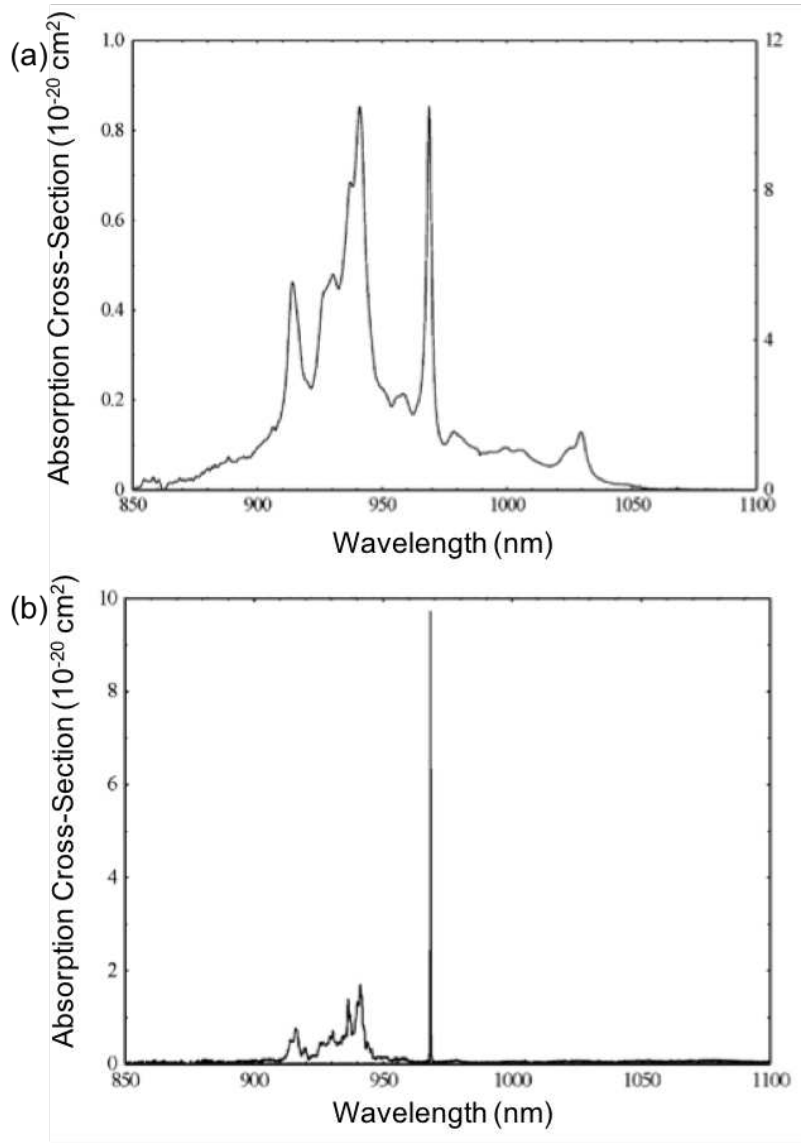

Figure 1.14: The absorption cross section of 9.8 at.% Yb:YAG at a) 300 K and b) 75 K. (from [127])

1.2.4 Current state of the art Yb-doped CPA Lasers

With the advances in diode laser technology outlined above, many laser architectures utilizing Yb-doped materials have emerged in recent years to generate high power short pulse lasers. These systems use high power amplifiers based on either water-cooled thin disk Yb:YAG, slab Yb:YAG, Yb-doped fiber, or cryogenically cooled Yb:YAG. For this discussion, we are concerned with the development of CPA laser systems with high pulse energy, on the millijoule to joule level, high repetition rates, on the order of 1 kHz, and short pulse duration, <10 ps.

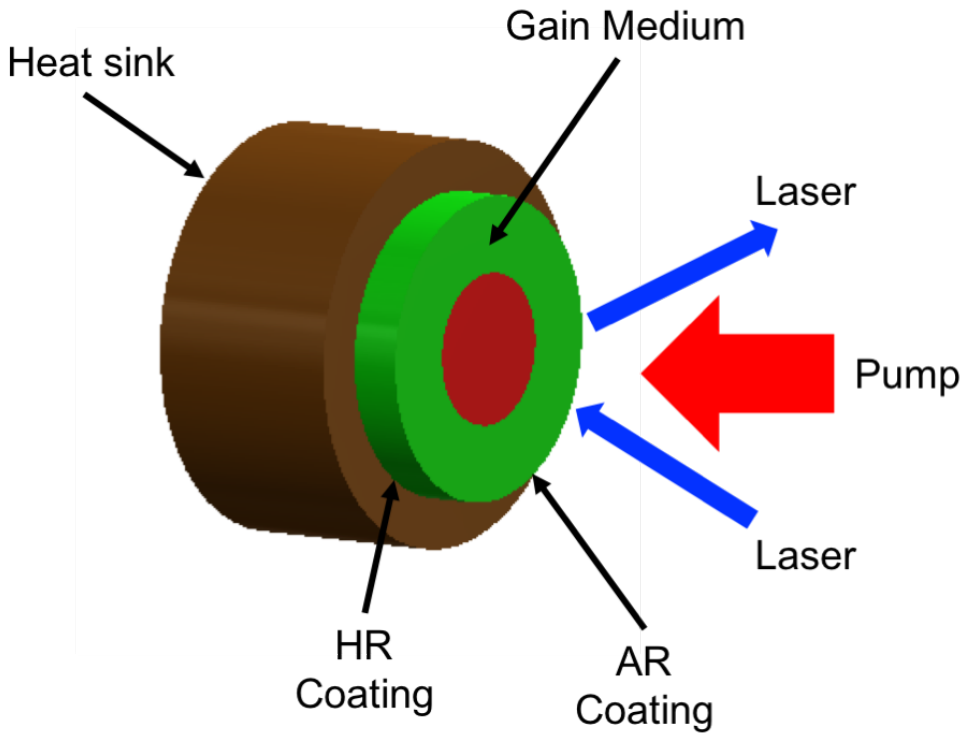

Figure 1.15: Schematic showing the active mirror geometry.

The thin-disk Yb:YAG amplifier is a mature technology that has been a successful means of generating high power short pulse lasers. [35, 128] The concept, shown in Figure 1.15, uses a 100-200 μm thick, several millimeters diameter disk which has a high reflective (HR) coating for both pump and seed laser wavelengths on one side and an antireflective (AR) coating for both wavelengths on the other. This amplifier configuration is often described as an "active

mirror". The HR side is thermally coupled to a water-cooled heatsink, often made of copper or copper-tungsten. The large area of the cooling surface and small thickness facilitate excellent heat removal from the gain medium with the largest thermal gradients being longitudinal to the direction of beam propagation. This minimizes thermal lensing and depolarization effects. This design architecture has been effective at generating pulses with picosecond durations and modest pulse energies, including demonstrations of 40 mJ at 1 kHz repetition rate [24] and 4.7 mJ at 300 kHz [129]. Recently, this concept has been used to scale to high pulse energies with Nubbemeyer et al. reporting 200 mJ, 5 kHz operation with 1.1 ps pulse durations. [26] In that work, two high power thin disk amplifier heads were used in a large mode regenerative amplifier ring cavity, and this work is being further extended with the goal of reaching joule level pulse energies at kilohertz operation. [130] While the thin-disk amplifier design has been successful for high power operation, it can be expensive and difficult to implement. Due to the low single pass absorption of pump light, a complicated, multi-pass pump design must be used for efficient energy storage. Many of these systems rely on expensive VBG stabilized diodes to minimize the thermal load in the laser crystal.

Another approach for high power operation, which is less related to the one investigated in this dissertation, uses Yb-doped fiber amplifiers. Two common techniques used in this approach are coherent beam combining (CBC) [131] and divided pulse amplification (DPA) [132, 133]. In CBC the seed beam is spatially separated into multiple beamlines and individually amplified. These amplified beams are then recombined to form a single high peak power pulse. Similarly, DPA temporally separates the initial seed pulse into a train of pulses which can then be amplified in a single gain medium and temporally recombined into a single pulse. Through a combination of CBC and DPA, pulse energies of 12 mJ with 262 fs pulse durations have been achieved at average powers of 700 W. [36] This scheme is susceptible to inefficiencies due to the precision and complexity of temporal and spatial beam recombination and is sensitive to gain saturation effects. This can lead to different pulses within the DPA pulse train experiencing different amplification levels, and amplitude and nonlinear phase mismatch among the

pulses can further limit recombination efficiency. Although, recent work has made progress on increasing the number of combined fiber channels with improved efficiency and diffraction limited beam quality [100], providing the potential for high pulse energy, high average power fiber laser systems.

Of the schemes used for high power amplification in Yb doped gain media, amplification in cryogenic Yb:YAG has been, to date, one of the most successful in obtaining high pulse energies at high repetition rates. It has been observed that the sole use of cryogenic Yb:YAG severely narrows the bandwidth of the output pulse making sub-5 ps pulse durations difficult. [31] Also, limitations in material properties of non-YAG host materials, as discussed above, limit achievable energy and power scaling. Many host materials have been investigated including KYW [116, 117], SSO (Sc_2SiO_5) [134], CALGO ($CaAlGdO_4$) [39], and CaF_2 [39], yet these amplifiers achieved relatively low pulse energies, on the order of 1 mJ, and modest, watt-level average powers. Therefore, many of the lasers systems using cryogenic Yb:YAG typically use a hybrid approach, whereby a broad bandwidth gain medium is used in a high gain preamplifier and cryogenic Yb:YAG is used in multipass power amplifier stages. The approach is favored because bandwidth can be preserved in the preamplifier and limited gain narrowing can be tolerated in the subsequent power amplification stages. Using this scheme, pulse energies on the order of 100 mJ and repetition rates of 1 kHz or greater have been achieved. [19, 28]

1.3 Outline of the following chapters

Chapter 2 describes the development of an all diode-pumped CPA laser using a room temperature Yb:YAG preamplifier in conjunction with a cryogenically-cooled Yb:YAG power amplifier to achieve uncompressed pulse energies of 1.4 J at a repetition rate of 500 Hz compressible to 3.8 ps. This laser system was used to demonstrate soft x-ray lasing in Ni-like molybdenum at a repetition rate of 400 Hz. Additionally, an initial result is presented of 1.4 J operation at 1 kHz.

Chapter 3 details the operating principles of OPCPA lasers and describes the development of a 100 Hz OPCPA laser operating in the near infrared (NIR) which is wavelength tunable between

λ = 1.5-2 μm. This system consisted of a ~100 μJ, sub-ps Yb:KYW regenerative amplifier which was used to generate λ = 1.5–2 μm pulses in a beta barium borate (BBO) difference frequency generation (DFG) stage. The generated NIR pulses were subsequently amplified in multiple stages of potassium titanyl phosphate (KTP) optical parametric amplification (OPA) to obtain a maximum pulse energy of 5 mJ. The final three stages of OPA were pumped by λ =1.03 μm, 50 mJ, ~5 ps pulses from a cryogenically cooled Yb:YAG CPA laser system described in [34] and similar in design to the one described in Chapter 2. Both the NIR OPCPA laser and λ = 1 μm CPA laser were seeded by a common Yb:KYW oscillator allowing for passive temporal synchronization of pump and signal pulses. λ = 1.6 μm, ~2.5 ps pulses were used to conduct laser induced damage threshold (LIDT) measurements on a number of high damage threshold optical coatings designed for operation near this wavelength. These constitute the first reported results of short pulse LIDT at this wavelength.

Chapter 2

Development of a kW class, Diode Pumped Picosecond Laser

This chapter describes the design and performance of a compact all diode-pumped λ = 1.03 μm CPA laser based on cryogenically-cooled active mirror Yb:YAG power amplifiers that produces pulses with energy up to 1.5 J at a repetition rate of 0.5 kHz, resulting in an uncompressed average power of 0.75 kW. The output is demonstrated to have good beam quality and good shot-to-shot stability. The laser pulses are compressed in vacuum to durations of about 5 ps FWHM by a pair of dielectric diffraction gratings, yielding pulse energies as high as 1 J.

The design architecture used to produce robust operation at 500 Hz was expanded upon to facilitate joule-level laser operation at 1 kHz repetition rate. Modifications to the system front end and the addition of one amplifier head allowed for uncompressed pulse energies as high as 1.4 J at 1 kHz. This chapter also discusses the application of this laser to realize the demonstration of a soft x-ray laser in the λ = 18.9 nm line of Ni-like Mo operating at 400 Hz repetition rate, the highest repetition rate demonstrated to date for a plasma-based soft x-ray laser.

2.1 500 Hz Laser Overview

A block diagram of the 500 Hz laser system is shown in Figure 2.1. Low energy, sub picosecond pulses are generated in a diode pumped, passively mode locked oscillator. These pulses are then stretched to several hundred picoseconds in a dielectric grating stretcher before being seeded into subsequent amplifiers. The laser design incorporates a room temperature preamplifier, to exploit the relatively broad gain bandwidth, and cryogenic power amplifiers, to exploit the improved mechanical, thermo-optic and spectroscopic properties. Pulses from the grating stretcher are first seeded into a high gain, room temperature Yb:YAG regenerative amplifier that

selects pulses at a repetition rate of 500 Hz and boosts the pulse energy to the millijoule level. Then a pair of cross polarized calcite polarizers with a pockels cell between them temporally cleans the pulses. The beam is then sent to a four-pass cryogenic preamplifier which increases the energy to the 100 mJ level and finally to an eight-pass cryogenic power amplifier. Pulse energies has high as 1.5 J are obtained after amplification and then compressed in a Treacy style dielectric grating compressor in vacuum, yielding >1 J, ~5 ps pulses at 500 Hz.

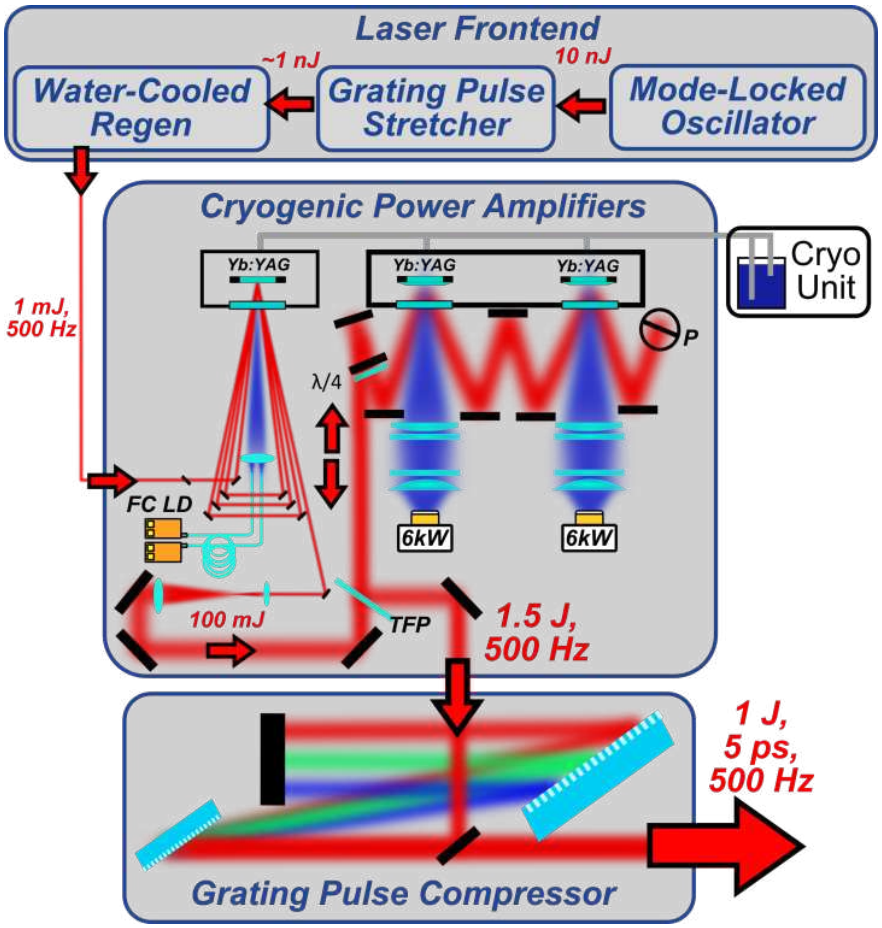

Figure 2.1: Schematic diagram of the diode-pumped high energy CPA laser system that includes fiber-coupled laser diodes (FC LD), a thin film polarizer (TFP), and periscope (P). (from [33])

2.2 Laser Oscillator

The laser front end consists of a mode locked Yb:KYW oscillator, a Martinez style dielectric grating stretcher, and a room temperature regenerative amplifier. The layout of the mode locked oscillator is shown in Figure 2.2.

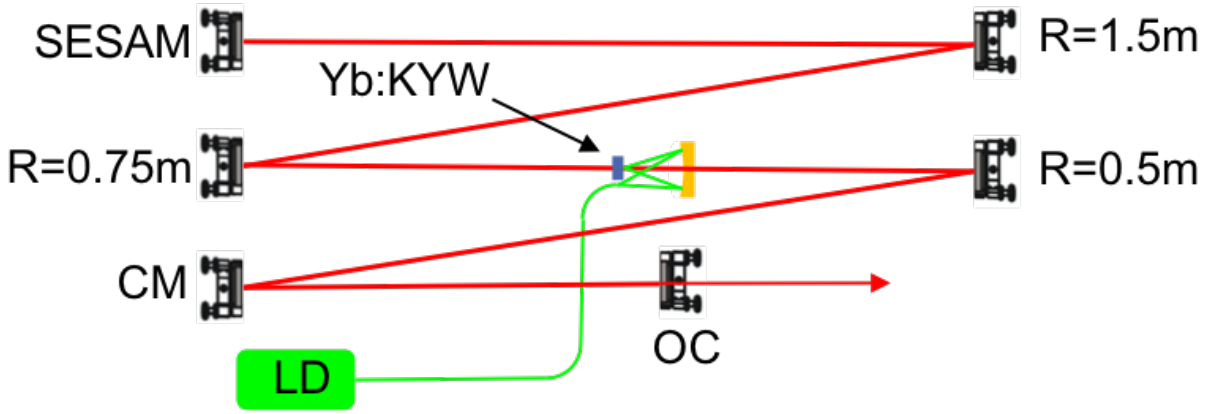

Figure 2.2: A schematic diagram of the diode pumped, modelocked oscillator. SESAM: semiconductor saturable absorbing mirror, CM: chirped mirror, OC: output coupler

The gain medium in the cavity is ytterbium doped potassium yttrium tungstate (Yb:KYW). The 5 %-at Yb:KYW crystal measures 5 x 5 x 3 mm and is in contact with a water-cooled copper heatsink. Yb-doped tungstates are an attractive gain material due to their relatively high stimulated emission cross section, broad gain bandwidth and low quantum defect. Furthermore, Yb:KYW is well suited to pumping by laser diodes at λ = 980 nm. Here, the crystal is pumped by a 30W, 980 nm fiber coupled laser diode with a 200 μm core. The tip is 1-1 imaged on the Yb:KYW crystal by a 2" diameter, f = 101.6 mm gold spherical mirror with a hole in the center, which the cavity beam passes through. The cavity is passively mode locked by a semiconductor saturable absorbing mirror (SESAM) that has a saturable loss of 2 % , and dispersion is compensated by a chirped mirror (CM) designed to have a group delay dispersion (GDD) of -2000 fs^2 over a wavelength range of 1020 – 1040 nm. The output coupler (OC) is a dielectric mirror coated to allow 6 % transmission on one side and an anti-reflection (AR) coating on the other.

The coatings are deposited onto a window substrate with a wedge angle of 1 degree between the surfaces to avoid back reflection from the AR side which could disturb modelocking.

The oscillator outputs 0.88 W when pumped with 30 W CW. Pulses leave the oscillator at a repetition rate of 55.4 MHz, corresponding to 15.7 nJ per pulse. Figure 2.3 shows the measured spectrum of the oscillator pulses. The spectrum is peaked at 1031.6 nm with a bandwidth of 3.8 nm full width at half maximum (FWHM), which supports transform limited, sech^2 pulses below 300 fs. While the wavelength is not centered at 1030 nm, where Yb:YAG demonstrates strong lasing, the bandwidth and intensity are sufficient to allow amplification in subsequent Yb:YAG stages.

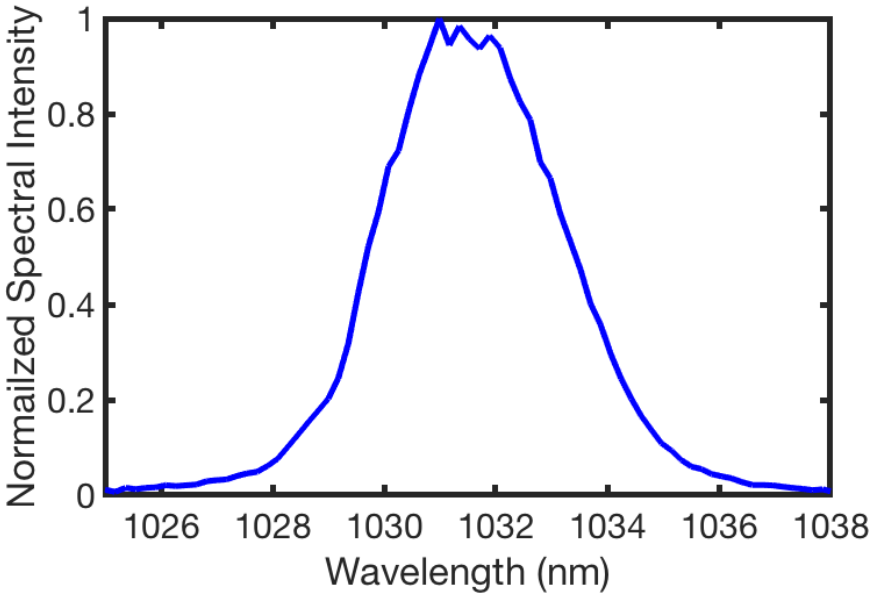

Figure 2.3: The typical spectrum of pulses exiting the mode locked oscillator have a FWHM bandwidth of 3.8 nm, which correspond to sub 300 fs transform limited pulses assuming a sech^2 pulse shape.

2.3 Temporal Pulse Stretcher

2.3.1 Dielectric Grating Stretcher

A dielectric diffraction grating stretcher is used to temporally increase the ~300 femtosecond pulses exiting the oscillator to several hundred picoseconds prior to amplification. In a

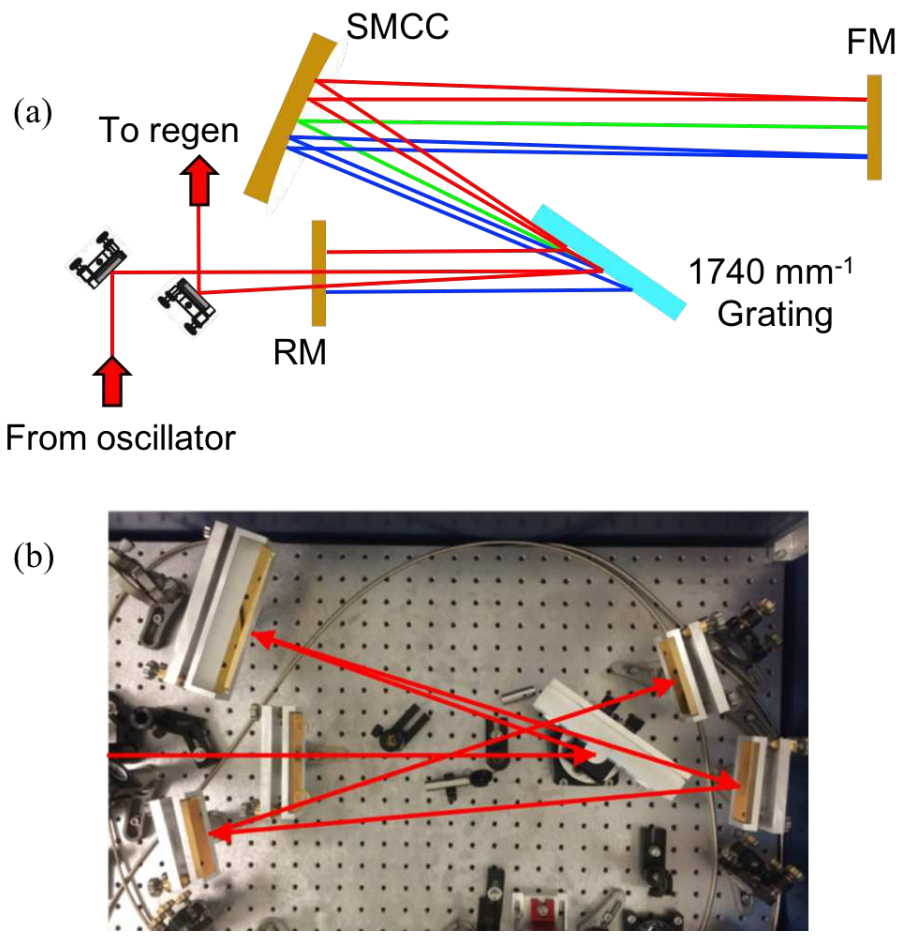

Figure 2.4: a) A schematic diagram showing the dielectric grating stretcher. It is a folded Martinez style pulse stretcher in which the beam is diffracted four times from the 1740 mm^{-1} grating and a f = 60 cm spherical concave mirror (SMCC) is used to provide positive dispersion. The retro-mirror (RM) allows the beam to retrace the same beam path, and the focal plane mirror (FM) is placed at the focal plane of the SMCC to allow a single grating and SMCC to be used. For clarity, this illustration does not show the additional gold mirrors which allow the necessary path length in a small footprint. b) An image of the grating stretcher with the beam path from the grating to the FM in red. The addition of fold mirrors allows the stretcher to occupy a limited table space of only 16" x 27".

stretcher an optical element is used to impart group delay dispersion (GDD) which is a spectral phase term that is quadratic in frequency and temporal broadening occurs as a result of different frequency components traveling different path lengths. In most CPA lasers the stretcher introduces normal dispersion, i.e. longer wavelengths travel a shorter optical path, while the compressor compensates for this after amplification by imparting anomalous dispersion. In [104], Treacy found that two parallel grating always introduce anomalous dispersion, and Martinez [135] demonstrated that by placing a telescope between a grating pair the sign of the dispersion can be reversed and effectively create a negative pathlength between the gratings.

During 500 Hz operation, a Martinez style stretcher, shown schematically in Figure 2.4a, is used. In this design a single 1740 mm^{-1} dielectric grating and f = 60 cm spherical concave mirror (SMCC) are used. This simplifies the alignment by ensuring consistent incidence angles and allows for a much smaller footprint on the optical table. Pulses from the oscillator are incident on a 1740 mm^{-1} dielectric grating at an angle of 55.25 degrees. The SMCC is placed 15" from the grating and a gold mirror is placed at normal incidence at the focal plane of the SMCC. This generates an effective pathlength through the stretcher of 4.57 m. Figure 2.4b shows an image of the stretcher. Additional mirrors are placed between the SMCC and the focal plane mirror (FM) to reduce the footprint on the optical table, and the path of the incident beam from the grating to FM is shown in red. The stretcher is slightly misaligned to simplify the ejection from the stretcher and eliminates the need for optical isolators to prevent feedback into the oscillator. If we consider the dispersion equation from [104], that the stretcher design creates a negative effective path length, and a bandwidth of 0.55 nm, which is the bandwidth of the regenerative amplifier after gain narrowing, then the stretched pulse duration is 450 ps.

2.3.2 Chirped Volume Bragg Grating Stretcher

For operation at 1 kHz, the results are discussed in more detail in Section 2.7, a Chirped Volume Bragg Grating (CVBG) was used to temporally stretch the oscillator pulses prior to seeding into the regenerative amplifier. Similar to the dielectric grating stretcher, the CVBG applies a

linear chirp by forcing the various frequency components of the pulse to travel differing optical path lengths. This is accomplished by having the various spectral components of the beam diffract from different holographic planes within the bulk. These diffraction planes are recorded into the bulk by the interference of two beams in a photosensitive medium. In this case, photo-thermo refractive (PTR) glass is the material used to record the phase volume hologram by photo-inducing precipitation of sodium fluoride nanocrystals, and the refractive index variation produced is proportional to the fraction of precipitated nanocrystals within the glass structure.

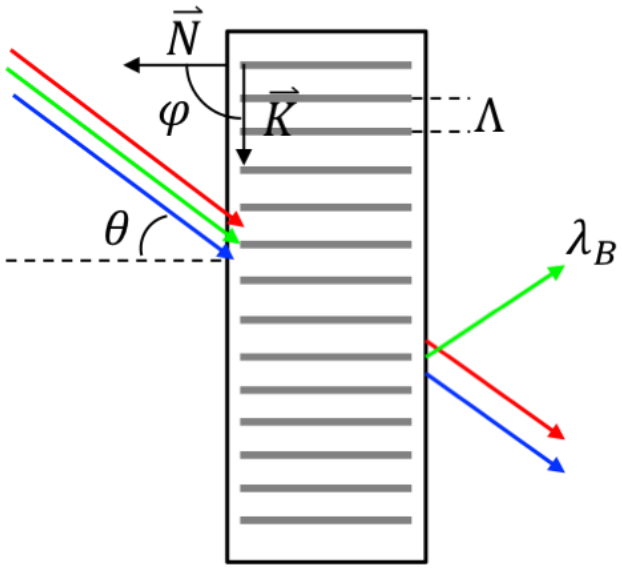

Figure 2.5: An illustration of a holographic transmission grating. θ is the angle of incidence with respect to the surface normal $\vec{N}$, $\vec{K}$ is directed normal to the diffraction planes, ϕ is the angle between $\vec{N}$ and $\vec{K}$, Λ is the grating period, and λ_B is the wavelength satisfying the Bragg condition

To understand the operation of a CVBG it is helpful to first consider the operation of a transmission Bragg grating with uniform periodicity of the diffraction planes. A schematic of this type of grating is shown in Figure 2.5. In order for efficient diffraction to occur, the following Bragg condition should be satisfied [136]

$$\lambda_B = 2n\Lambda cos(\theta + \phi) \tag{2.1}$$

where λ_B is the diffracted wavelength, n is the average refractive index of the material, Λ is the period of the grating, θ is the direction of beam propagation with respect to the surface normal, and ϕ is the angle between $\vec{N}$ and $\vec{K}$. In Figure 2.5, $\phi = \pi/2$ and (2.1) reduces to

$$\lambda_B = 2n\Lambda sin(\theta) \tag{2.2}$$

For a grating operating in reflection, the $\vec{K}$ vector is parallel to $\vec{N}$ so $\phi = 0$ and we obtain the following relation

$$\lambda_B = 2n\Lambda cos(\theta) \tag{2.3}$$

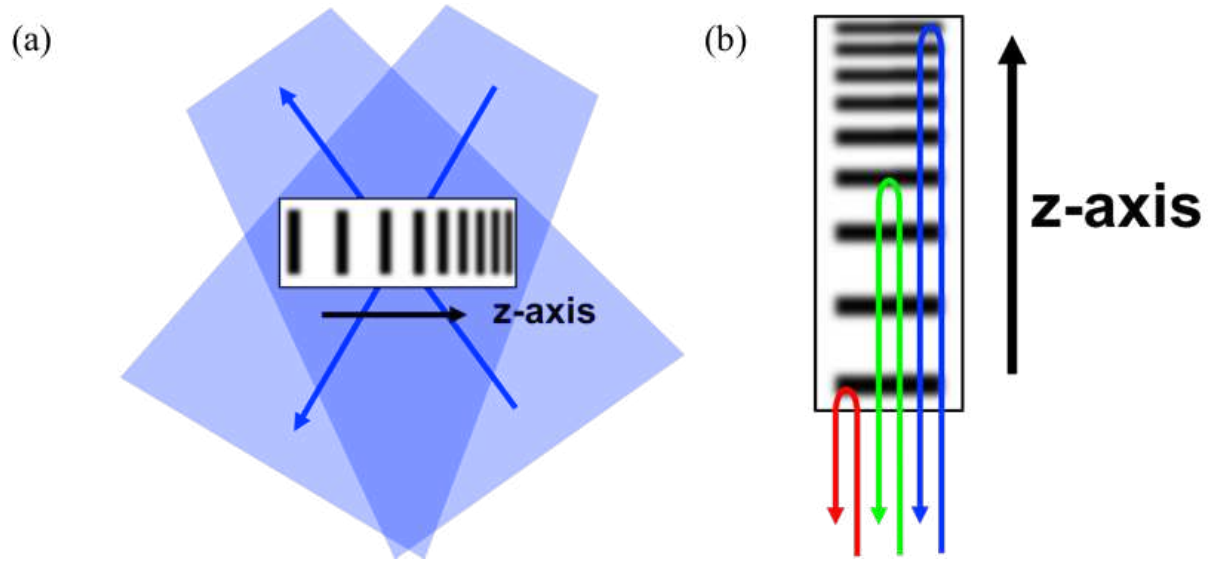

Figure 2.6: a) A schematic showing geometry for producing a CVBG in which equally convergent and divergent beams are used to record linearly varying interference planes. b) An illustration showing how the diffraction of various spectral components within a CVBG create a temporal delay in the pulse.

For uniform Bragg gratings, the planes are recorded by interfering two collimated beams of light in the PTR glass to produce diffraction planes with uniform periodicity. To produce a CVBG, equally convergent and divergent beams are used to record diffraction planes whose period varies linearly. An illustration of this recording geometry is shown in Figure 2.6a. When

the period variation is oriented along the pulse propagation direction, z, the result is a reflecting, CVBG shown in Figure 2.6b, in which the various spectral components of the beam are diffracted from different planes in the bulk and produce an optical path difference.

To understand the reflected spectrum of a CVBG, we first consider a reflection Bragg grating in which the beam is normally incident, i.e. $\theta = 0$, and (2.3) is now, $\lambda = 2n\Lambda$. If there is a period variation of the diffraction planes along the beam propagation direction, $\delta\Lambda/\delta z$, then we obtain the following spectral chirp rate (SCR)

$$SCR = \frac{\delta\lambda}{\delta z} = 2n\frac{\delta\Lambda}{\delta z} \tag{2.4}$$

This condition, along with the grating thickness T, dictates the spectral width of the grating. The total time delay of the grating or the stretched pulse width, t_s , can be determined using the average refractive index of the material, n, and the speed of light, c. The stretched pulse width along with the SCR can be used to characterize the stretch factor, SF, of the CVBG.

$$t_s = \frac{2nT}{c} \tag{2.5}$$

$$SF = \frac{t_s}{\Delta\lambda} = \frac{2n}{cSCR} \tag{2.6}$$

Due to the limited bandwidth available after amplification in the cryogenic regenerative amplifier, the CVBG used for 1 kHz operation was specified with a large stretch factor of 400 ps/nm, yielding a total of 800 ps/nm when used in a double pass configuration.

Figure 2.7a shows a schematic of the pulse stretcher used for 1 kHz operation. The oscillator pulses are seeded through a thin film polarizer (TFP) and are incident on the face of the CVBG which introduces normal dispersion (the red side) at an angle of 3 degrees. The spectrally dispersed, diffracted pulse exits the grating and is then normally incident on a mirror with a quarter-wave plate ($\lambda/4$) before it. The double pass through the waveplate rotates the polarization 90 degrees. The beam then traverses the CVBG once more and exits the stretcher upon re-

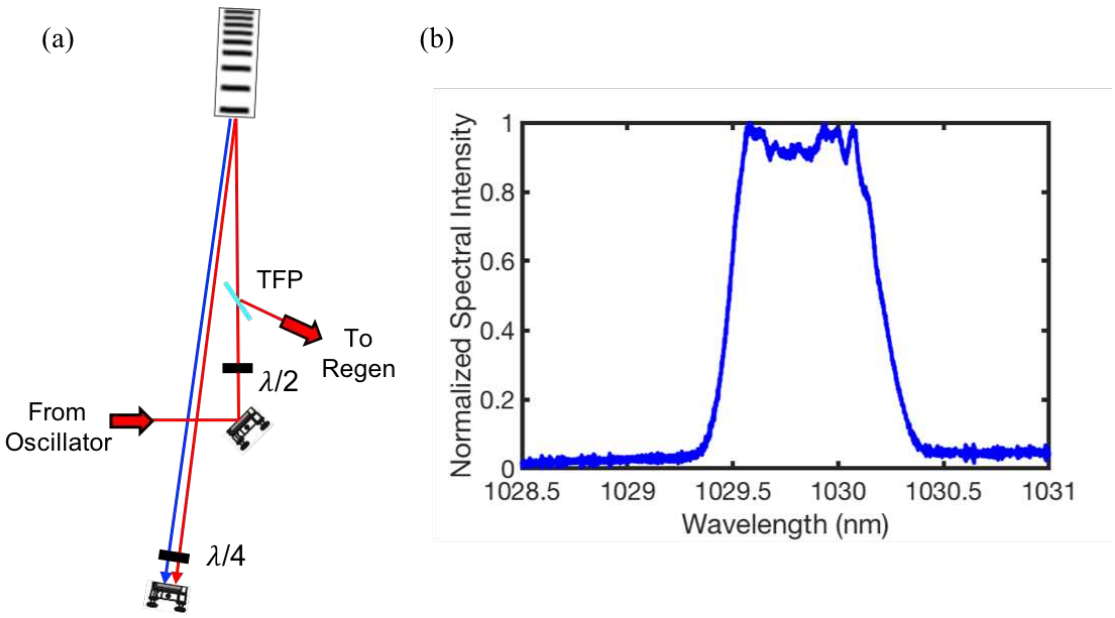

Figure 2.7: a) A diagram showing the beam path through the CVBG stretcher. The beam makes two passes through the CVBG yielding a spatially coherent beam with a stretch factor of 800 ps/nm. TFP: thin film polarizer, $\lambda/2$: half-wave plate, $\lambda/4$: quarter-wave plate b) The stretched pulse spectrum at the exit of the CVBG stretcher optimized for seeding a 1 kHz cryogenic regenerative amplifier. The pulses have a FWHM bandwidth of 0.72 nm.

flection from the TFP. Figure 2.7b shows the typical spectrum at the output of the stretcher. The pulses have a FWHM bandwidth of 0.72 nm and with a specified stretch factor of 400 ps/nm for the CVBG, this yields a stretched pulse duration of 576 ps when double passed. The stretched pulse duration of the beam was not directly measured due to the low intensity but pulse durations of 250 ps were measure with a SHG intensity autocorrelator of the amplified beam exiting the regenerative amplifier where the majority of the gain narrowing occurs.

Figure 2.8 shows the typical spectra of amplified pulses exiting the cryogenic regenerative amplifier used during 1 kHz operation when seeded with either the dielectric grating stretcher, a), or the CVBG stretcher, b). The bandwidth for both cases is comparable with the CVBG stretched pulses having a FWHM bandwidth of 0.26 nm. These pulses were able to be recompressed using the same grating and geometry as the stretcher shown in Figure 2.7a. For compression the stretched pulses were incident on the opposite side of the grating (the blue side),

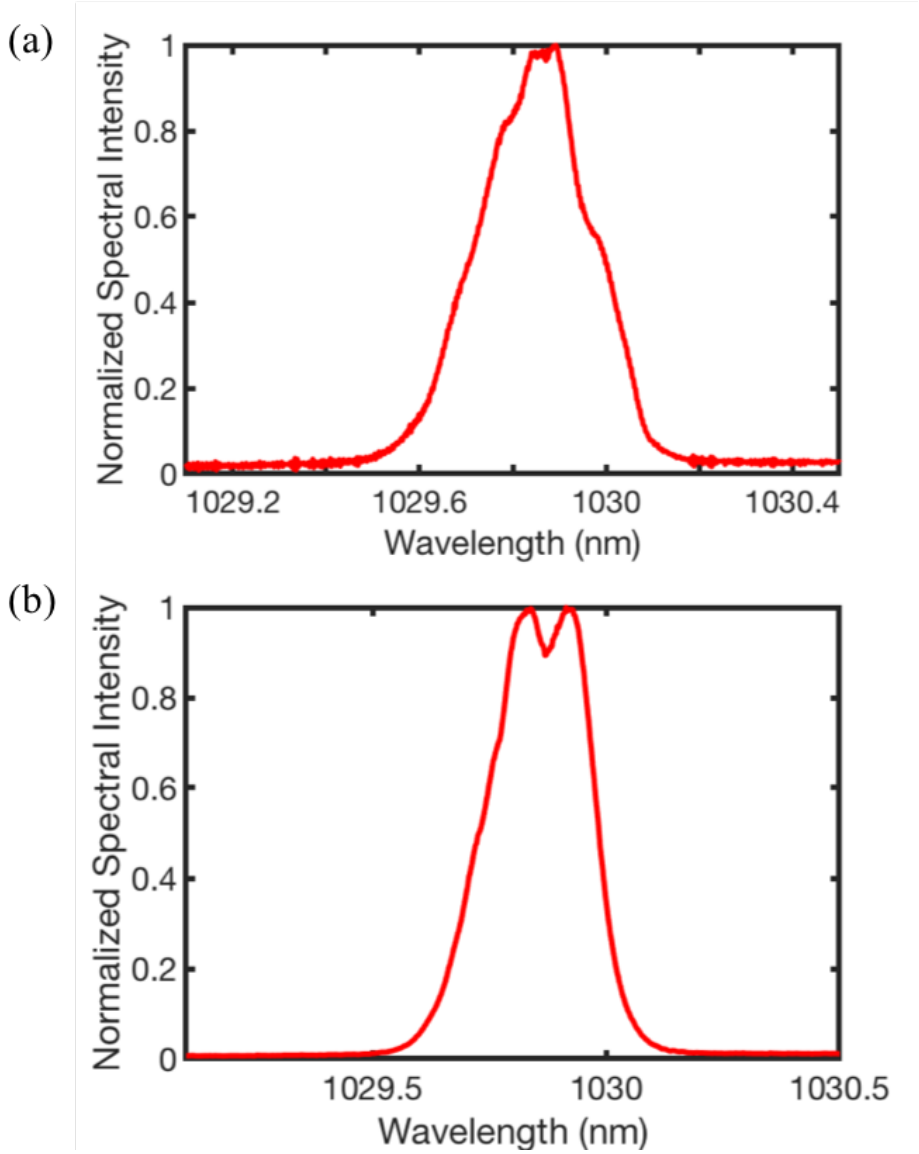

Figure 2.8: The spectra from a cryogenic Yb:YAG, 1 kHz regenerative amplifier when seeded with pulses stretched by a) a dielectric grating stretcher and b) a CVBG stretcher. The pulses have similar amplified bandwidths, 0.22 nm for a) and 0.26 nm for b).

thereby introducing anomalous dispersion to the pulses. The results of this 1 kHz regenerative amplifier and compressor will be discussed later in Section 2.7.1.

CVBGs have several advantages over conventional Treacy style designs. Typical stretcher/ compressor configurations require large aperture, highly uniform diffraction grating with long path lengths to achieve a large stretch factor. This requires expensive optics with a large amount of table space. By contrast, the CVBG used during 1 kHz operation measured 5 x 5 x 40 mm and occupied a table space of only 4 x 20 inches (this could be further reduced by use of smaller optics), and CVBGs are also much less susceptible to misalignment due to vibration because they are monolithic. While many of the same advantages are shared by chirped fiber Bragg gratings [137], their limited apertures constrain their power handling when used as compressors. In contrast, CVBGs with their larger apertures can be used as both a stretcher and compressor, and a single CVBG can be used to accomplished both tasks. [138]

2.4 Regenerative Preamplifier

The first stage of amplification is in a room temperature Yb:YAG regenerative amplifier, Figure 2.9. This amplifier has the highest gain of any in the system and is where pulses can suffer the most gain narrowing. Therefore, the choice was made to use the broader bandwidth available in room temperature Yb:YAG [124, 126] for this amplifier. While the gain is lower than that at cryogenic temperatures, it was not found to be problematic at 500 Hz operation. In fact, the use of room temperature Yb:YAG at this stage allows the spectrum of joule-level pulses exiting the final amplifier, shown later in Figure 2.22, to have nearly double the bandwidth as those exiting a cryogenic regenerative amplifier, shown in Figure 2.8.

Pulses leaving the dielectric grating stretcher pass through a thin film polarizer (TFP), half wave plate ($\lambda/2$), and faraday rotator (FR) combination before being seeded into the regenerative amplifier. This combination functions as an optical isolator and prevents pulses exiting the amplifier from propagating back to the stretcher and oscillator. S polarized pulses are seeded into the cavity via a cavity TFP and are trapped inside the cavity by a $\lambda/4$ waveplate and pockels

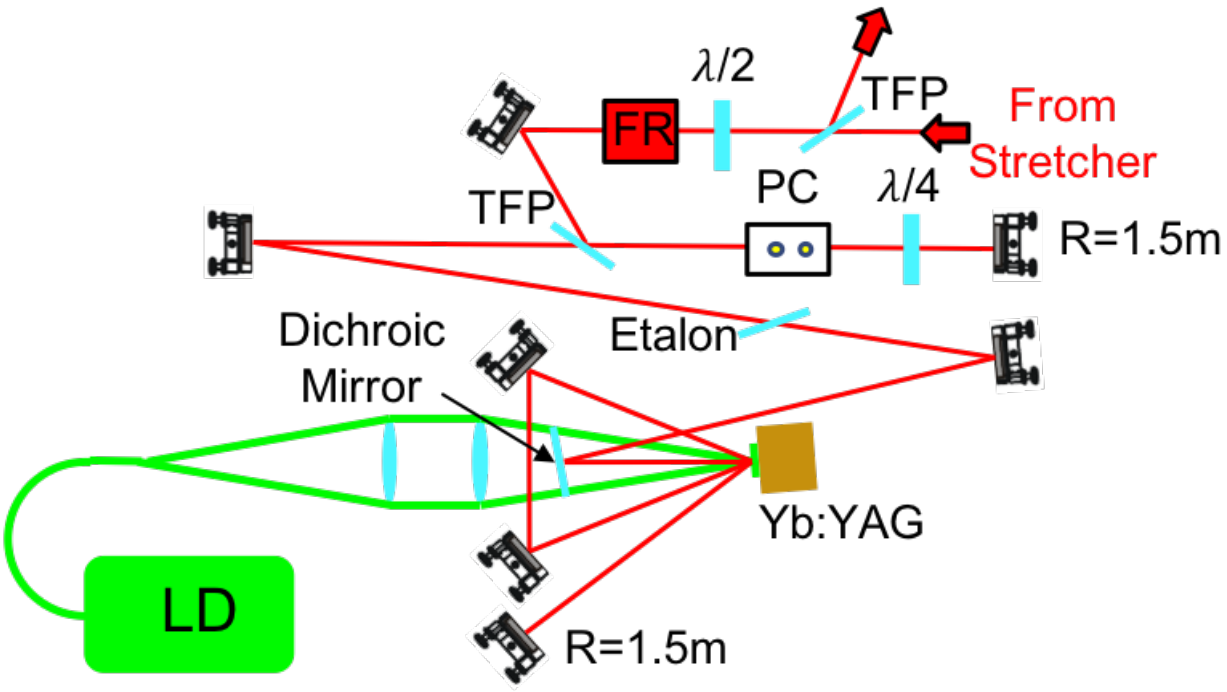

Figure 2.9: A schematic of the 500 Hz regenerative amplifier. $\lambda/2$: half waveplate, FR: faraday rotator $\lambda/4$: quarter waveplate, PC: Pockels cell, TFP: thin film polarizer, LD: laser diode

cell (PC) which rotate the polarization 90 degrees when a $\lambda/4$ wave voltage is applied to the PC. The active medium inside the cavity is 0.5 mm thick 10 %-at. doped Yb:YAG active mirror with a 1 degree wedge to prevent unwanted reflections inside the cavity. The side of the crystal coated as a high reflector is soldered with indium to a water-cooled copper heat sink. The crystal is pumped by a λ = 940 nm, 400 W CW fiber coupled laser diode. The diode output is coupled through a 600 µm core fiber, the end of which is one to one imaged onto the crystal by a pair of f = 10 cm achromatic lenses. The cavity is comprised of two R = 1.5 m spherical end mirrors and flat zero degree and 45-degree mirrors otherwise. The cavity was designed to have a mode size of approximately 700 μm on the Yb:YAG crystal to well match the 600 μm pump spot. The beam makes two passes of the active mirror per cavity single pass allowing for an improved gain to loss ratio. It was necessary to add a thin-film Fabry-Perot etalon with a few nanometers of tunability near 1030 nm when operated around Brewster's angle into the cavity, due to the mismatch of peak wavelength emission between this room temperature amplifier and the subsequent cryogenic amplifiers. [124, 126]

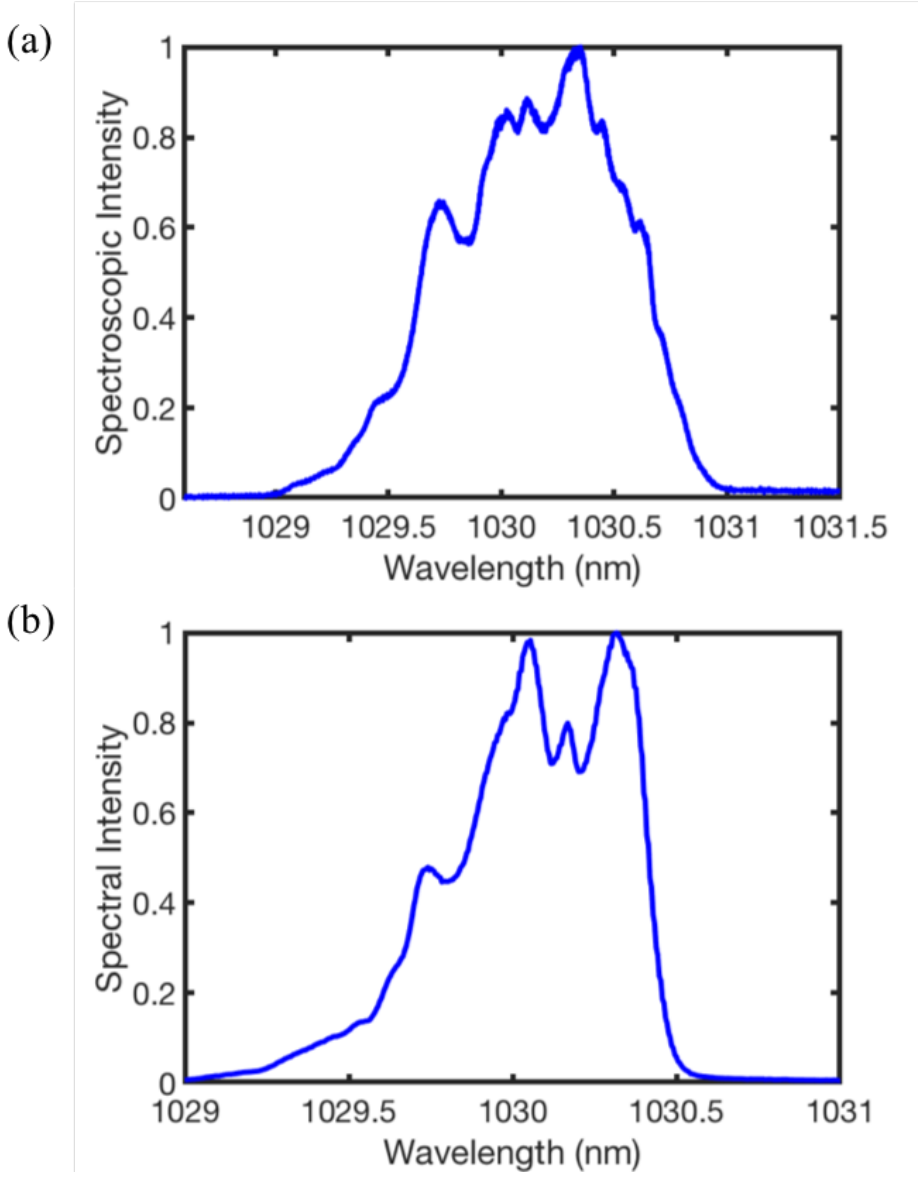

Figure 2.10: a) The spectrum of the beam exiting the room temperature regenerative amplifier with no wavelength tuning. The pulses have a bandwidth of 1 nm which corresponds to transform limit pulse duration of 1.1 ps, assuming a sech^2 pulse shape. b) The spectrum when the wavelength has been optimized for subsequent cryogenic amplification. The FWHM bandwidth is 0.56 nm, corresponding to a transform limit duration of 2 ps.

The amplifier is pumped by 200 W peak power, 200 μs square pulses from the diode laser at a repetition rate of 500 Hz, producing pulses up 1.5 mJ at 500 Hz repetition rate with a wavelength suitable for amplification in subsequent cryogenic amplifiers. Figure 2.10a shows the typical spectrum of the amplifier when the system is "free running", i.e. unoptimized for the following amplification stages. Figure 2.10b shows the wavelength tuned for optimal gain in the following amplifiers. The bandwidth in free running case is approximately 1 nm FWHM and has a transform limit pulse duration of 1.1 ps, assuming a sech^2 pulse shape, while the optimized case has a narrower bandwidth, FWHM of 0.56 nm, which still supports a transform limit duration of 2 ps.

Pulse picking is performed in this stage by the timing circuit which controls the timing of the voltage across the PC. This circuit synchronizes the pulses exiting the oscillator every ~17 ns with the desired 500 Hz timing. Unsynchronized pulses are not trapped in the cavity and make one round trip before exiting with little amplified energy. After reflection from the entrance TFP, these unamplified pulses are removed from the system by a pair of crossed polarized calcite polarizers with a PC between them. The timing of the $\lambda/2$ wave voltage applied across the PC is gated such that only the amplified pulses leaving the regenerative amplifier are transmitted through this system. This temporal gating system has the added benefit of increasing the pulse contrast by removing any "pre" and "post" pulses which may leak out of the amplifier before and after the main pulse, respectively. Furthermore, this gating prevents possible back reflected pulses from the later amplifiers from making their way back to the regenerative amplifier and oscillator, which can significantly reduce the stability of the laser.

2.5 Cryogenic Power Amplifiers

The first cryogenic power amplifier is shown in Figure 2.11. The amplifying medium is composed of a 30 mm x 30 mm x 5 mm Yb:YAG gain medium with a 5 mm thick Cr:YAG cladding optically bonded to the perimeter, making the total dimensions of this composite disk 40 mm x 40 mm x 5 mm. The Cr:YAG acts as an absorber of amplified spontaneous emission (ASE), with

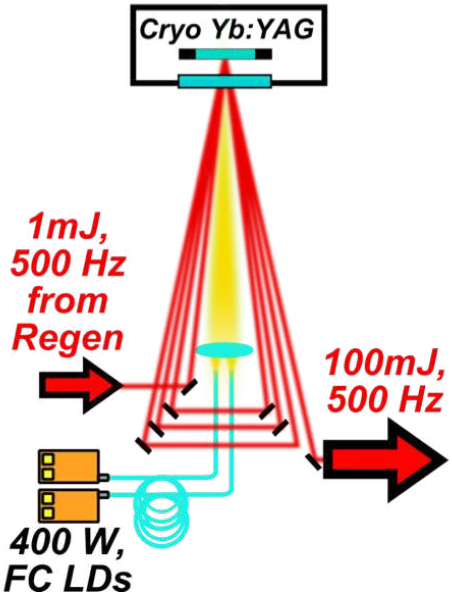

Figure 2.11: A schematic of the beam path through the first cryogenic amplifier. The beam makes four passes of the Yb/Cr:YAG gain disk, which is pumped by two fiber coupled laser diodes (FC LD), before exiting the amplifier with pulse energy as high as 100 mJ. (from [33])

a measured absorption length of 5 cm^{-1}. Due to the index matching between the materials, potential Fresnel reflections at the interface are prevented. The inclusion of this cladding helps prevent depopulation of the upper laser level in the high gain environment.

The disk is placed inside an evacuated chamber and sealed with indium wire. The back face of the crystal is cooled by forced convection with flowing liquid oxygen (LOX) at 77 K by a custom heat exchanger. The disk is pumped by two 400 W fiber coupled laser diodes. The 600 μm fiber ends are imaged into a single 4 mm spot on the laser crystal by two f = 50 mm achromatic lenses (one for each fiber). The diodes are pulsed with 450 μs square pulses with peak powers up to 400 W from each diode. The millijoule-level pulses from the front end of the system are seeded into the amplifier where they make four passes through the gain medium and then exit the amplifier. Figure 2.12 show a measurement of the amplifier's output energy as function of total pump energy incident on the crystal with a maximum of 100 mJ extractible when pumped with 360 mJ at 500 Hz repetition rate.

The pulses suffer gain narrowing during amplification. The spectrum of the 100 mJ pulses, shown in Figure 2.13a, have a FWHM bandwidth of 0.43 nm, supporting a transform limit du-

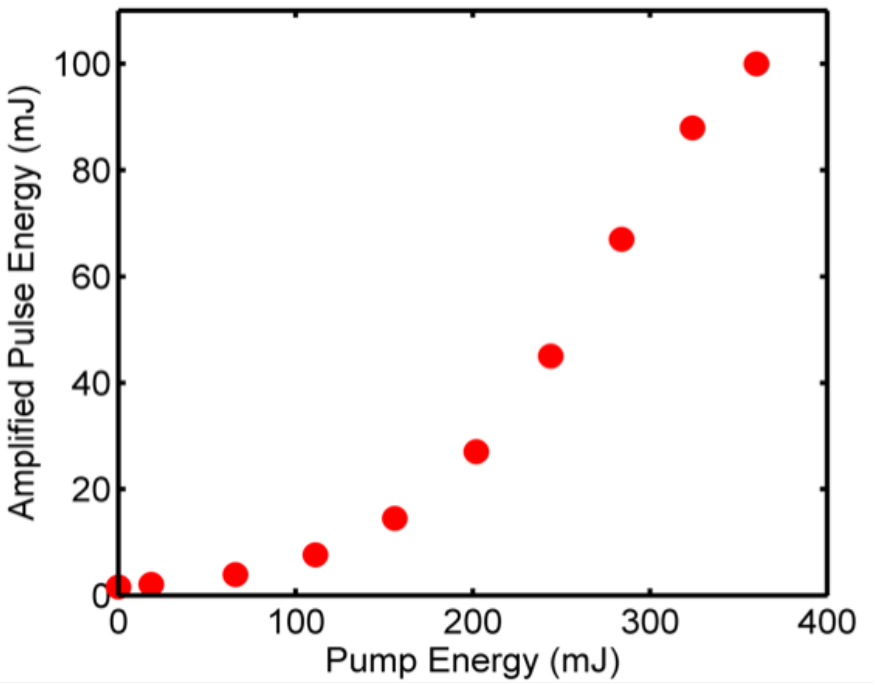

Figure 2.12: Measured pulse energy exiting the first cryogenic amplifier as a function of incident pump energy. A maximum of 100 mJ was obtained at 500 Hz repetition rate.

ration of 2.6 ps (sech^2). The 100 mJ pulses were compressed to 3.8 ps after traversing the subsequent amplifier and dielectric grating compressor, both of which will be described later. Figure 2.13b shows a second harmonic generation (SHG) intensity autocorrelation trace of the amplified pulses and a sech^2 fit.

After exiting the first cryogenic amplifier, the beam passes through a Galilean telescope to increase the beam size. The mode size and divergence of the beam after the telescope were adjusted to optimize the mode matching through the second cryogenic amplifier to account for thermal lensing due to high power pumping. The beam shape is also made to be more flat top before entering the following amplifier to improve extraction efficiency. This is done by including a serrated aperture between the plano-convex and plano-concave lenses of the Galilean telescope. The serrated teeth form a soft aperture and help to avoid high spatial frequency modulations due to diffraction as the beam propagates through the following amplifier.

Following the telescoping and beam shaping, the beam proceeds to the second cryogenic power amplifier which is shown schematically in Figure 2.14. In this final amplifier the P po-

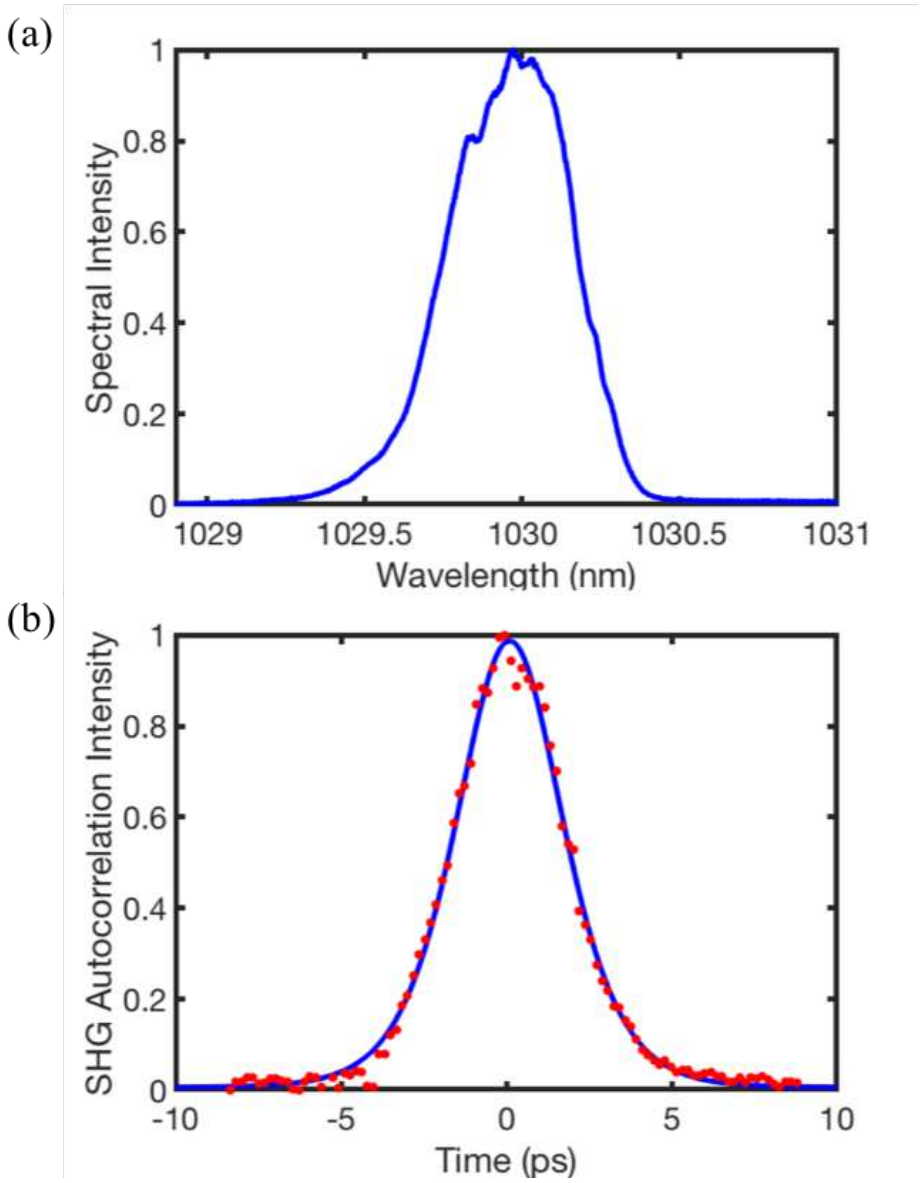

Figure 2.13: a) The spectrum of the second stage. The FWHM bandwidth is 0.43 nm b) The second harmonic (SHG) intensity autocorrelation of the cryogenic preamplifier operating at 100 mJ.

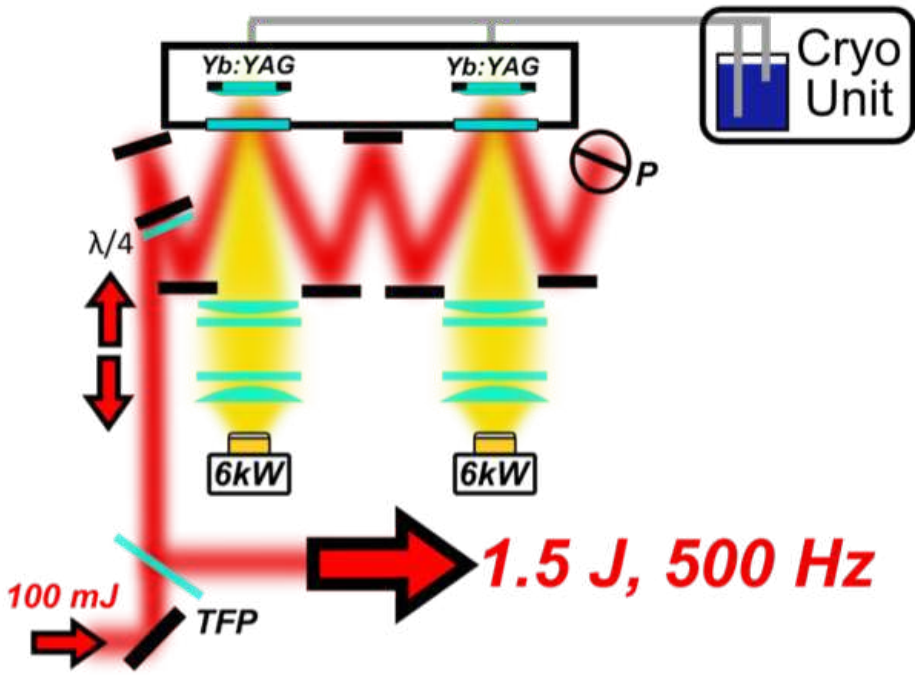

Figure 2.14: Schematic of the beam path through the final cryogenic power amplifier. The beam makes four passes through each composite gain disk, exiting the amplifier with energies up to 1.5 J. (from [33])

larized beam first passes through a TFP set near Brewster's angle. The seed pulses make one bounce off each gain disk before the beam height is changed by a periscope and continues to make one more bounce off each disk. After this second set of bounces, the beam passes through a $\lambda/4$ waveplate, reflects off a zero-degree end mirror, and passes through the $\lambda/4$ waveplate again, thereby rotating its polarization 90 degrees from P to S, retraces the same beam path back through the amplifier, reflects off the TFP, and exits the amplifier.

The custom-made gain disks used in this amplification stage were specially designed to allow for high gain amplification, minimal influence of ASE and parasitic oscillations (PO), and a simplified pump geometry. First, the thickness and doping of the Yb:YAG gain medium was optimized to allow for greater energy storage per pump pass than conventional active mirror thin disk laser amplifiers. Many laser amplifiers utilizing an active mirror geometry are "thin disk" lasers, using crystal thicknesses of 100-200 μm with high aspect ratios. The large aperture face of the crystal provides a large surface for cooling and the limited thickness provides a short conduction path, allowing for highly efficient heat removal with limited transverse thermal gra-

dients. Although, the thin disk design presents a number of limitations when trying to scale to high pulse energy. The high aspect ratio creates significant transverse gain in the crystal. This creates a long gain path for ASE and if precautions are not taken to eliminate surface reflections due to index differences, PO can further reduce the energy storage in the gain region. Therefore, a thin disk with simultaneously high gain is difficult to achieve. Along with limitations in achievable gain, only a limited amount of pump energy can be stored per pass due to the short absorption length of the crystal. To store an adequate amount of pump energy in a thin disk amplifier design, complex pumping schemes are employed to reimage unabsorbed pump light back to the gain region and typically require 12 to 24 passes of the pump light on the crystal. Therefore, the design of the gain disks in this final amplification stage sought to preserve the beneficial thermal properties of a thin disk active mirror geometry, while allowing for high energy storage with a simplified pump design.

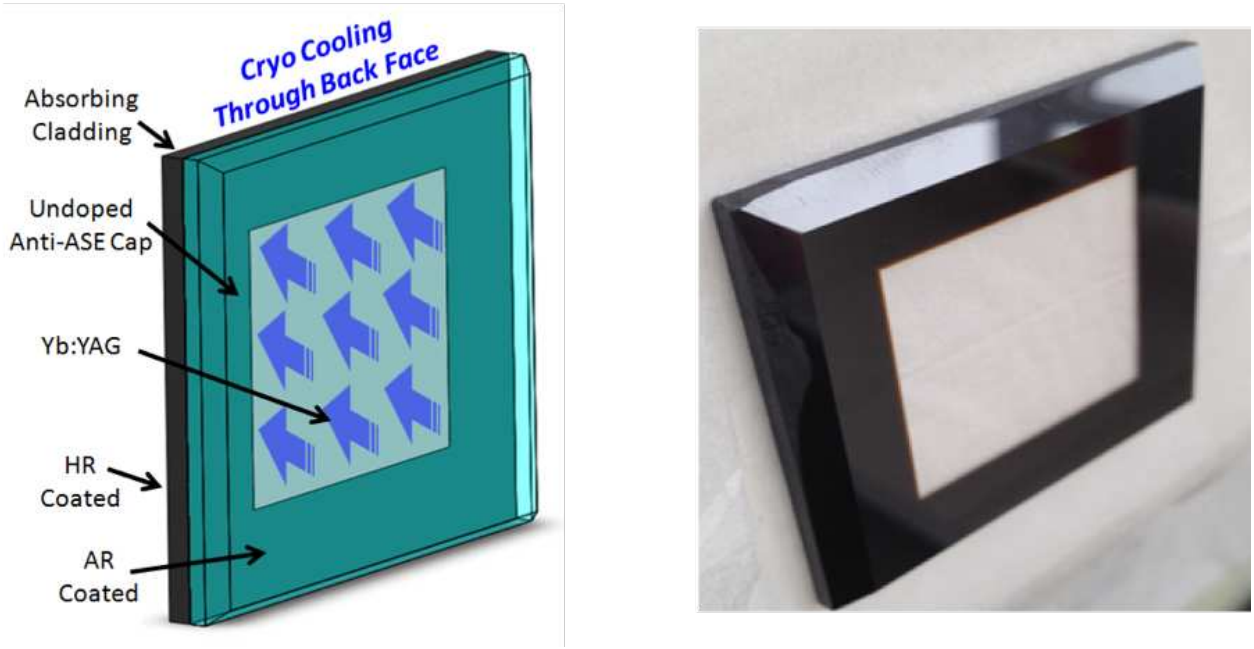

Figure 2.15: a) A schematic showing the composition of the custom designed gain disks used in the final stage of amplification. b) A photograph showing the composite gain disk.

The gain disks in this final amplifier are a custom composite of Yb:YAG, Cr:YAG, and undoped YAG. An illustration showing the composition of the various materials is shown in Fig-

ure 2.15a while a picture of the disk is shown in Figure 2.15b. The gain medium is a slab of single crystal 3%-at. doped Yb:YAG whose lateral dimensions measure 30 mm x 30 mm and a thickness of 2 mm. A 10 mm section of Cr:YAG is optically bonded to all lateral faces of the gain medium and atop the Yb/Cr:YAG assembly, a 3 mm thick undoped YAG endcap is optically bonded. The absorption of the Cr:YAG was measured to be 5 cm^{-1} at 1030 nm, allowing for greater than 99 % absorption of ASE in a 10 mm path length. The addition of an undoped YAG end cap has been shown to further suppress the role of PO in thin disk lasers [139–141] by eliminating the index difference between the host material and the environment on the large surface area front face of the crystal. The near index matched endcap reduces the solid angle over which spontaneously emitted photons can be trapped by total internal reflections at interfaces where index differences exist. This allows the transverse dimension of the crystal to be larger without concern that ASE will suppress gain. The endcap of the crystals was also beveled to help direct spontaneously emitted photons into the absorbing Cr:YAG cladding. This end cap also increases the structural integrity of the gain disk, making it less susceptible to wavefront distortions which can occur when compressing the indium wire used to seal the crystal in vacuum at cryogenic temperatures. It also prevents potential wavefront distortions or possible fracture from the pressure difference between the flowing cryogen on the back surface and the high vacuum on the front surface. The back face of the disks is HR coated for λ = 940 and 1030 nm while the front surface is AR coated for the same wavelengths.

Each disk in the amplifier is pumped by a λ = 940 nm, 6 kW diode array. The emission from the diode comes from sixty 100 W bars which are stacked vertically. In total the emission region from the diode stack measures 1 cm x 10 cm and has a divergence angle of 8 degrees FWHM along the slow axis (horizontal) and 0.25 degrees FWHM along the fast axis (vertical). Therefore, a pump shaping and imaging system was designed to collect the divergent light emitted from the bars, homogenize the light, and re-image it into a near flat top pump profile on the crystal.

An illustration of the focusing optics is shown in Figure 2.16. The vertical axis of the diodes is collected and down telescoped by a f = 350 mm and f = -50 mm cylindrical lens pair. The

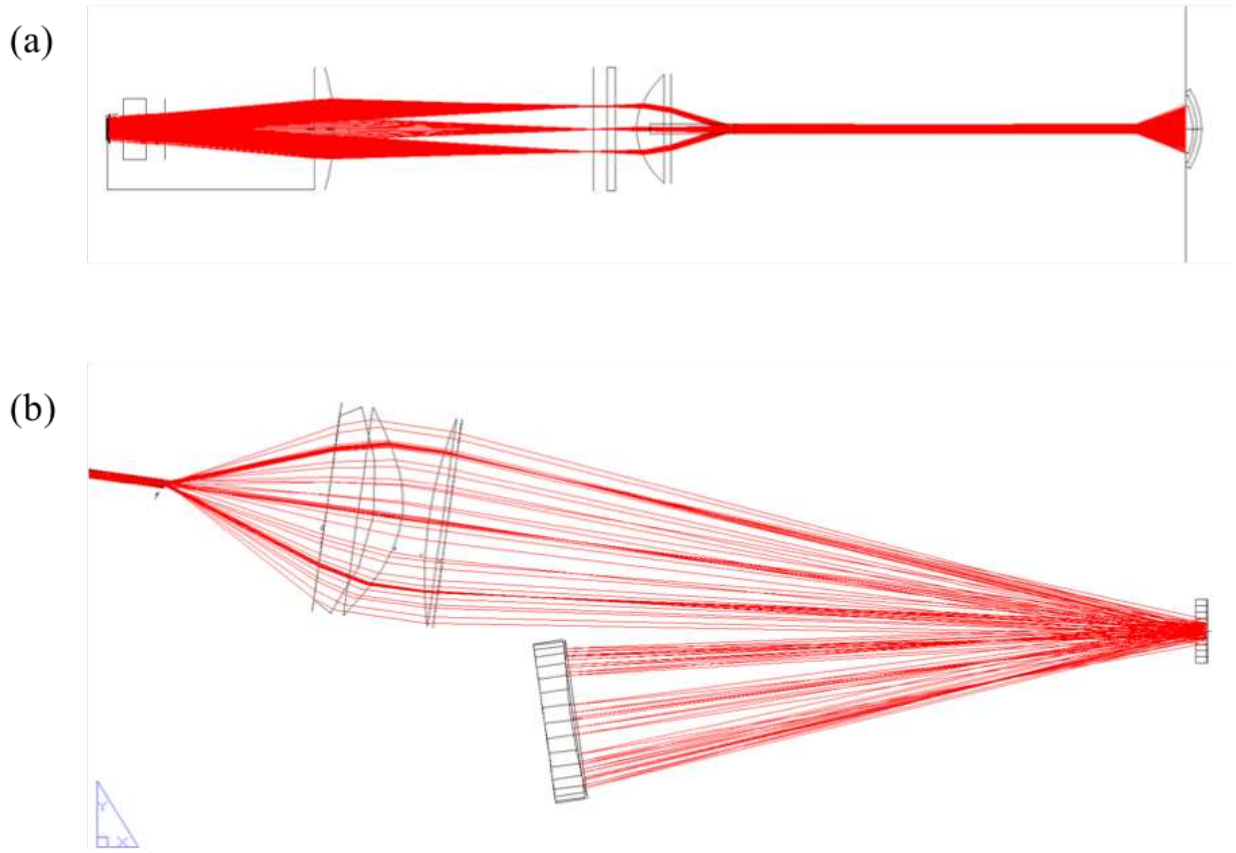

Figure 2.16: A top down view of the pump optics a) This shows the first part of the pump imaging system. On the left is the emission from the diode bars which is collected and focused into the homogenizing rod. The rays reflect within the rod and are reemitted on the right side of the image. b) This shows the second part of the imaging system. The rays emitted from the rod at the top left of the figure are imaged onto the crystal surface at the right of the figure by a 4x magnifying telescope at an angle of 15 degrees. The unabsorbed rays are then re-imaged onto the crystal by the spherical concave mirror at the bottom of the figure.

horizontal axis is initially collimated by a single f = 170 mm cylindrical lens. Both axes are then focused into a 100 mm long fused silica rod by a f = 50 achromatic lens. Within the rod total internal reflections from the outer surface homogenize the light, but due to the limited commercial availability of high quality round fused silica rods, the rod was hexagonal with an edge to edge diameter of 4 mm. It was necessary to place a 5 degree holographic UV diffuser to produce a uniform image at the crystal surface. The output of the rod is then re-imaged and magnified 4x onto the crystal by a pair of f = 50 mm and a f = 200 mm spherical lenses to a 16 mm (edge to edge) flat top spot on each disk.

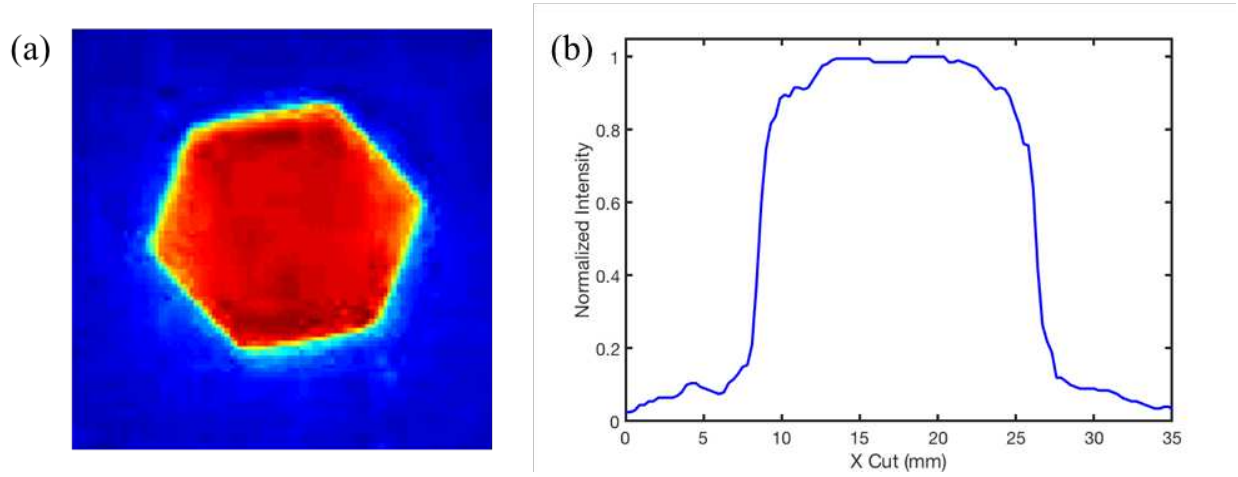

Figure 2.17: a) An image of the pump spot fluorescence from the final cryogenic amplifier. The spot is approximately 16 mm from edge to edge. b) A one-dimensional cut of the pump profile. This illustrates the highly flat top profile of the pump region.

An image of the pump spot on the crystal is shown in Figure 2.17a with a 1D cut to illustrate the highly flat top nature of the pump region, Figure 2.17b. The pump radiation is incident on the crystal at an angle of 15 degrees. To simplify pump alignment and maintain the desired incident angle, a 10 degree wedge was placed between the spherical lenses used to re-image the homogenizing rod. The unabsorbed pump radiation is relay imaged back onto the crystal with an f = 150 mm spherical concave mirror. With this simple two pass pumping scheme and appropriately designed gain disks, greater than 90% of the pump radiation is absorbed. It avoids

the pump complexity inherent in a thin disk amplifier or the need for the high doping concentration, which can significantly reduce thermal conductivity at cryogenic temperatures [114].

During laser operation, the laser diode arrays were pulsed with 500 µs pulses at a repetition rate of 500 Hz, and ~60 mJ of pulse energy was seeded into the final 8-pass amplifier. The output energy of this amplifier as a function of total energy supplied to both disks is shown in Figure 2.18. At the maximum pump energy of 4 J, 1.5 J (750 W) of pulse energy was obtained, corresponding to an optical-to-optical efficiency of 37 %. Slight thermal lensing was observed when operating at high power and this was compensated by increasing the input divergence into the final amplifier with the Galilean telescope before the TFP. The thermal lensing in the amplifier was measured to be less than 200 m for a single pass through each crystal, and no depolarization loss was observed.

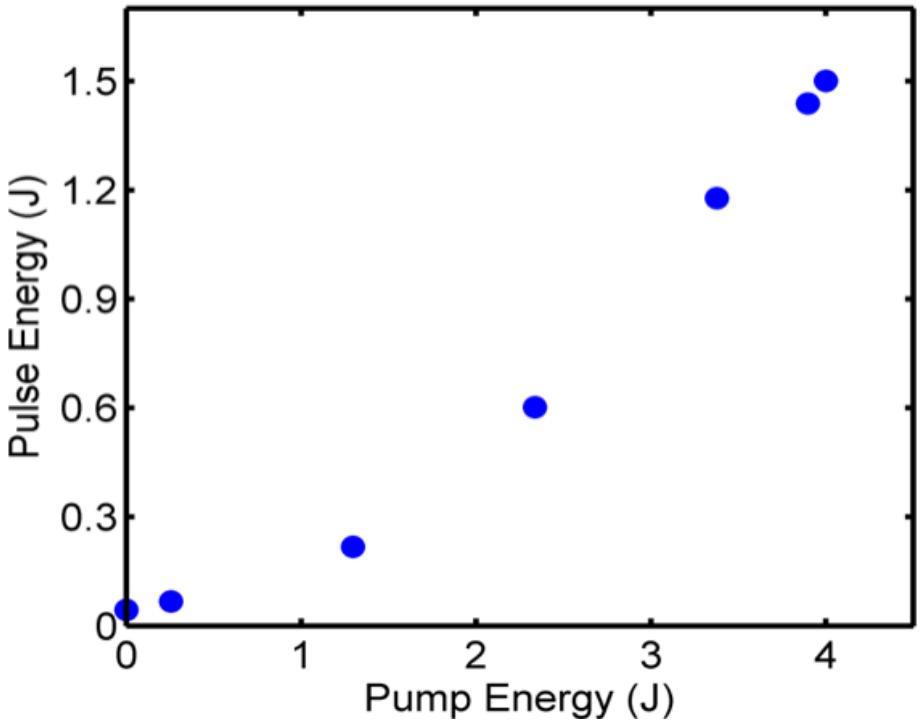

Figure 2.18: Measured output pulse energy as a function of total pulse energy incident of the two gain disks at 500 Hz repetition rate. 1.5 J of energy was obtained when 4 J of pump energy was incident on the disks, yielding an optical to optical efficiency of 37 %.

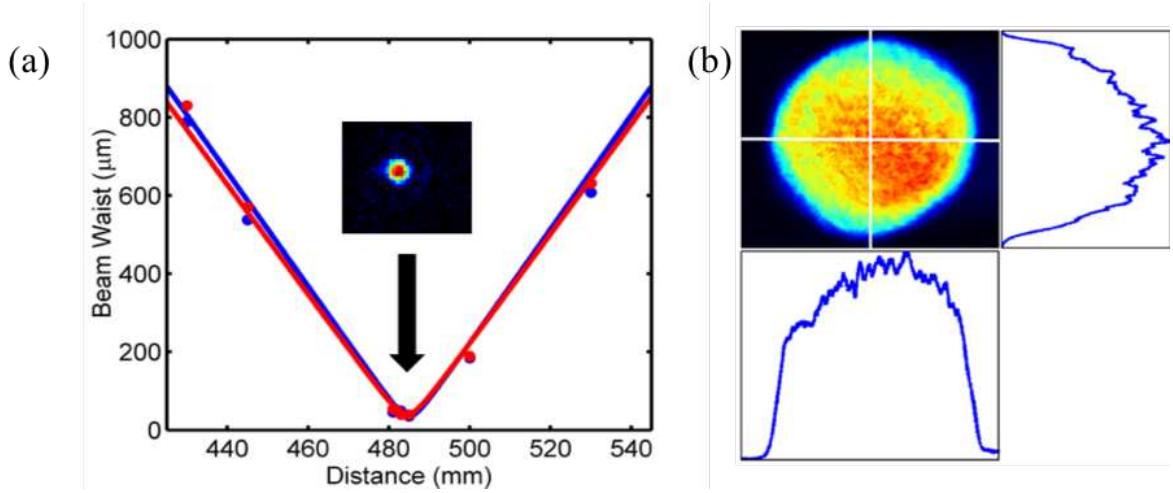

Figure 2.19: a) An M^2 measurement of the beam exiting the final amplifier. This measurement was performed with the laser operating at 1.4 J and 500 Hz repetition rate. Inset is an image of the far field beam. b) An image of the near field laser beam with 1.4 J of pulse energy at 500 Hz repetition rate with x (below) and y (right) profile cuts through the beam center.

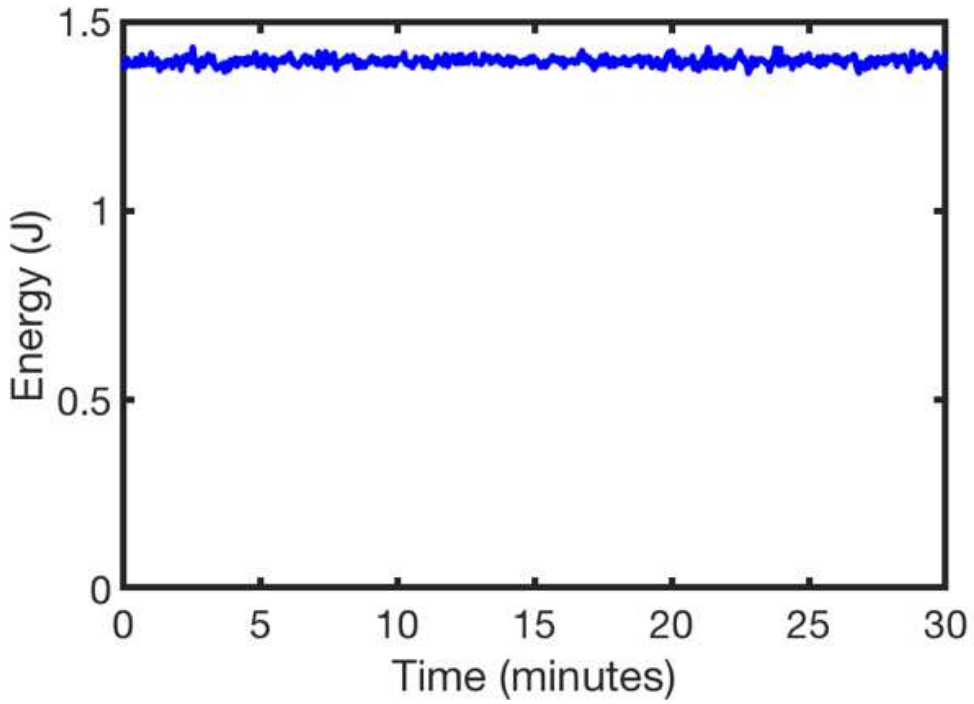

Figure 2.20: A continuous measurement of pulse energy over a 30-minute period. The average pulse energy during this run was 1.41 J with a standard deviation of 0.75 %.

The laser demonstrated excellent beam quality during high power operation. Figure 2.19a shows the results of an M^2 measurement. Here, a f = 500 mm plano-convex lens was used to focus the attenuated output laser beam operating at 1.4 J and a camera on a linear translation stage was used to capture images of the beam as it went through a focus. The 4σ pulse widths along the x (horizontal) and y (vertical) axes were determined from these images and a least squares fit was made to the Gaussian beam propagation equation to determine an M^2 value for the beam. The M^2 for the x and y axes were determined to be 1.25 and 1.31, respectively, and this measurement also shows the lack of astigmatism present in the beam. The excellent beam quality from the laser is further demonstrated by the far-field beam image, inset into Figure 2.19a, as well as the near-field image shown in Figure 2.19b. The near-field beam shows a highly flat top beam that is free of any hot spots.

Figure 2.20 shows the pulse to pulse energy fluctuations over a 30 minutes period of continuous laser operation. During this run, the laser fired 900,000 consecutive shots with an average energy of 1.4 J and a standard deviation of 0.75 % over the entire run. This standard deviation approaches the 0.5 % shot to shot repeatability of the Newport 818E energy detector used to make the measurement.

2.6 Dielectric Grating Compressor

The pulse compressor, shown in Figure 2.21, is a Treacy style compressor, providing anomalous dispersion and consists of two high damage threshold 1740 mm^{-1} gratings, a roof mirror (RM), and two fold mirrors. Prior to entering the compressor, the beam is expanded with a Galilean telescope to a diameter of 40 mm and is incident on the first grating at an angle of 55.5 degree which creates a footprint of 22.5 cm^2 on the first grating. For the 1.4 J beam, this corresponds to a fluence of 1.96×10^{-2} J/cm^2 and poses a limited risk for optical damage. Upon diffraction from the first grating, the beam travels 2.18 m before it is incident on the second grating. After, the beam changes height via a roof mirror, retraces the same path, and passes directly above the input mirror before exiting the compressor. Two fold mirrors are placed be-

tween the two gratings to provide the necessary path length for full dispersion compensation and minimizes the footprint of the compressor. All compression is done in vacuum to minimize the risk of damage to the gratings. At the grating angle used for optimal compression, the gratings have a first order efficiency of 92 % which corresponds to a throughput efficiency of 72 %. This takes the 1.4 J uncompressed pulses at 500 Hz to 1 J at the output.

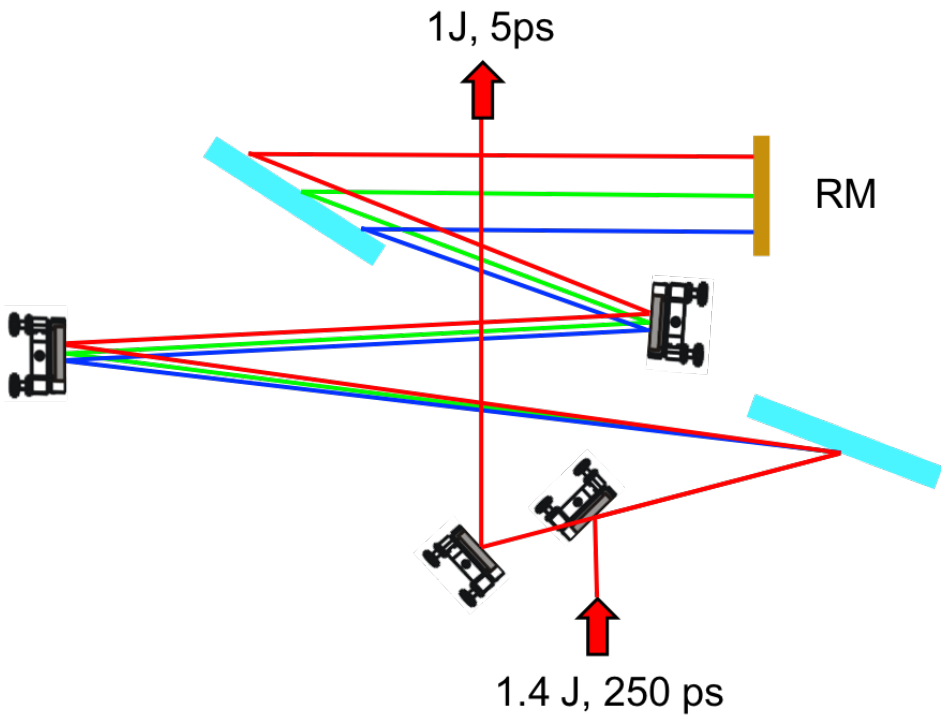

Figure 2.21: A schematic of the pulse grating stretcher illustrating the beam paths of the various spectral components. roof mirror (RM)

While an autocorrelation measurement was not performed on the fully amplified pulses due to the logistical difficulty in attenuating the 500 W beam exiting the compressor, Figure 2.22 shows that limited additional gain narrowing occurs through this final stage of amplification. Amplified pulses exiting the final amplifier had a FWHM bandwidth of 0.36 nm, which is enough to support pulse durations as short as 3.1 ps (sech^2). Figure 2.13b shows the intensity autocorrelation trace of the 100 mJ (pre-compression energy) beam traversing the entire laser system. This lower power beam was compressed to a sech^2 FWHM duration of 3.8 ps having only 7

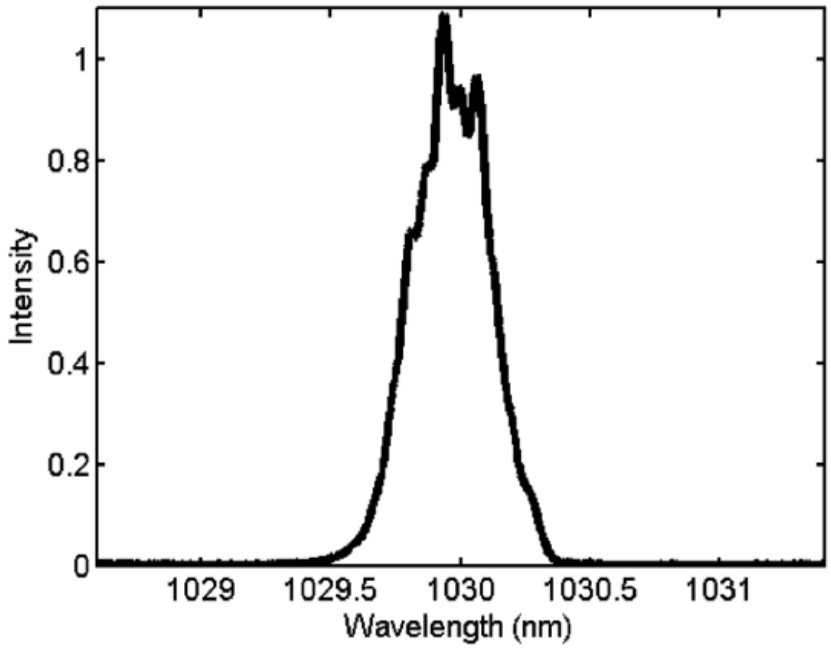

Figure 2.22: The measured spectrum of the fully amplified beam exiting the final amplification stage. The FWHM bandwidth was measured to be 0.36 nm which supports sech^2 pulse durations of 3.1 ps.

angstroms more bandwidth than the fully amplified beam. Therefore, similar compression can be expected at full power.

2.7 1 kHz Joule-level Laser Demonstration

In order to scale the laser system to Joule level pulse energies at 1 kHz repetition rate, several changes were made to the 500 Hz system. These changes include redesigning the regenerative amplifier and adding an additional stage of power amplification. The redesign of the regenerative amplifier constituted the largest change necessary for 1 kHz operation. These modifications included operating at cryogenic temperatures rather than room temperature, incorporating a new cavity design, and improvements to the soldered crystal heat sink.

2.7.1 Cryogenic Regenerative Amplifier

The most notable change to this amplification stage is the cryogenic cooling of the gain material. While the room temperature regenerative amplifier enables broader bandwidth, it suffers

from low gain and an emission wavelength that is mismatched to the subsequent cryogenic amplifiers. For these reasons, it was found that cryogenic cooling of the gain material was the simplest step towards operation at 1 kHz repetition rate. Other alternatives exist which have the potential for simultaneously broad bandwidth and high pulse energy but required more intensive design and testing. Some of the options currently under investigation include a jet-impinged, water-cooled thin disk Yb:YAG amplifier and a cryogenically cooled Yb:KYW amplifier. These will be discussed in Section 2.9.

A new gain module was developed to enable operation at cryogenic temperatures. Similar to the 500 Hz laser system, the HR side of a 1 degree wedged, 0.5 mm thick, 10 %-at. doped Yb:YAG disk was soldered to a heat sink. Instead of soldering to copper, the Yb:YAG crystal was soldered with indium to a 75/25 (W/Cu) heat sink. While CuW has a lower thermal conductivity than pure copper, its coefficient of thermal expansion is better matched to that of YAG, helping to mitigate thermally induced stress during the soldering process. [128] This CuW heat sink is thermally contacted with indium to another copper heat sink which has atmospheric LN2 flowing through it. This entire assembly is then placed into an evacuated chamber and positioned as an active mirror in the cavity.

Figure 2.23a shows a schematic of the new regenerative amplifier while Figure 2.23b shows the mode size throughout the cavity. The new cavity is more simplified, reducing alignment complication, and allowed for a larger mode size in the cavity, which was possible due to the higher gain of cryogenic Yb:YAG. A larger mode cavity was found to be crucial when scaling to higher repetition rates because damage to the interface between the crystal and solder was found to be a leading cause for optically induced damage. Now the cavity consists of a flat and R = 1.5 m spherical mirror as the cavity end mirrors and provides a mode size of ~1 mm in diameter at the crystal as well as at the pockels cell, >2 mm. The crystal is pumped by the same 400 W peak power fiber coupled laser diode but now the 600 μm core fiber is magnified to a flat top pump spot size of 1.8 mm by a pair of achromatic lenses of focal lengths f = 100 mm and f = 200 mm. This reduces the average pump intensity by over an order of magnitude and maintains

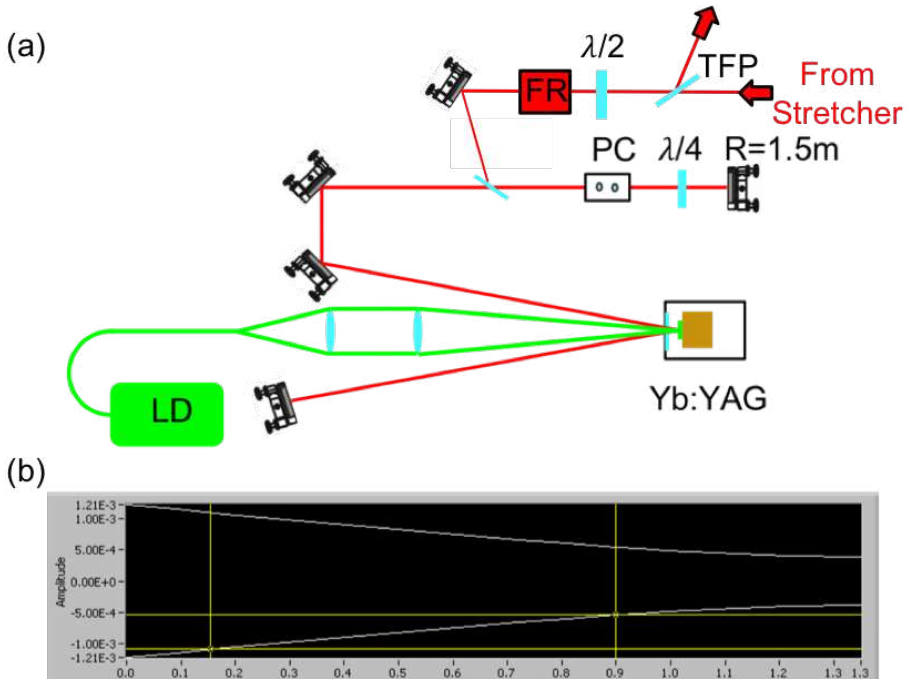

Figure 2.23: a) A schematic illustrating the 1 kHz, cryogenic regenerative amplifier. b) A plot showing mode size throughout the 1 kHz cavity. The R = 1.5 m end mirror is located at position 0 along the x-axis. The vertical cursors indicate the pockels cell, located at x = 0.15 m, and the crystal, located at x = 0.9 m.

the seed pulse fluence, of ~0.5 J/cm^2 at the maximum extractible pulse energy, on the crystal and has improved the lifetime of the crystal solder interface.

With this updated amplifier design, pulse energies exceeding 4 mJ have been obtained with peak pump powers of 100 W and pump pulse durations of 100 μs. Furthermore, the wavelength of the amplified beam is inherently matched to that of the subsequent amplifiers and eliminates the need for an intracavity etalon which was a large source of loss in the cavity.

While the amplifier boasts significantly more energy it now suffers more gain narrowing. Figure 2.8b shows the output spectrum of the amplified pulses with a FWHM bandwidth of 0.26 nm, approximately 47 % of that obtained at 500 Hz. The amplified pulses were compressed using a CVBG compressor whose alignment was identical to that shown in Figure 2.7a except that the amplified stretched pulse was incident on the opposite side of the CVBG. In this way, the pulses experience anomalous dispersion and are recompressed to near their transform limit and have been compressed to sub 10 ps durations, as shown in Figure 2.24. These pulses were measured to have a compressed pulse duration of 8.4 ps FWHM (sech^2).

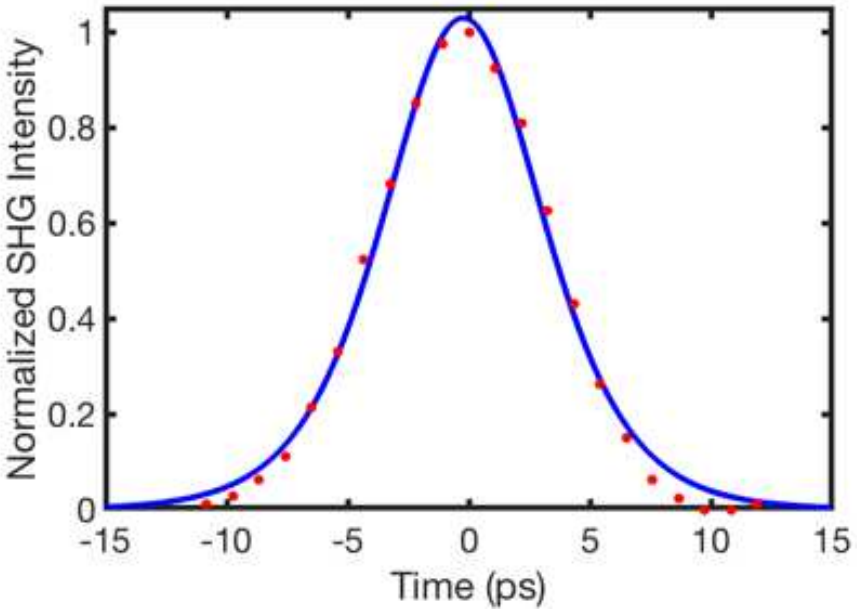

Figure 2.24: The acquired SHG intensity autocorrelation trace of the compressed cryogenic regenerative amplifier. A sech^2 fit indicates a compressed pulse duration of 8.4 ps FWHM.

2.7.2 Cryogenic Power Amplifiers

The first cryogenic power amplifying stage, as detailed in Section 2.5, was altered when transitioning from 500 Hz to the initial 1 kHz demonstration. The amplifier was again seeded with millijoule level pulses from the regenerative amplifier and pumped by the same two fiber coupled laser diode with pulse durations of 450 µs, now at 1 kHz repetition rate. Instead of the four-pass configuration used at 500 Hz, an additional pass was added to maintain an extraction energy comparable to that which was obtained at 500 Hz. A lower single pass gain was required in order to minimize the effects of thermal lensing in the amplifier which became pronounced at high pump powers.

Figure 2.25a shows the output pulse energy as a function of incident pump energy. 67 mJ was obtained from 270 mJ of pump energy with good beam quality. Figure 2.25b shows the amplifier operating at an average pulse energy of 67 mJ at 1 kHz repetition rate for a continuous 30 minute run. The amplifier displays excellent stability with a standard deviation of 0.6 % for the entire run. Following this stage, the beam is again made to be more flat top with a

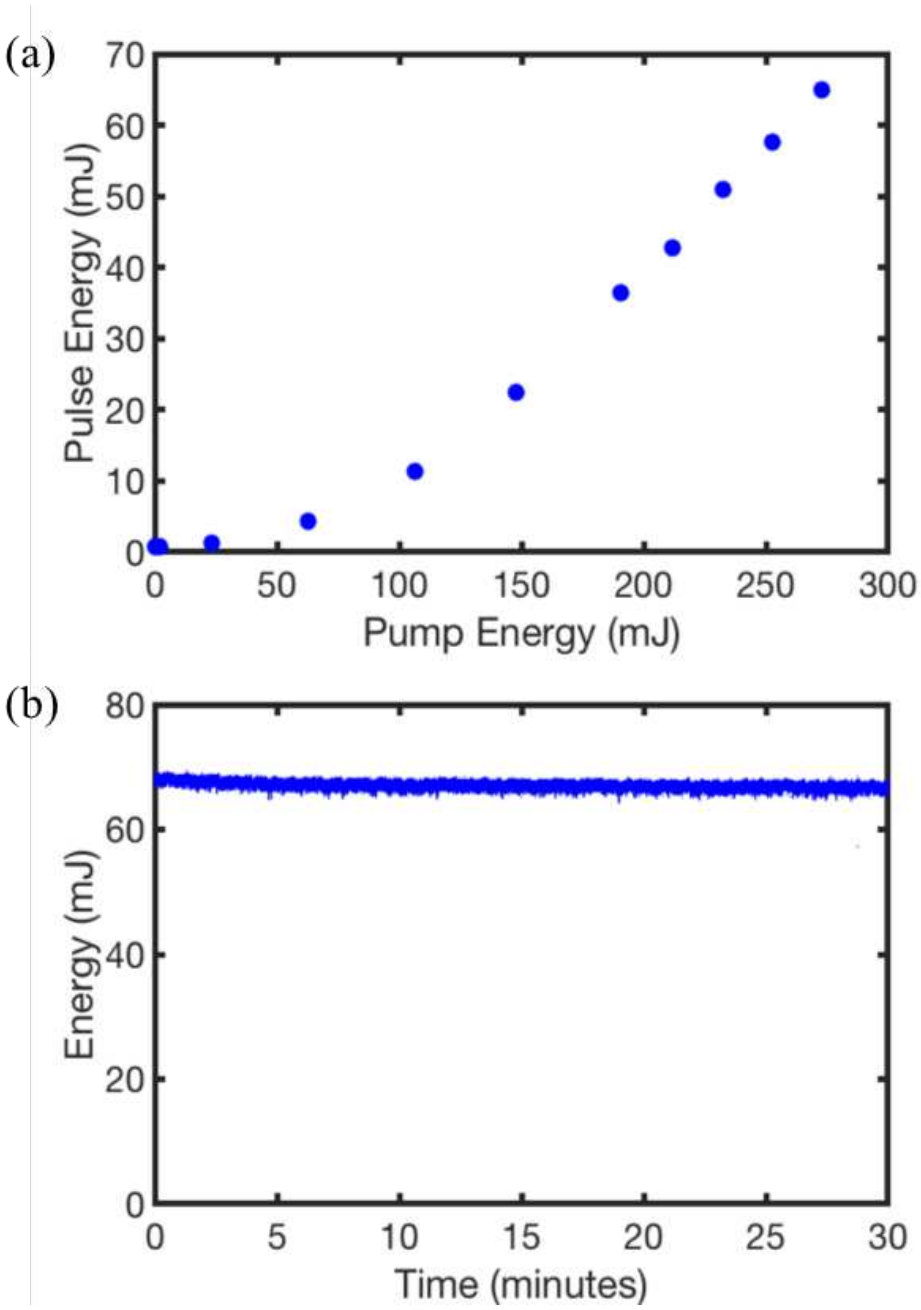

Figure 2.25: a) Pulse energy at the output of the first cryogenic amplification stage operating at 1 kHz. b) A plot of 30 minutes of continuous laser operation at an energy of 67 mJ at 1 kHz. The laser was measured to have a standard deviation of 0.6 % during this period.

serrated aperture between the lenses of a magnifying telescope. The throughput of this system is approximately 70 % allowing the next amplifier to be seeded with a pulse energy of ~45 mJ.

During the initial operation at 1 kHz, an additional cryogenic cooling unit, amplifier head, and pump optics were added to the existing system. All of these components were identical to those used in the final amplifier of the 500 Hz laser system and detailed in Section 2.5. Figure 2.26 is a diagram of the final two amplification stages used to obtain joule level pulses at 1 kHz repetition rate. The ~45 mJ beam from the previous amplifier is seeded through a TFP where the beam makes two passes of each crystal before its polarization is rotated, reflects from a zero degree send back mirror, and retraces the same beam path, exiting the amplifier upon reflection from the TFP. In total, the beam makes eight passes of the two crystals in the same geometry as was used in the final 500 Hz amplifier.

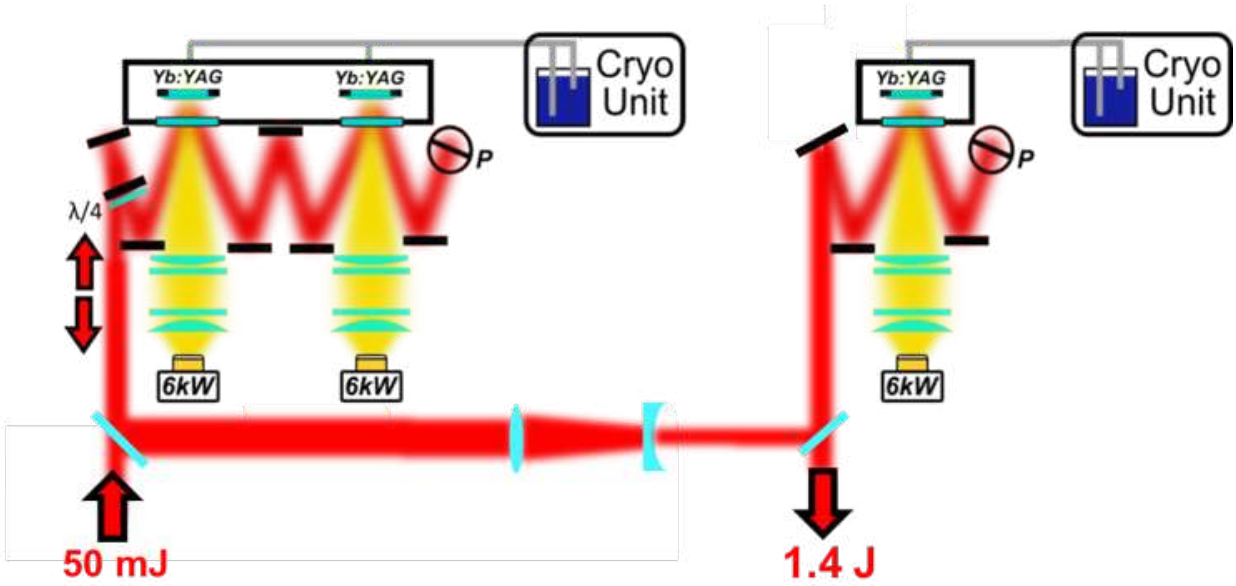

Figure 2.26: A schematic of the the high power laser implemented with two cryogenic amplification stages. The initial stage uses the same 8-pass beam path as was used during 500 Hz operation and in last stage the beam makes two passes through the composite gain disk.

Figure 2.27a shows the performance of the 8-pass cryogenic amplifier operating at 1 kHz repetition rate. In this run a maximum of 840 mJ was achieved with an incident pump energy of 2.5 J which corresponds to an optical to optical efficiency of 36 %. This amplifier has

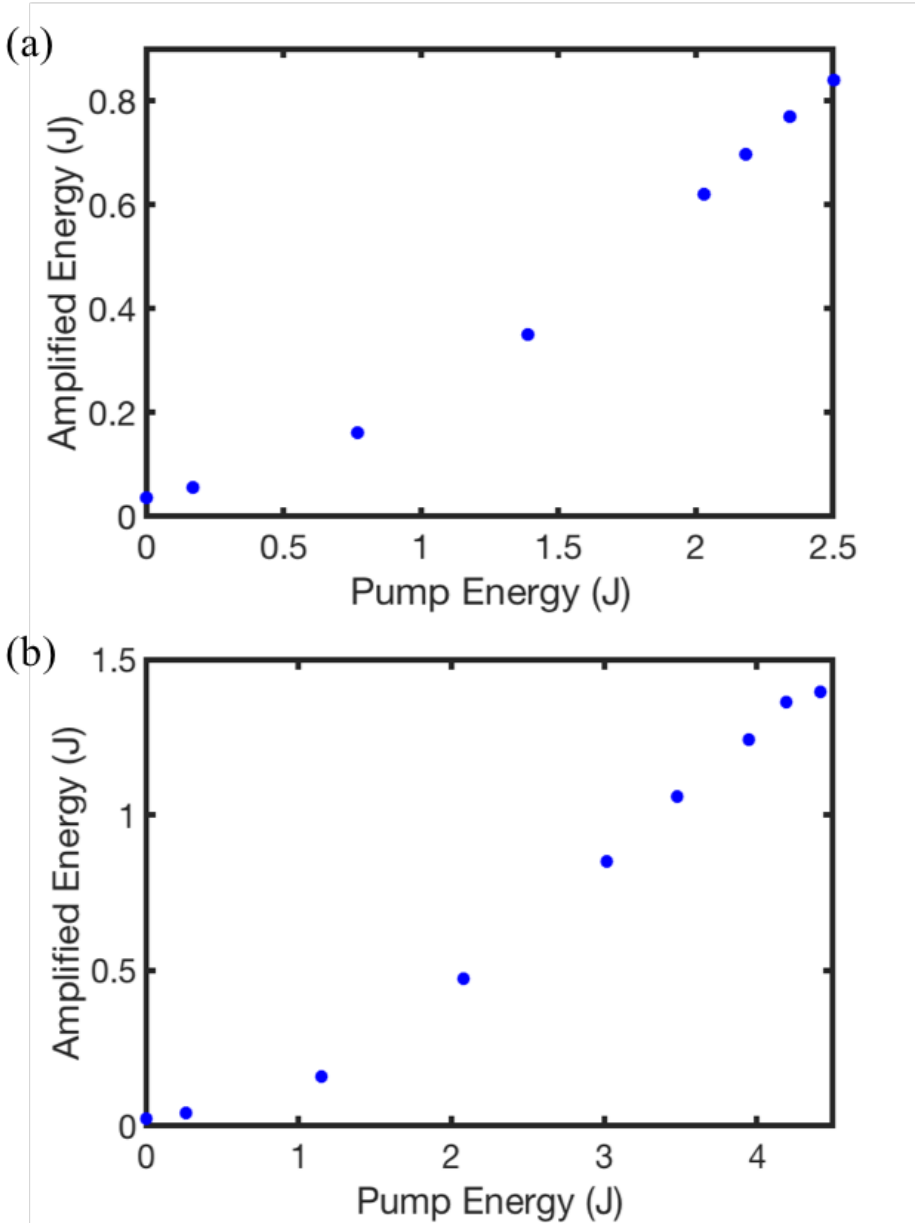

Figure 2.27: a) The output pulse energy from the initial 8-pass cryogenic amplifier as a function of pump energy measured at 1 kHz from the initial 8-pass cryogenic amplifier. The maximum energy achieved from this stage was 900 mJ. b) A measurement of the pulse energy exiting the final amplification stage plotted as a function of total pump energy in both stages. Here, a maximum of ~1.4 J of pulse energy was achieved.

achieved pulse energies of 900 mJ when pumped with 2.66 J of energy. After this amplification stage, the beam is resized to well match the pump spot on the next crystal and control the divergence through the subsequent amplifier by passing through a telescope consisting of a f = 60 cm plano-convex lens and a f = -40 cm plano-concave lens. In this final amplifier, the beam makes two passes of the Yb:YAG slab before exiting. Figure 2.27b shows the extracted pulse energy from this final amplifier as a function of total pump energy in the final two amplifiers. Pulse energies of 1.38 J were achieved when pumping with 4.4 J of energy. In both amplifiers, the pump diodes were pulsed with 300 μs square pulses to a peak power of 5 kW to minimize thermal lensing in the crystals. No attempt was made to characterize the beam quality of the laser when operating at joule level energies. Ensuring good beam quality and stability at 1 kHz operation will be a focus of future work on this laser.

2.8 Demonstration of a Diode-pumped 400 Hz Soft X-ray Laser

This section details the application of the 500 Hz, λ = 1.03 μm, CPA laser described in the above sections to generate lasing at λ = 18.9 nm in Ni-like molybdenum. The CPA laser system was still in development at the time of this demonstration. To improve the CPA laser stability and successfully obtain lasing in the soft x-ray regime, the driving laser was operated at 400 Hz repetition rate. This is a continuation of work performed at Colorado State University to produce tabletop SXRLs with high repetition rates and average powers. [84, 142] In [84], Reagan et al. used a 100 Hz, >1 J, cryogenically-cooled CPA laser akin to the one detailed in this chapter to demonstrate lasing at 18.9 nm in Ni-like molybdenum for periods of 1 hour and 30 minutes at repetition rates of 50 Hz and 100 Hz respectively. This tabletop laser system was notable for its high pulse energies, >1 μJ, and average powers, 0.15 mW, and in fact, a subsequent calibration of the spectrometer diffraction grating showed the pulse energy and power to be higher and closer to ~0.2 mW. [143]

A schematic of the setup for SXRL generation with the 50/100 Hz system is shown in Figure 2.28. Here, a temporally tailored pump pulse consisting of a nanoseconds long pre-pulse

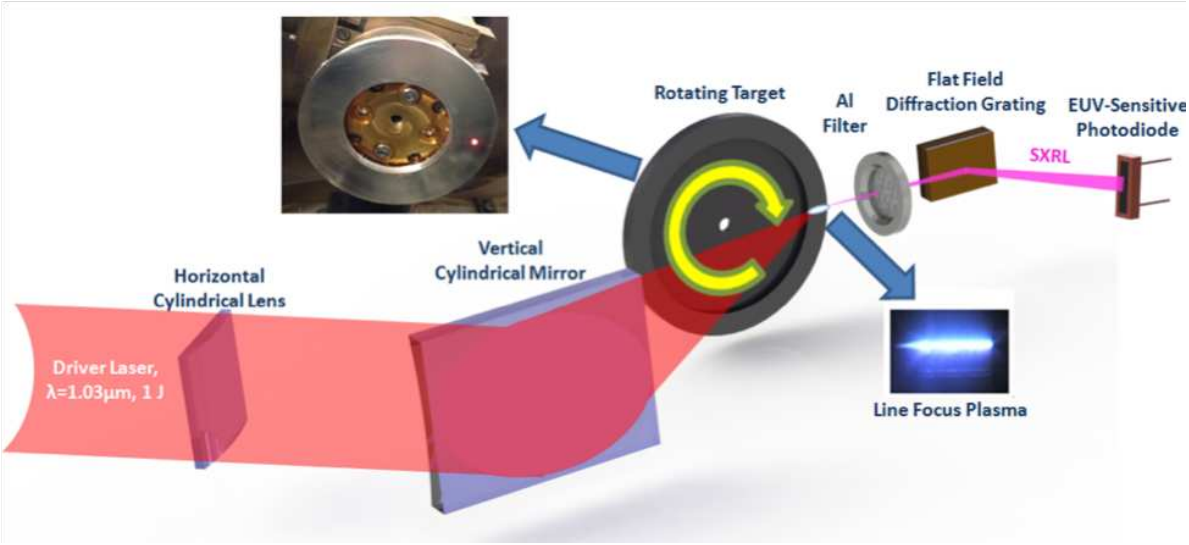

Figure 2.28: Schematic for high repetition rate SXRL operation (from [84])

preceded the short heating pulse is used. This intentionally added pre-pulse had a relative pulse intensity of approximately 10^{-3} as compared to the main pulse and was created as a result of ASE from the regenerative amplifier. The duration and relative intensity of the pre-pulse were controlled by adjusting the timing of the Pockels cell within and after the amplifier as well as the intensity of the stretched short pulses seeded into this amplifier. This tailored pulse had an energy of 0.9 J and the short heating pulse was compressed to ~6 ps after the Treacy compressor. To create and heat the plasma, the driving laser was focused with a horizontal cylindrical lens and vertical cylindrical mirror to form a 30 μm FWHM wide by 6 mm long line focus on the target. The beam was incident at an angle of 29° to efficiently heat the plasma region for optimal SXRL amplification. To enable long duration operation, a high shot capacity target was used as illustrated in the top left of Figure 2.28. On-axis spectra of the generated SXRL radiation was recorded using a grazing incidence variable space diffraction grating and a back-thinned CCD sensitive to x-rays. Aluminum filters were placed between the target and diffraction grating to reject visible and ultraviolet radiation spontaneously emitted from the plasma as well as scattered pump light.

Using the CPA laser developed as part of this dissertation and a setup similar to the one shown in Figure 2.28, lasing was obtained at 400 Hz repetition rate. The only difference between

the setup used for 100 Hz lasing, as shown in Figure 2.28, and the 400 Hz demonstration was that the rotating, high shot capacity target was exchanged for a lower shot capacity slab target. The rational for this decision was to ease the complexity and alignment of the system, and as this was only an initial SXRL demonstration, there was no attempt made to optimize the SXRL pulse energy or to perform long duration operation at this time.

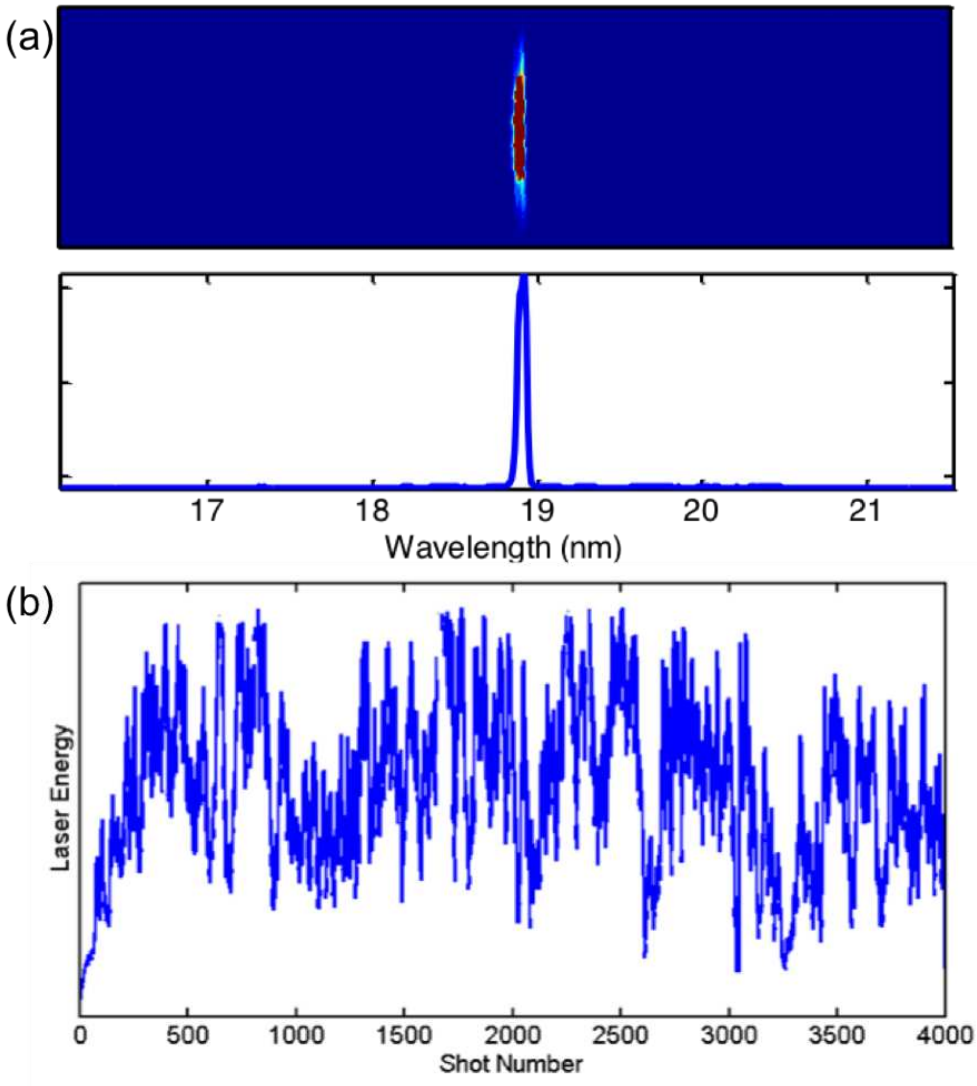

Figure 2.29: a) Single-shot on-axis SXRL spectrum. b) Run of 4000 consecutive shots at λ = 18.9 nm and 400 Hz repetition rate

Figure 2.29a shows a single-shot spectra of the λ = 18.9 nm laser with the λ = 1.03 μm laser running at 400 Hz repetition rate in which strong lasing is observed. Runs of several thousand shots were also acquired, and one is shown in Figure 2.29b. To acquire this data, the CCD camera was replaced with an x-ray sensitive Si-photodiode and placed at the spectral location of the laser wavelength shown in Figure 2.29a. In this figure, we initially see the driver laser thermally stabilizing and coming into focus on the target. This is evidenced by the steady increase in relative pulse energy in the initial shots. The laser then stabilizes and fires on every shot for four thousand consecutive shots. Due to the difficulty of acquiring and storing every photodiode waveform at such a high repetition rate, no attempt was made to record longer runs. The driving laser and SXRL setup were capable of running for much longer durations and in the future a faster data acquisition setup will enable demonstrations for longer periods.

2.9 Summary and Future Work

In summary, we have developed a compact, all diode pumped CPA laser based on cryogenically cooled Yb:YAG. This laser system has demonstrated the capability of stably operating at kW average powers at a repetition rate of 500 Hz. Data was recorded for run times as long as 30 minutes. As a demonstration of the use of this high power source in an application, a 400 Hz, λ = 18.9 nm laser was generated in Ni-like molybdenum, showing strong lasing. Additionally, initial results of the CPA laser operating at 1 kHz repetition rate were presented. 1.4 J pulse energies were obtained at this higher repetition rate, illustrating the viability of this design architecture for obtaining picosecond pulses with average powers >1 kW. These systems will be necessary for creating next generation, high gradient particle accelerators [98], high power OPCPAs for HHG [87] and ultrafast spectroscopy [88], and tabletop SXRLs with high repetition rates and photon flux [84, 142]. Yet, more work is necessary to ensure long term stable operation with high beam quality as well as a transform limit pulse duration below 5 ps, as demonstrated at 500 Hz operation.

In order to reduce the transform limit pulse duration to below 5 ps, it will be necessary to implement a new design for the regenerative amplifier. Two routes that show promise are a thin-disk room temperature Yb:YAG amplifier and a cryogenic Yb:KYW amplifier design. The first option is a well developed technology with commercially available amplifier heads. This design has had great success in generating lasers with high average powers (>1 kW) with picosecond duration transform limited pulses. While these systems have not shown the ability to achieve joule-level pulse energies, the technology appears to be a good choice for a high gain, low pulse energy amplifier. Various technical issues will need to be addressed if this option is pursued. One will be the wavelength matching of this amplification stage with the subsequent cryogenic amplification stages. It is likely that a Fabry-Perot etalon will need to be used as was done in this laser when operating at 500 Hz. The second will be the need for a more elaborate pump design. Due to the low absorption of the thin-disk, it will be necessary to implement a multi-pass pumping scheme which adds considerable complexity as compared to the current design.

A second option for a high energy, broad bandwidth, kHz repetition rate regenerative amplifier could be to use Yb:KYW as the gain material. While this design is not as prevalent as thin-disk Yb:YAG, it has already been employed as a broad bandwidth preamplifier for seeding narrow band cryogenic Yb:YAG [19], and amplifiers based on this technology which deliver the millijoule level pulses at kHz repetition rates are commercially available. Work has been reported on amplifiers with up to 4.7 mJ, sub-ps pulses at 1 kHz repetition rate [38], when operated at room temperature and pumped at $\lambda = 981$ nm. Others have demonstrated performance up to 5.5 mJ with sub-ps transform limit pulses in cryogenically cooled Yb:KYW with $\lambda = 940$ nm pumping [116]. It is possible that the current regenerative amplifier would only need moderate changes to simultaneously achieve the desired pulse energy and bandwidth at high repetition rate operation.

Chapter 3

Development of a Near-Infrared Optical Parametric Chirped Pulse Amplification Laser for Laser Induced Damage Threshold Measurements

3.1 Introduction

The development of "eye safe" lasers, operating at wavelengths between λ = 1.4 μm and 1.8 μm, is of interest for applications requiring the propagation of beams with high pulse energies in open air over long distances. In this wavelength regime, retinal and corneal eye damage is minimized due to radiation absorption effects within the eye. [144] Additionally, interest exists in developing lasers in the near and mid-infrared as a means of extending the cutoff energy of high harmonics [91–93], which scale as $I\lambda^2$, as well as for investigations in ultrafast spectroscopy [88–90]. While development of pulsed lasers in the near-infrared (NIR) continues to advance, no measurements of short pulse optical coating damage have been published. In this chapter, an optical parametric chirped pulse amplification (OPCPA) laser which is tunable from λ = 1.5 μm to 2 μm is constructed and used to perform laser induced damage threshold (LIDT) testing for low OH fused silica as well as various multilayer dielectric optical coatings designed for operation at λ = 1.6 μm.

The work presented in this chapter was done in collaboration with Drew Schiltz and many of the results reported are also presented in his master's thesis. [145] Here, the development and operation of the OPCPA laser system is discussed in detail. Additionally, the experimental results of LIDT are re-examined with discrepancies found with those presented in [145]. Schiltz determined that the measured LIDT of the sample targets deviated from commonly used models for evaluating LIDT, while the analysis performed here suggest good agreement with predicted scaling laws for LIDT suggested by Gamaly et al. [146]. Furthermore, the results

are in agreement with the wavelength dependence observed in ultrafast LIDT at shorter wavelengths [147–149].

3.2 Theory: Optical Parametric Amplification

The work in this chapter centers on the three-wave mixing process called optical parametric amplification (OPA) and by extension difference frequency generation (DFG). In a suitable nonlinear medium, an energetic beam called the pump, of freqency ω_p, and a second low energy beam called the signal, of frequency ω_s, are incident on a nonlinear crystal. The pump beam amplifies the signal beam and, in the process, generates an additional beam called the idler, at frequency ω_i. This process is parametric which means the initial and final quantum states are identical. Energy can be transferred to a virtual state for a period dictated by the uncertainty principle $\hbar/\delta E$ where δE is the energy difference between the virtual level and the closest real level. This fact has the important consequence that no net transfer of energy or momentum can be made from the optical field to the material. Therefore, energy must be conserved in the process

$$\hbar\omega_p = \hbar\omega_s + \hbar\omega_i \tag{3.1}$$

For efficient energy transfer from the pump to both signal and idler wavelengths, momentum should be conserved. This is also referred to as the phase matching condition.

$$\hbar\mathbf{k}_p = \hbar\mathbf{k}_s + \hbar\mathbf{k}_i \tag{3.2}$$

To better understand the nature of OPA, we will derive the coupled amplitude equations which govern the process to see how the nonlinear polarization of the material enables parametric amplification. [1] We begin by first considering the polarization of a material in response to an applied electric field. For the case of nonlinear optics, the induced polarization, $\mathbf{P}(t)$, can be expressed as a power series expansion of the electric field, $\mathbf{E}(t)$.

[1] this derivation closely follows the mathematical treatment presented in [150]

$$\mathbf{P}(t) = \epsilon_0\left(\chi^{(1)}\mathbf{E}(t) + \chi^{(2)}\mathbf{E}^2(t) + \chi^{(3)}\mathbf{E}^3(t) + \cdots\right) \tag{3.3}$$

The quantities $\chi^{(n)}$, where n = 1,2,3..., are known as the susceptibility tensors. In equation (3.3), $\chi^{(1)}$ is the linear susceptibility while all higher terms are known as the nonlinear susceptibility. Specifically, $\chi^{(2)}$ is called the second-order non-linear susceptibility, $\chi^{(3)}$ is called the third-order nonlinear susceptibility and so on. We can further express the induced polarization in equation (3.3) as

$$\begin{aligned}\mathbf{P}(t) &= \mathbf{P}^{(1)}(t) + \mathbf{P}^{(2)}(t) + \mathbf{P}^{(3)}(t) + \cdots \\ &= \mathbf{P}^{(1)}(t) + \mathbf{P}^{(NL)}(t)\end{aligned} \tag{3.4}$$

In OPA, we are interested in the second-order nonlinear polarization, $\mathbf{P}^{(2)}(t) = \epsilon_0\chi^{(2)}\mathbf{E}^2(t)$, for the case in which two waves, at frequencies ω_1 and ω_2, interact in a loseless nonlinear medium. The complex electric field can be expressed as

$$\mathbf{E}(t) = E_1 e^{-i\omega_1 t} + E_2 e^{-i\omega_2 t} + c.c. \tag{3.5}$$

This yields the following expression for the second-order nonlinear polarization

$$\begin{aligned}\mathbf{P}^{(2)}(t) &= \sum_n P(\omega_n) e^{-i\omega_n t} \\ P(2\omega_1) &= \epsilon_0\chi^{(2)}E_1^2 \\ P(2\omega_2) &= \epsilon_0\chi^{(2)}E_2^2 \\ P(\omega_1+\omega_2) &= 2\epsilon_0\chi^{(2)}E_1E_2 \\ P(\omega_1-\omega_2) &= 2\epsilon_0\chi^{(2)}E_1E_2^* \\ P(0) &= 2\epsilon_0\chi^{(2)}(E_1E_1^* + E_2E_2^*)\end{aligned} \tag{3.6}$$

Each term in the above expression refers to a different nonlinear effect and have corresponding complex conjugates. $P(2\omega_1)$ and $P(2\omega_2)$ correspond to second harmonic generation

(SHG), $P(\omega_1+\omega_2)$ is sum frequency generation (SFG), $P(\omega_1-\omega_2)$ is difference frequency generation (DFG) and OPA, and $P(0)$ is a static electric field across the medium known as optical rectification. For the case of OPA, ω_1 and ω_2 can be replaced by the pump frequency, ω_p, and signal frequency, ω_s, respectively, to give the following second-order nonlinear polarization term for OPA.

$$P(\omega_p-\omega_s)=2\epsilon_0\chi^{(2)}E_pE_s^* \tag{3.7}$$

Now, we consider the form of an electromagnetic wave propagating through a dispersionless, lossless nonlinear medium, which can be described by Maxwell's equations. We will be concerned with nonmagnetic materials in which there are no free charges, i.e. $\rho=0$, and no free currents, i.e. $\mathbf{J}=0$. This allows the following relations,

$$\mathbf{B}=\mu_0\mathbf{H} \tag{3.8}$$

$$\mathbf{D}=\epsilon_0\mathbf{E}+\mathbf{P} \tag{3.9}$$

Here, $\mathbf{P}$ has the form given in equation (3.4), and Maxwell's equations then take the following form

$$\nabla\cdot\mathbf{D}=0 \tag{3.10}$$

$$\nabla\cdot\mathbf{B}=0 \tag{3.11}$$

$$\nabla\times\mathbf{E}=-\frac{\partial\mathbf{B}}{\partial t} \tag{3.12}$$

$$\nabla\times\mathbf{H}=\frac{\partial\mathbf{D}}{\partial t} \tag{3.13}$$

By applying the curl operator to equation (3.12), using the relations given in equations (3.8) and (3.13), and allowing the interchange of the time derivative with the curl operator, we obtain the following relation

$$\nabla(\nabla\cdot\mathbf{E})-\nabla^2\mathbf{E}=-\mu_0\frac{\partial^2\mathbf{D}}{\partial t^2} \tag{3.14}$$

By use of equation (3.9), equation (3.14) takes the form

$$\nabla(\nabla\cdot\mathbf{E})-\nabla^2\mathbf{E}+\mu_0\epsilon_0\frac{\partial^2\mathbf{E}}{\partial t^2}=-\mu_0\frac{\partial^2\mathbf{P}}{\partial t^2} \tag{3.15}$$

In linear optics with isotropic source free media, equation (3.10) implies $\nabla\cdot\mathbf{E}=0$, yet in nonlinear optics, this is not necessarily the case due to the more general relation between the electric displacement field and electric field shown in equation (3.9). If we assume that the solution to the wave equation takes the form of a transverse, infinite plane wave (which to a good approximation is true), then $\nabla\cdot\mathbf{E}=0$, and the first term of equation (3.15) can be eliminated. Equation (3.15) can also be further simplified by noting that $\frac{1}{\mu_0\epsilon_0}=c^2$ to yield the following

$$\nabla^2\mathbf{E}-\frac{1}{c^2}\frac{\partial^2\mathbf{E}}{\partial t^2}=\mu_0\frac{\partial^2\mathbf{P}}{\partial t^2} \tag{3.16}$$

The polarization can be decomposed into its linear and nonlinear terms as in equation (3.4), and noting that for an isotropic medium, $\mathbf{P}^{(1)}=\varepsilon_0\chi^{(1)}\mathbf{E}$, we have

$$\begin{aligned}
\nabla^2\mathbf{E}-\frac{1}{c^2}\frac{\partial^2\mathbf{E}}{\partial t^2}&=\mu_0\frac{\partial^2}{\partial t^2}\left(\mathbf{P}^{(1)}+\mathbf{P}^{(NL)}\right)\\
\nabla^2\mathbf{E}-\frac{1}{c^2}\left(1+\chi^{(1)}\right)\frac{\partial^2\mathbf{E}}{\partial t^2}&=\mu_0\frac{\partial^2\mathbf{P}^{(NL)}}{\partial t^2}\\
\nabla^2\mathbf{E}-\frac{\epsilon^{(1)}}{c^2}\frac{\partial^2\mathbf{E}}{\partial t^2}&=\mu_0\frac{\partial^2\mathbf{P}^{(NL)}}{\partial t^2}
\end{aligned} \tag{3.17}$$

where $\epsilon^{(1)}=1+\chi^{(1)}$. From equation (3.17), we have an inhomogeneous wave equation with the induced nonlinear polarization as the source term. When considering a dispersive medium, we must analyze each frequency component individually. The electric and polarization fields are then a summation of the various spectral components. The fields for each frequency component are expressed as

$$\begin{aligned}\mathbf{E}_n(\mathbf{r},t) &= \mathbf{E}_n(\mathbf{r})e^{-i\omega_n t} + c.c. \\ \mathbf{P}_n^{(NL)}(\mathbf{r},t) &= \mathbf{P}_n^{(NL)}(\mathbf{r})e^{-i\omega_n t} + c.c.\end{aligned} \tag{3.18}$$

and equation (3.17) can be written as follows for each frequency component, with the evaluation of the second time derivatives yielding a factor of $-\omega_n^2$

$$\nabla^2\mathbf{E}_n(\mathbf{r},t) + \frac{\omega_n^2\epsilon^{(1)}(\omega_n)}{c^2}\mathbf{E}_n(\mathbf{r},t) = -\mu_0\omega_n^2\mathbf{P}_n^{(NL)}(\mathbf{r},t) \tag{3.19}$$

We will now apply the above nonlinear wave equation to the case of OPA/DFG. If we consider the spectral component at the idler frequency, $\omega_i = \omega_p - \omega_s$, and assume a monochromatic, plane wave propagating in the +z direction, then the field can be expressed as

$$E_i(z,t) = A_i(z)e^{i(k_i z - \omega_i t)} + c.c. \tag{3.20}$$

where $k_i = \frac{n_i\omega_i}{c}$ and $n_i^2 = \epsilon^{(1)}(\omega_i)$. The nonlinear source term in equation (3.19) has the form given in equation (3.18)

$$P_i^{(2)}(z,t) = P_i^{(2)}(z)e^{-i\omega_i t} + c.c. \tag{3.21}$$

From equation (3.7), we know that for incident waves of frequency ω_p and ω_s, the term for OPA/DFG has the form $P_i^{(2)}(z) = 2\epsilon_0\chi^{(2)}E_pE_s^*$, and the applied fields have the following form

$$E_n(z,t) = A_n(z)e^{i(k_n z - \omega_n t)} + c.c. \tag{3.22}$$

where $n = p, s$, then equation (3.21) has the form

$$P_i^{(2)}(z,t) = 2\epsilon_0\chi^{(2)}A_p(z)A_s^*(z)e^{i(k_p - k_s)z}e^{-i\omega_i t} + c.c. \tag{3.23}$$

By inserting equations (3.20), (3.22), and (3.23) into (3.19) and noting that $k_i^2 = \frac{\epsilon^{(1)}\omega_i^2}{c^2}$ we obtain the following equation

$$\left(\frac{\partial^2 A_i}{\partial z^2} + 2ik_i\frac{\partial A_i}{\partial z}\right)e^{ik_i z} = \frac{-2\omega_i^2\chi^{(2)}}{c^2}A_p A_s^* e^{i(k_p-k_s)z} \tag{3.24}$$

where the amplitudes' spatial dependence and complex conjugates have been suppressed. This equation can be further simplified by assuming the slow varying amplitude approximation, which implies that the wave's amplitude varies much more slowly than its wavelength.

$$\left|\frac{\partial^2 A_I}{\partial z^2}\right| \ll \left|k_i\frac{\partial A_i}{\partial z}\right| \tag{3.25}$$

which reduces equation (3.24) to

$$\frac{\partial A_i}{\partial z} = \frac{2id_{eff}\omega_i^2}{k_i c^2}A_p A_s^* e^{i\Delta kz} \tag{3.26}$$

where the term $\Delta k = k_p - k_s - k_i$ is the wavevector mismatch, and $2d_{eff} = \chi^{(2)}$ relates the second-order susceptibly to the nonlinear optical coefficient. [150] By a similar method, the coupled amplitude equations for the pump and signal beams can be derived to obtain

$$\frac{\partial A_s}{\partial z} = \frac{2id_{eff}\omega_s^2}{k_s c^2}A_p A_i^* e^{i\Delta kz} \tag{3.27}$$

$$\frac{\partial A_p}{\partial z} = \frac{2id_{eff}\omega_p^2}{k_p c^2}A_i A_s e^{-i\Delta kz} \tag{3.28}$$

These coupled amplitude equations illustrate how the variation in amplitude of one wave depends on the other two waves in the process. These equations can be solved analytically if we assume that the pump wave is sufficiently strong such that its amplitude remains constant for the interaction length. Thus, we may let $\frac{\partial A_p}{\partial z} = 0$. The resulting derivatives of equations (3.26) and (3.27) are then

$$\frac{\partial^2 A_i}{\partial z^2} = \alpha_i A_p\left[\frac{\partial A_s^*}{\partial z}e^{i\Delta kz} + i\Delta k A_s^* e^{i\Delta kz}\right] \tag{3.29}$$

$$\frac{\partial^2 A_s}{\partial z^2} = \alpha_s A_p\left[\frac{\partial A_i^*}{\partial z}e^{i\Delta kz} + i\Delta k A_i^* e^{i\Delta kz}\right] \tag{3.30}$$

$$\alpha_n = \frac{i d_{eff} \omega_n^2}{k_n c^2}, n = i, s$$

By substitution of equations (3.26), (3.27), and their associated complex conjugates into equations (3.29) and (3.30), we obtain the following homogeneous linear second order differential equations.

$$\frac{\partial^2 A_i}{\partial z^2} - i\Delta k \frac{\partial A_i}{\partial z} - \gamma^2 A_i = 0 \tag{3.31}$$

$$\frac{\partial^2 A_s}{\partial z^2} - i\Delta k \frac{\partial A_s}{\partial z} - \gamma^2 A_i = 0 \tag{3.32}$$

$$\gamma^2 = \frac{d_{eff}^2 \omega_i^2 \omega_s^2}{k_i k_s c^4} \left| A_p \right|^2$$

With the boundary conditions that $A_i(0)$ and $A_s(0)$ must be distinct constants, we obtain the following solution for the signal and idler beams.

$$A_i = e^{\frac{i\Delta k z}{2}} \left[A_i(0) \cosh(gz) + \left(\frac{\alpha_i A_p A_s^*(0)}{g} - \frac{i\Delta k A_i(0)}{2g} \right) \sinh(gz) \right] \tag{3.33}$$

$$A_s = e^{\frac{i\Delta k z}{2}} \left[A_s(0) \cosh(gz) + \left(\frac{\alpha_s A_p A_i^*(0)}{g} - \frac{i\Delta k A_s(0)}{2g} \right) \sinh(gz) \right] \tag{3.34}$$

$$g^2 = \gamma^2 - \left(\frac{\Delta k}{2} \right)^2$$

From these solutions, we notice that both signal and idler increase monotonically with crystal length, and the amplitudes are maximized when $\Delta k = 0$, i.e. perfect phase matching. It should be noted that these solutions were found for signal, idler, and pump beams all propagating collinearly. In general, this does not have to be the case and the beams can propagate non-collinearly. Next, we will focus on techniques to minimize phase mismatch for non-collinear beam propagation, thus improving energy transfer efficiency.

Minimizing phase mismatch for co-propagating beams with differing frequencies is necessary for efficient energy transfer in nonlinear processes. The issue stems from the fact that in materials with dispersion, the index of refraction generally increases with increasing frequency. This results in temporal walk off of the beams due to their velocity difference within

the medium. Various techniques can be used to minimize phase mismatch during nonlinear processes, including angle tuning, temperature tuning, and quasi-phase-matching. Here, we will be concerned with the optimization of the phase matching angle of the crystal as well as the non-collinear angle, which we will define as the angle between the incident pump and signal beams. The theory for achieving optimal phase matching via this method is based on the work of [151].

In general, phase matching can be achieved in birefringent crystals by precisely controlling the orientation of the crystal and the polarization of the incoming beams. In this way, the various interacting beams will experience different indices of refraction and propagate such that the phase mismatch is minimized. As a reminder, the phase matching condition for the three coupled waves in OPA/DFG is given by

$$\Delta\vec{k} = \vec{k}_p - \vec{k}_s - \vec{k}_i \tag{3.35}$$

For non-collinear phase matching, these vectors may propagate along different directions so long as the condition in equation (3.35) is satisfied. Figure 3.1 illustrates the geometry of

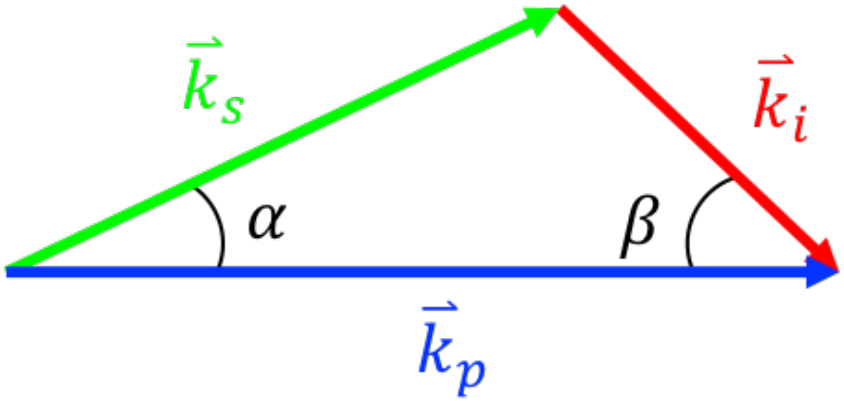

Figure 3.1: Geometry for non-collinear phase matching

non-collinear OPA/DFG where the signal beam, $\vec{k}_s$, propagates at an angle α with respect to the pump beam, $\vec{k}_p$, while the generated idler beam, $\vec{k}_i$, makes the angle β with respect to $\vec{k}_p$ to

satisfy the condition given in equation (3.35). This shows that the projections of $\vec{k}_i$ and $\vec{k}_s$ along p must equal $\vec{k}_p$. With the condition that $\omega_p > \omega_s \geq \omega_i$, the following general phase matching condition can be obtained

$$\frac{n_p(\lambda_p)}{\lambda_p} = \frac{n_s(\lambda_s)}{\lambda_s}\cos\alpha + \frac{n_i(\lambda_i)}{\lambda_i}\cos\beta \tag{3.36}$$

$$\beta = \sin^{-1}\left[\frac{n_s(\lambda_s)\lambda_i}{n_i(\lambda_i)\lambda_s}\sin\alpha\right] \tag{3.37}$$

As was mentioned before, phase matching can be performed in birefringent crystals which come in two types, uniaxial and biaxial. Uniaxial crystals have two principal refractive indices referred to as ordinary, n_o, and extraordinary, n_e. Crystals are considered negative uniaxial if $n_e < n_o$ and positive if $n_e > n_o$. Light polarized normal to the plane of beam propagation and the optical axis of the crystal, or c-axis, experiences a fixed, ordinary refractive index, n_o. Light polarized in the plane of beam propagation and the c-axis experiences an extraordinary refractive index, $n_e(\theta)$. This index depends upon the angle between the c-axis and the direction of beam propagation and can be described by the following equation

$$\frac{1}{n_e^2(\theta)} = \frac{\cos^2\theta}{n_o^2} + \frac{\sin^2\theta}{n_e^2} \tag{3.38}$$

For the case of biaxial crystals, there exist three principal refractive indices, $n_x < n_y < n_z$, corresponding to the crystallographic axes X, Y, and Z. In the reference frame shown in Figure 3.2, the propagation of a wave in a biaxial crystal is described by the following refractive index relation

$$\frac{\sin^2\theta\cos^2\phi}{(n^{-2} - n_x^{-2})} + \frac{\sin^2\theta\sin^2\phi}{(n^{-2} - n_y^{-2})} + \frac{\cos^2\theta}{(n^{-2} - n_z^{-2})} = 0 \tag{3.39}$$

Figure 3.2 schematically shows the relation between the axes X, Y, and Z and angles θ and ϕ. The angle θ is defined as the angle between the optical path and the Z axis, while ϕ defines the angle of the X axis in the X-Y plane from the phase matching plane.

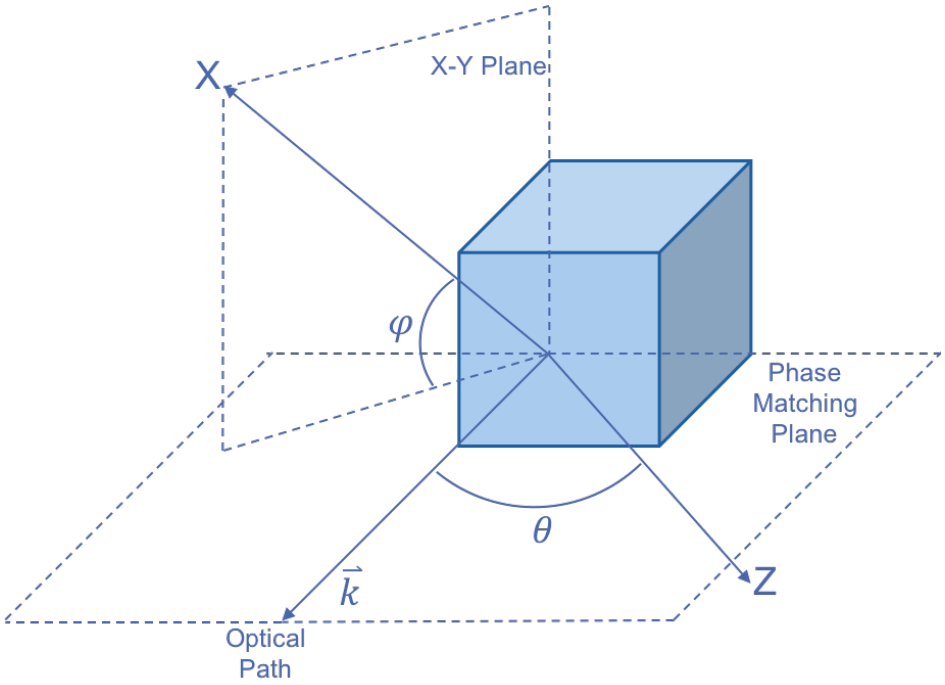

Figure 3.2: A schematic showing the relation between the axes of the optical reference frame and angles θ and ϕ

There are two types of three-wave interactions to achieve phase matching in birefringent crystals. In type I phase matching, the two lower frequency beams have the same polarization which is orthogonal to that of the highest frequency beam. For type II, the two lower frequency beams are orthogonally polarized with one of the lower frequency beams polarized in the same direction as the highest frequency beam.

Of particular interest for the laser system described in this chapter is type I DFG in beta barium borate (BBO) and type II OPA in potassium titanyl phosphate (KTP). Liu et al. derived the phase matching angle, θ_{PM}, for non-collinear beam propagation in uniaxial and biaxial crystals. [151] The following convention is used to simplify equations

$$n_j(\lambda_k) \equiv \frac{n_j(\lambda_k)}{\lambda_k} \tag{3.40}$$

where $k = i, s, p$ for idler, signal, and pump, respectively, $j = o, e$ for uniaxial crystals and $j = x, y, z$ for biaxial crystals.

For type I DFG in BBO, we are concerned with phase matching in a negative uniaxial crystal which from [151] gives the following relations.

$$n_e(\lambda_p) = n_o(\lambda_s) + n_o(\lambda_i) \tag{3.41}$$

$$\beta = \sin^{-1}\left[\frac{n_o(\lambda_s)}{n_o(\lambda_i)}\sin\alpha\right] \tag{3.42}$$

$$\sin\theta_{PM} = \frac{n_e(\lambda_p)}{n_o(\lambda_s)\cos\alpha + n_o(\lambda_i)\cos\beta}\sqrt{\frac{n_o^2(\lambda_p) - (n_o(\lambda_s)\cos\alpha + n_o(\lambda_i)\cos\beta)^2}{n_o^2(\lambda_p) - n_e^2(\lambda_p)}} \tag{3.43}$$

For efficient amplification of NIR pulses across wavelengths ranging from $\lambda = 1.5 - 2\mu$m type II OPA is employed in KTP following the work of [152]. To determine the appropriate phase matching and non-collinear angles, the following equations from [151] were used

$$n_y(\lambda_p) = n_z(\lambda_s)\cos\alpha + n_y(\lambda_i)\cos\beta \tag{3.44}$$

$$\beta = \sin^{-1}\left[\frac{n_y(\lambda_p)}{n_y(\lambda_i)}\sin\alpha\right] - \alpha \tag{3.45}$$

$$\sin\theta_{PM} = \frac{n_z(\lambda_s)}{n_y(\lambda_p)\cos\alpha + n_y(\lambda_i)\cos(\alpha+\beta)}\sqrt{\frac{n_x^2(\lambda_s) - (n_y(\lambda_p)\cos\alpha - n_y(\lambda_i)\cos(\alpha+\beta))^2}{n_x^2(\lambda_s) - n_z^2(\lambda_s)}} \tag{3.46}$$

Figure 3.3a shows the resulting phase matching angle for signal wavelengths ranging from $\lambda = 600 - 900$nm when pumped at $\lambda = 515$nm for various pump-signal non-collinear angles in type I BBO. We see that good phase matching is achieved across a large number of wavelengths for $\theta_{PM} \approx 24°$ a non-collinear angle $\alpha \approx 2°$. These parameters are important for efficiently generating tunable idler pulses in the NIR. Figure 3.3b shows the resulting phase matching angle for type II OPA in KTP for signal wavelengths ranging from $\lambda = 1.2 - 2\mu$m when pumped at $\lambda = 1.03\mu$m for non-collinear angles of $1 - 5°$. We see that by adjustment of both the phase matching and non-collinear angles good phase matching can be achieved for the wavelengths of interest.

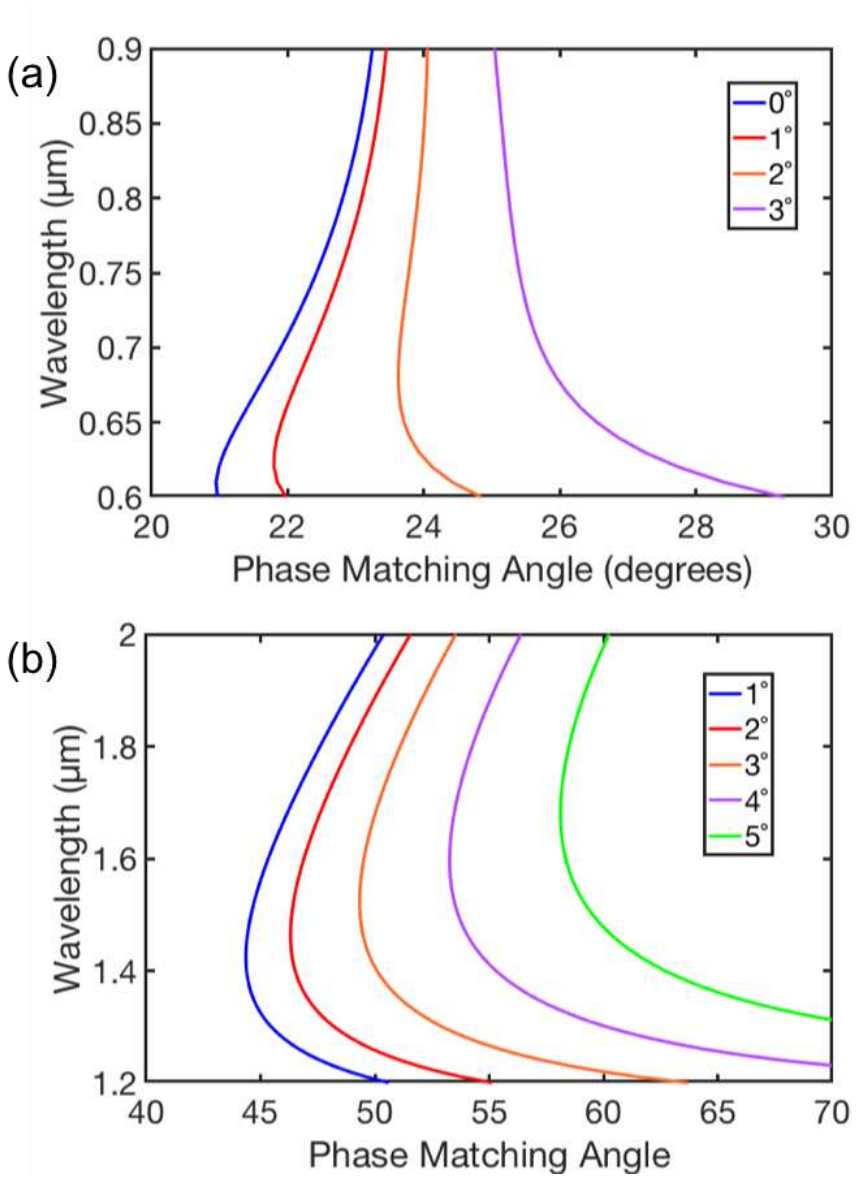

Figure 3.3: a) A plot of the wavelength and phase matching angle for non-collinear type I OPA in BBO with 515 nm pumping. The plot is made for various non-collinear angles ranging from 0-3 degrees between pump and signal. b) A plot of the wavelength and phase matching angle for non-collinear type II OPA in the X-Z plane of KTP for various non-collinear angles.

3.3 NIR OPCPA System Design and Construction Overview

Figure 3.4 shows a block diagram of the OPCPA laser system constructed as part of this work. Short pulses are generated in the mode-locked Yb:KYW oscillator described in Section 2.2, are separated into two pulses via a beam splitter, and used to seed two separate amplification chains. The first amplifier chain is a tunable NIR OPCPA laser which is described in detail in this chapter. The other is a $\lambda = 1\mu$m, 100 Hz CPA laser described in [34] which serves as the pump source for the final stages of the OPCPA. This common seed source provides passive temporal synchronization of the pump and seed pulses in the OPCPA.

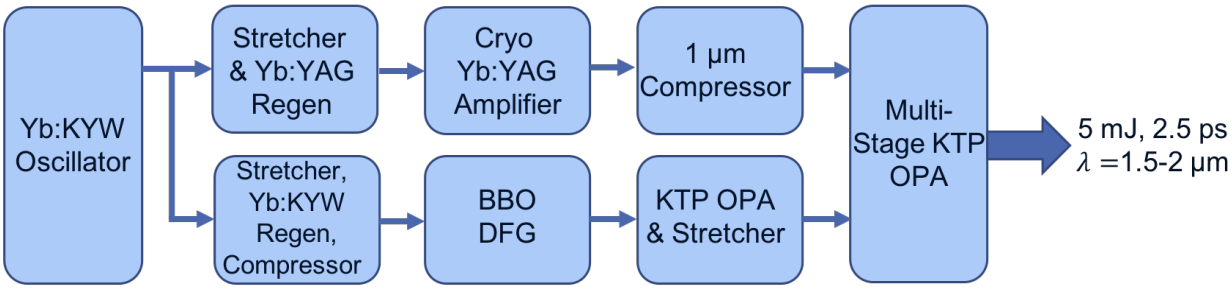

Figure 3.4: A block diagram of the amplification stages for generating a NIR, millijoule level OPCPA at 100 Hz repetition rate.

The $\lambda = 1\mu$m laser system is composed of a room temperature Yb:YAG regenerative amplifier followed by a cryogenic Yb:YAG amplifier capable of producing up to 140 mJ of uncompressed pulse energy at 100 Hz repetition rate. These pulses are then compressed to ~5 ps in a dielectric grating compressor, as described in Section 2.6, and used as the pump source for the final stages of OPA.

The OPCPA laser is comprised of a Yb:KYW regenerative amplifier, a DFG and pre-OPA front end, and multiple stages of OPA which are pumped by the $\lambda = 1\mu$m laser. The regenerative amplifier produces ~100 μJ, sub picosecond pulses which are then used in a type I DFG in BBO to produce an idler pulse whose wavelength is tunable from $\lambda = 1.5 - 2\mu$m. A type II optical parametric preamplifier is seeded with these NIR pulses and increases their energy to the mi-

crojoule level. The NIR pulses are then temporally stretched and are amplified in three stages of type II OPA in KTP.

3.4 Yb:KYW Regenerative Amplifier

Prior to amplification, pulses from the oscillator are temporally stretched in a Martinez style stretcher similar to the one detailed in Section 2.3.1. Here, a 1200 mm^{-1} grating and a f = 12" spherical concave mirror are used. The grating and spherical mirror are separated by ~180 mm and a flat mirror was placed at the focal plane of the mirror to fold the system. The stretcher has an effective path length of -0.5 m which corresponds to a temporal pulse duration of 15 ps for 3.3 nm of bandwidth. Due to the low pulse energies from the regenerative amplifier, this stretch factor was sufficient for amplification and avoid non-linear effects, that were not observed.

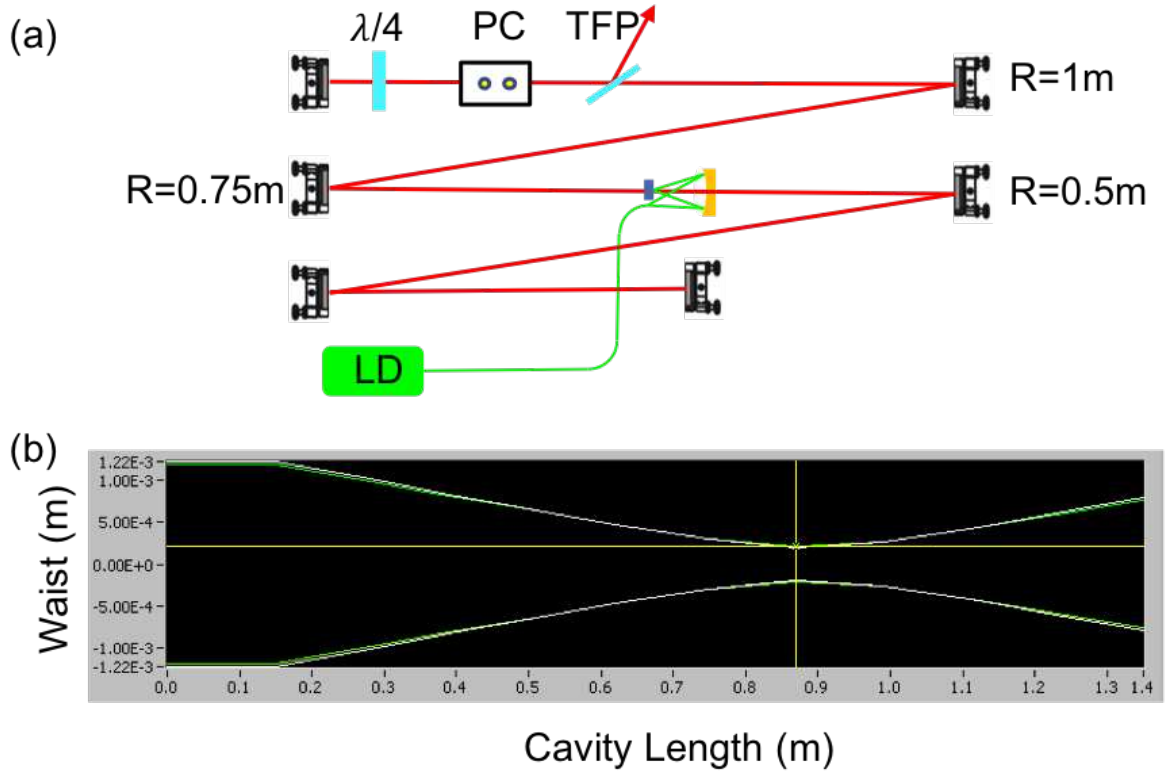

Figure 3.5: a) A schematic of the Yb:KYW regenerative amplifier. b) shows the mode size throughout the cavity with the yellow cursors indicating the position of the crystal where there is good spatial overlap of the cavity mode and the 200 µm pump spot.

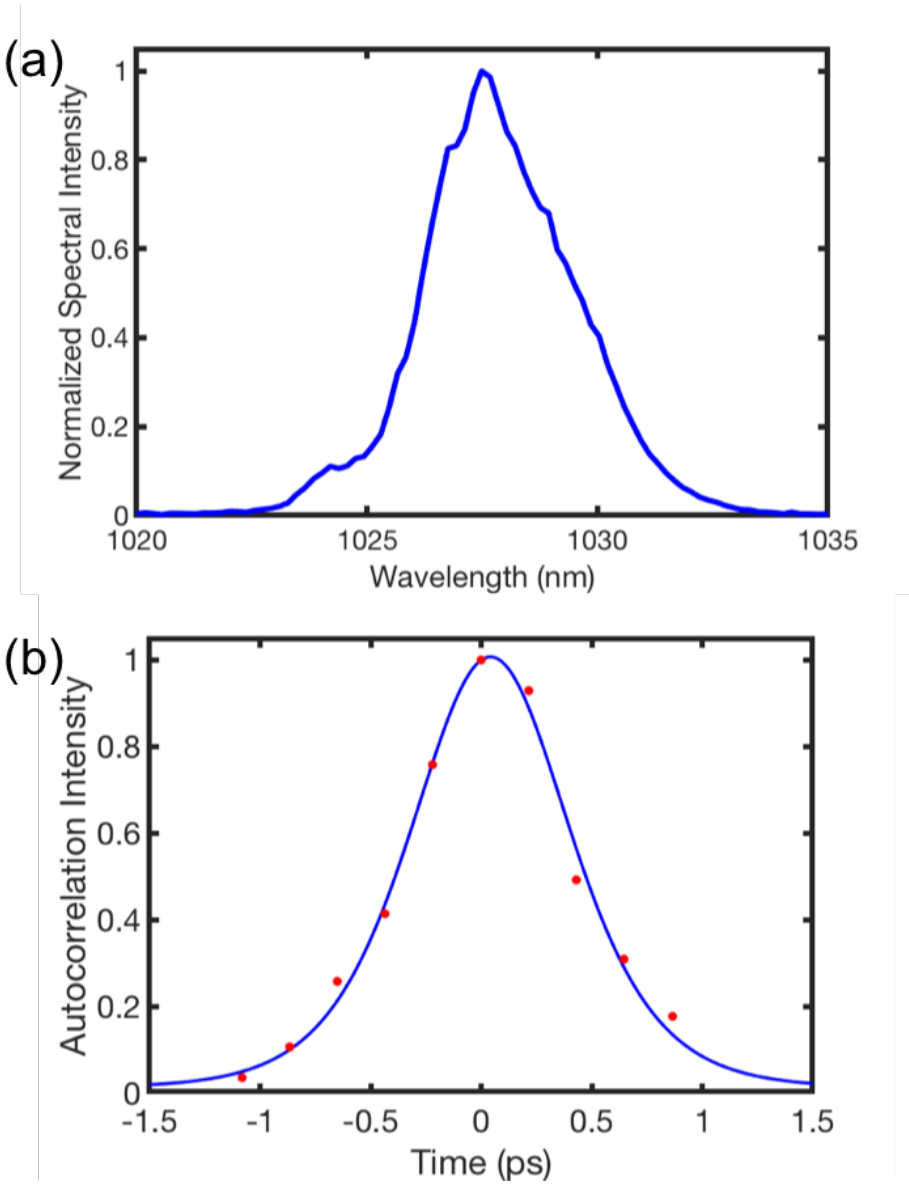

Figure 3.6: a) Yb:KYW regenerative amplifier spectrum showing a FWHM bandwidth of 3.3 nm. b) An intensity SHG autocorrelation of the compressed Yb:KYW regenerative amplifier. The sech^2 fit to the acquired data shows the pulses have a FWHM pulse duration of 850 fs.

The cavity design for the amplifier, shown in Figure 3.5a, is similar to the one used in the Yb:KYW oscillator. All curved mirrors are identical, producing the same mode size throughout the cavity but the chirped mirror, output coupler, and semiconductor absorber mirror (SESAM) were all replaced by flat high reflecting dielectric mirrors. The mode size throughout the cavity is shown in Figure 3.5b with the yellow cursors indicating the position of the crystal in the cavity.

A 5x5x3 mm Yb:KYW crystal was used as the gain medium. This was pumped by a 30 W, λ=981 nm, 200 μm core, fiber coupled laser diode. The fiber tip was 1-to-1 imaged onto the crystal using an f = 2" spherical mirror, for good mode matching between the pump and cavity mode. The spherical mirror had a small hole in the middle which allowed the cavity beam to pass through it. Necessarily, a quarter waveplate, Pockels cell and thin film polarizer (TFP) were included in the cavity to electro-optically seed and eject pulses from the cavity.

During typical operation, seed pulses make ~25 cavity round trips before exiting the amplifier with pulse energies of ~200 µJ when pumped with 7 W peak pump power at a repetition rate of 100 Hz. The typical spectrum from the amplifier, shown in Figure 3.6a, has a bandwidth of 3.3 nm FWHM, corresponding to a transform limit pulse duration of 335 fs. Pulse compression is performed with a Treacy style compressor [104]. It is composed of two parallel 1200 mm^{-1} separated by 25 cm and the pulses are diffracted twice from each grating. The overall compressor efficiency is 46 % yielding ~100 µJ pulses. Figure 3.6b shows a SHG intensity autocorrelation of the compressed pulses after amplification and here the FWHM duration is 850 fs but pulse durations of 600 fs were achieved. These pulses were short enough to induce non-linear effects required in the OPCPA front end.

3.5 NIR OPCPA

The front end of the NIR OPCPA is shown schematically in Figure 3.7. It consists of two parts. An initial DFG stage and an OPA preamplifier. While DFG and OPA are analogous properties, as detailed in Section 3.2, the names are fitting because the primary purpose of each stage is evidenced by the name. In the DFG stage, the purpose is the generation of the tunable idler pulse by selectively amplifying a portion of a broadband signal beam. The idler from the initial stage then becomes the signal for the OPA preamplifier, boosting its energy before temporal stretching. It should be noted that an idler pulse is also generated in the mid-IR during this and subsequent OPA stages, but these wavelengths are not of interest in our application. Therefore, we disregard them.

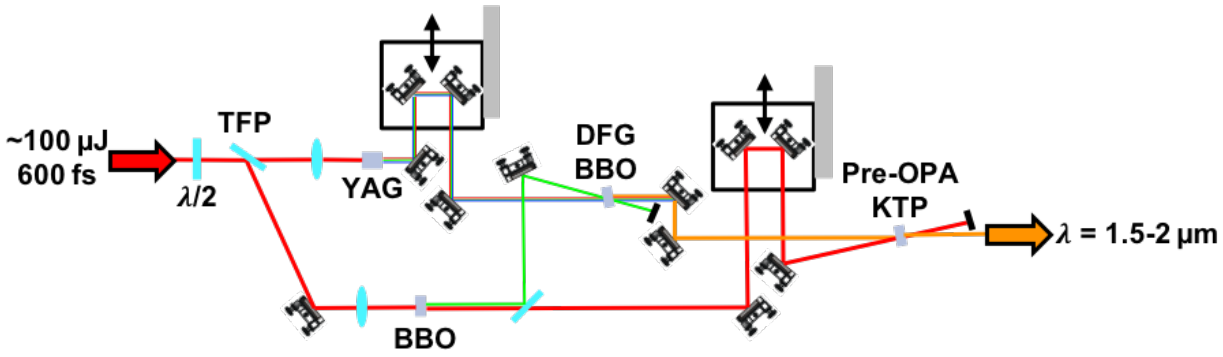

Figure 3.7: A schematic showing the beam path for the generation and pre-amplification of the λ = 1.5-2 µm pulses.

3.5.1 Theory: Super Continuum Generation

Before discussing the design and operation of the OPCPA front end, it is necessary to discuss another nonlinear process, besides DFG/OPA, employed for the generation of the desired idler wavelength. Because the goal of the DFG is to create wavelengths from λ=1.5 to 2 µm, it is necessary to have a signal beam with continuous broad bandwidth at shorter wavelengths. If the frequency doubled output of the Yb:KYW regenerative amplifier is to be used as a pump source for DFG, then it would be necessary to have a signal beam with a bandwidth which continuously spans λ = 700 – 800 nm. By using the appropriate phase matching condition, the desired idler wavelengths can be obtained.

One means of producing a signal beam with the desired spectral characteristics is through super continuum generation (SCG). This process is a complex interplay of both linear and nonlinear spatiotemporal effects, such as diffraction, group velocity dispersion, self-focusing, self-steepening, multi-photon absorption, etc. Therefore, a comprehensive description will not be attempted here. More detailed analysis of SCG in bulk materials can be found in [153,154]. SCG is actually quite a simple effect to elicit and can be done by loosely focusing a sub-picosecond pulse into an appropriate material. With enough intensity, the pulse begins to self-focus. This process can be understood by first considering the intensity dependent refractive index.

$$n = n_0 + n_2 I \tag{3.47}$$

where n_0 is the weak-field or linear refractive index, n_2 is the second-order or nonlinear refractive index, and I is the field intensity. This relation is also known as the Kerr effect and demonstrates the intensity dependence of the refractive index. If we consider a cylindrically symmetric Gaussian beam with enough intensity, the highest index will be along the optical axis for positive n_2 and decrease radially, effectively creating a lens and causing the beam to focus in the material. The self-focusing threshold for a beam with this spatial profile is [155]

$$P_{cr} = \frac{1.8962\lambda^2}{4\pi n_0 n_2} \tag{3.48}$$

where λ is the laser wavelength. This is called the critical power for self-focusing and is the point at which the effects of self-focusing and diffraction exactly cancel. Above this threshold value, the beam will focus in the material, and a change in the phase of the pulse is also associated with the nonlinear refractive index.

$$\phi_{NL} = -\frac{n_2\omega_0}{c} I(t) z \tag{3.49}$$

where ω_0 is the carrier frequency and z is the propagation length. The result of this time varying phase is a broadening of the pulse spectrum called self-phase modulation (SPM) and is described by the following equations

$$\delta\omega(t) = \frac{\partial\phi_{NL}(t)}{\partial t} \tag{3.50}$$

$$\omega(t) = \omega_0 + \delta\omega(t) \tag{3.51}$$

Under the assumption that n_2 is positive, a temporally Gaussian pulse will see that its leading edge will be red shifted, while the trailing edge will be blue shifted. In materials with normal group velocity dispersion (GVD), i.e. $k_0'' > 0$ where $k_0'' = \partial^2 k/\partial\omega^2|_{\omega_0}$ and $k = \omega_0 n_0/c$, pulse splitting at the nonlinear focus produces two sub-pulses. The leading pulse being red shifted with respect to the original pulse frequency and the trailing pulse being blue shifted. It is at this

point that the pulse experiences self-steepening effects [156] which pushes the highest intensity to the rear of the trailing pulse due to the nonlinear index. This causes the trailing edge of the pulse to steepen to the point where the intensity falls as quickly as dispersion allows. This rapidly varying intensity on the blue edge of the pulse creates a large phase jump and results in a pulse with a broad blue shifted spectrum.

The scheme for generating NIR pulses is shown in Figure 3.7 and is based on the work by [157]. To create the pump and signal beams, the ~100 μJ sub picosecond pulses from the regenerative amplifier are first split via a half waveplate/ TFP combination. Approximately 30 % of the pulse energy is transmitted through the TFP while the other 70 % is reflected. The transmitted beam is then focused by an f = 10 cm lens into a 1 cm long undoped YAG rod. This creates enough intensity within the material to induce SCG, producing light from the visible through the IR and acts as a broadband signal for the subsequent DFG. The 1 μm light reflected from the TFP is then focused into a BBO crystal (θ=23.4°,ϕ=90°) where SHG produces light at ~515 nm. Approximately 25 % conversion efficiency is achieved in this process giving ~20 μJ of green light. Following this SHG, the beam is incident on a mirror optimized to reflect green light. This directs the 515 nm light to pump the DFG while the unconverted 1 μm light is transmitted and will be used as the pump in the following OPA pre-amplifier. The broad bandwidth signal beam and 515 nm pump beam are then focused into a BBO crystal similar to the one used for SHG with a small, i.e. 1-2 degrees, non-collinear angle.

Figure 3.8a shows a spectrum of the DFG signal beam. The red line shows the unamplified spectrum from the SCG while the blue is the spectrum after amplification. The presence of amplification in the signal also indicates the generation of an idler beam at a wavelength equal to the energy difference of the pump at amplified signal wavelength. By adjustment of the phase matching angle of the BBO crystal and the pump-signal non-collinear angle, it was possible to select the signal wavelength which was amplified. Selection and amplification of the signal pulse energy allowed us to simultaneously generate and optimize the idler wavelength for future amplification. Figure 3.8b shows the various idler wavelengths attained for different

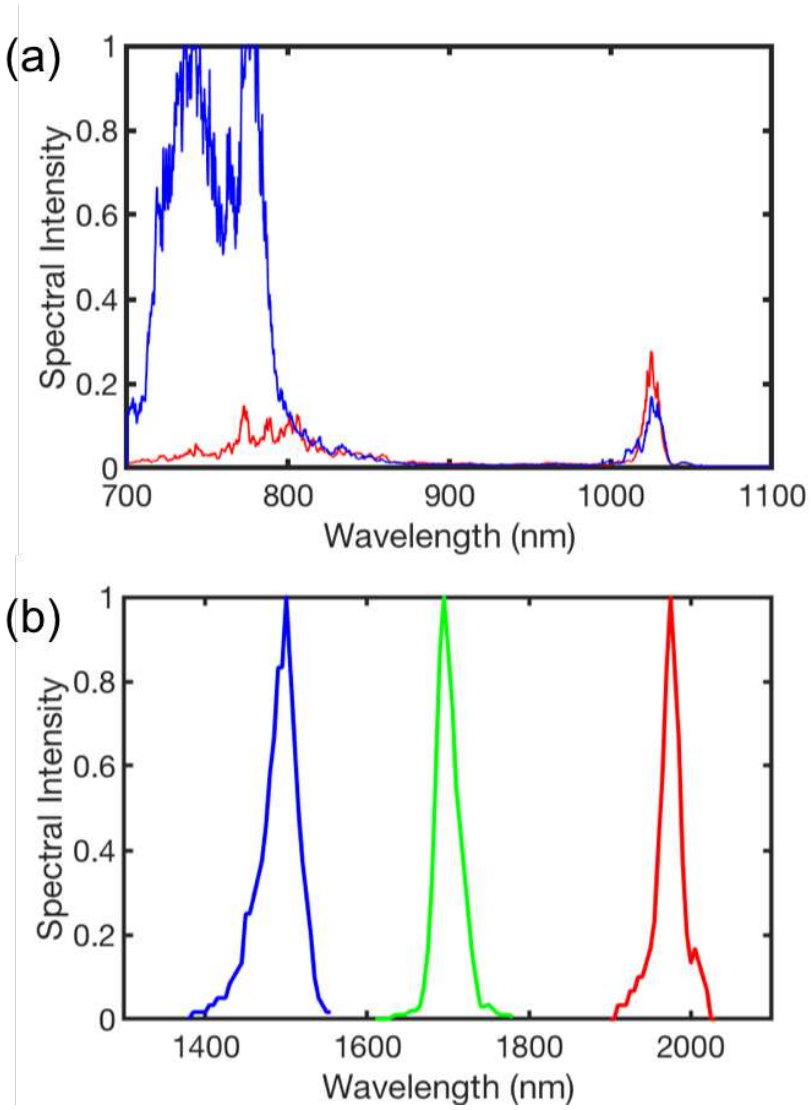

Figure 3.8: a) shows a spectrum of the DFG seed beam. The red line shows the unamplified spectrum while the blue is the spectrum after amplification. The spectral intensity is normalized to the same scale to illustrate amplification of the ~750 nm signal beam. Unconverted 1 µm light from the SCG can be seen here as well. b) Spectra from the first NIR OPA stage with the DFG idler optimized for center wavelengths ranging from less than 1.5 µm to just under 2 µm.

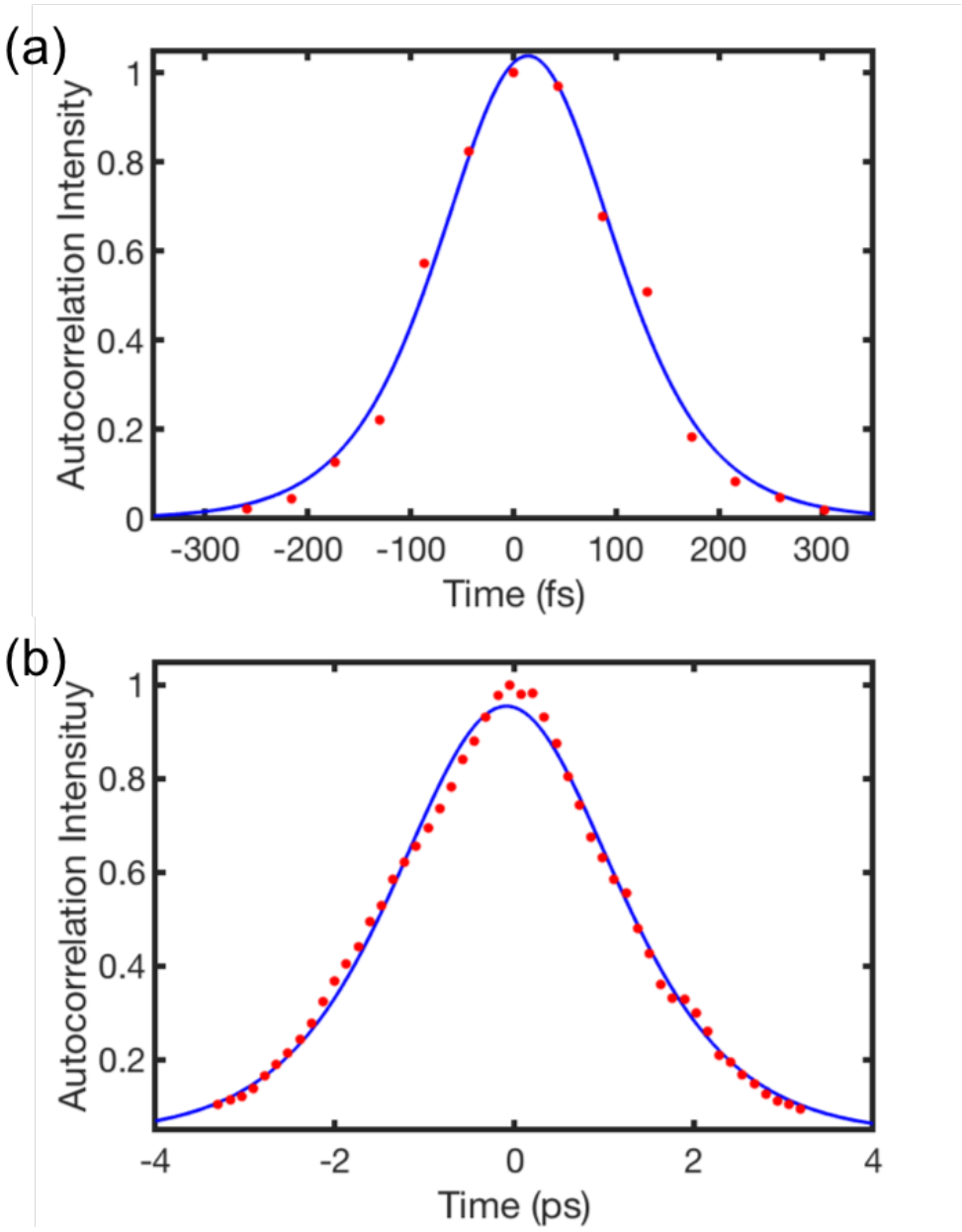

Figure 3.9: shows the SHG intensity autocorrelation of the NIR pulses after amplification in the type II KTP OPA pre-amplifier before and after temporal pulse stretching in a dielectric grating stretcher. The unstretched pulse duration, shown in a), was measured to have a sech^2 FWHM of 200 fs, while the duration after stretching, shown in b), was determined to be 2.9 ps. For these measurements the OPCPA was tuned to a wavelength of $\lambda = 1.55\,\mu\text{m}$.

phase matching conditions in the DFG stage. These spectra were measured with a scanning monochromator and an InGaAs photodiode sensitive to the NIR. It can be seen that by adjustment of the non-collinear angle and phase matching angle in the DFG, wavelengths ranging 1.5 µm to nearly 2 µm were achieved.

After DFG, idler pulses then become the sinal for type II OPA in KTP (5x5x2 mm, θ=45.5°, ϕ=0°). This pre-amplifier is pumped using the ~60 µJ of unconverted 1 µm light from the SHG and boosts the NIR pulse energy to the microjoule level before temporal pulse stretching. The pulse duration after this stage, shown by the SHG intensity autocorrelation in Figure 3.9a, has a sech^2 FWHM of 200 fs. To avoid detrimental non-linear effects and ensure good temporal overlap between the signal and pump pulses in the following amplification stages, the NIR pulses are stretched to ~3 ps in a Martinez style temporal pulse stretcher. Figure 3.9b shows the intensity autocorrelation of the pulses, optimized for 1.6 µm, after the stretcher.

3.6 Multi-Stage OPA

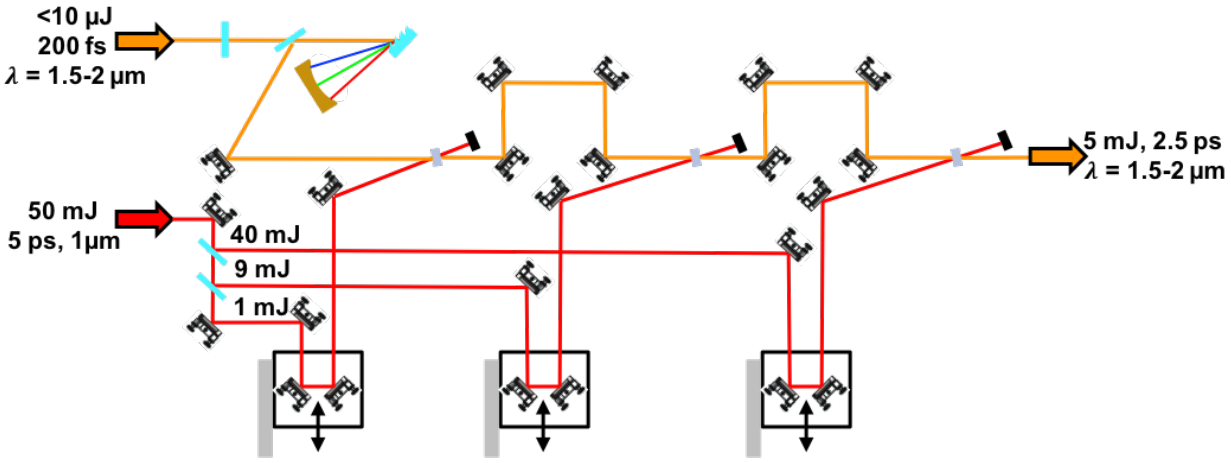

Figure 3.10: A schematic of the IR grating pulse stretcher and subsequent type II OPA stages. The microjoule level pulses from the system front end are amplified by λ = 1µm, ~50 mJ, 5 ps pulses from the cryogenic Yb:YAG laser to a pulse energy of nearly 5 mJ after the final OPA stage.

Following the DFG/OPA front end, the microjoule level NIR pulses are amplified to the millijoule level in a multi-stage type II OPA chain. This system is pumped by ~50 mJ, 5 ps pulses

from the 100 Hz cryogenic Yb:YAG laser. [34] The configuration for the amplifier is shown in Figure 3.10. The pump beam is split by two 90/10 beam splitters to provide 1 mJ, 9 mJ, and 40 mJ to amplifiers one through three respectively. The first two OPAs use 6 mm thick KTP (θ=45.5°,ϕ=0°) crystals while the final amplifier uses a 10 mm thick KTP (θ=45.5°,ϕ=0°) crystal. The phase matching and non-collinear angles were optimized in each stage depending on the signal wavelength. Figure 3.11 shows the output energy at 1.6 µm from the final KTP crystal as a function of total 1 µm pump energy into all three KTP amplification stages. We see that pulse energies of nearly 5 mJ were achieved, which is more than sufficient for the subsequent damage threshold measurements. Due to the unknown damage threshold of the compressor gratings, no attempt was made to compress the amplified pulses. Based on the bandwidths of the spectrum shown in Figure 3.8b, a transform limited pulse duration of 60-160 fs could be expected depending on the amplified wavelength.

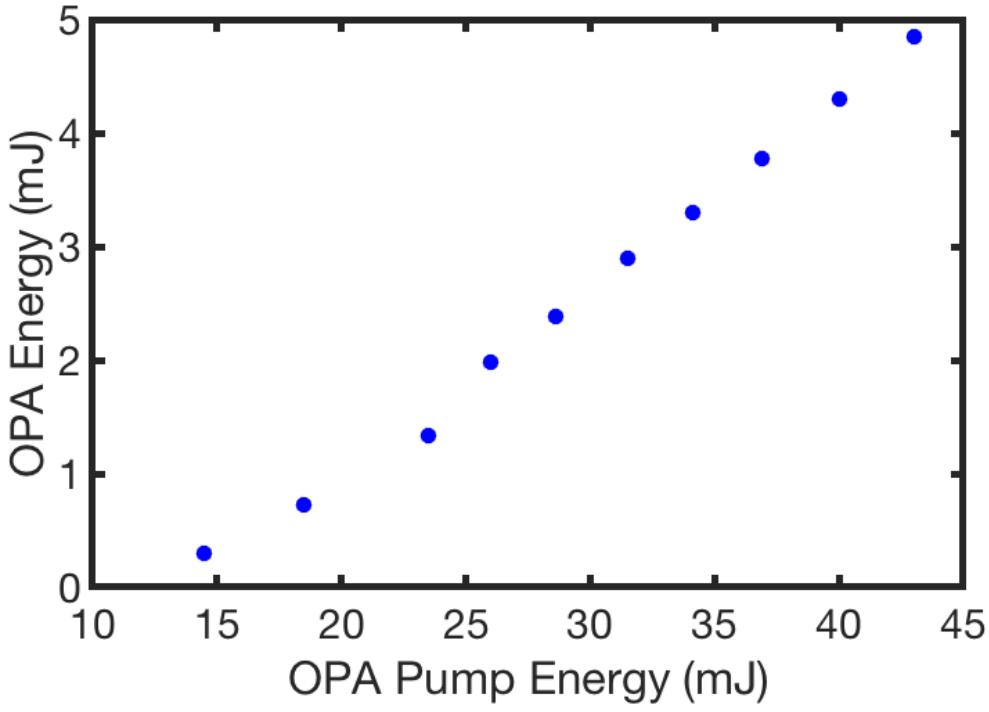

Figure 3.11: The output energy from the final KTP OPA stage as a function of 1 µm pulse energy into the final three OPA stages. Here, a maximum pulse energy of 4.85 mJ was obtained at a center wavelength of 1.6 µm.

3.7 Laser Induced Damage Testing

Damage testing of high reflectance (HR) or high transmittance anti-reflection (AR) coatings was performed by focusing the NIR pulses onto the front surface of the target of interest. Figure 3.12a shows the setup for these tests. Each damage site was irradiated with 100 pulses at 100 Hz repetition rate and ten sites were damaged for a given pulse energy. The combination of a half waveplate and polarizing beam cube were used to precisely control the pulse energy on target and this pulse energy was recorded for each waveplate position before damage testing. Damage was identified in situ by observing the scatter of a HeNe laser which was aligned to the same spot on the substrate as the NIR damaging pulses. These damage sites were later confirmed using a Nomarski microscope.

Due to the prohibitively high cost of cameras sensitive to the wavelengths of interest, the laser's spot size at the surface of the substrate was determined using a knife edge measurement technique. A razor blade was attached to a linear translation stage and the pulse intensity was recorded on NIR sensitive InGaAs photodiode (PD) as the razor blade was scanned transversely across the beam. This was performed in both the x and y axes of the beam and the resulting curves were fit to the following function to determine the x and y waist values.

$$P(x) = \frac{P1}{2}\left[1 + erf\left(\frac{\sqrt{2}(x - P2)}{P3}\right)\right] + P4 \tag{3.52}$$

where $P(x)$ is the measured PD intensity at position x, x is the position of the translation stage in mm, $P1$ is the functions amplitude, $P2$ is an offset in x, $P3 = 1/e^2$ radius of a Gaussian, and $P4$ is the background offset.

From this analysis, the beam was found to regularly have a FWHM of ~110 μm along each axis. Figure 3.12b shows the reconstructed beam profile based on this analysis with waist values of 106 μm and 114 μm along the x and y axes respectively and demonstrates the highly symmetric Gaussian shape of the beam used for LIDT.

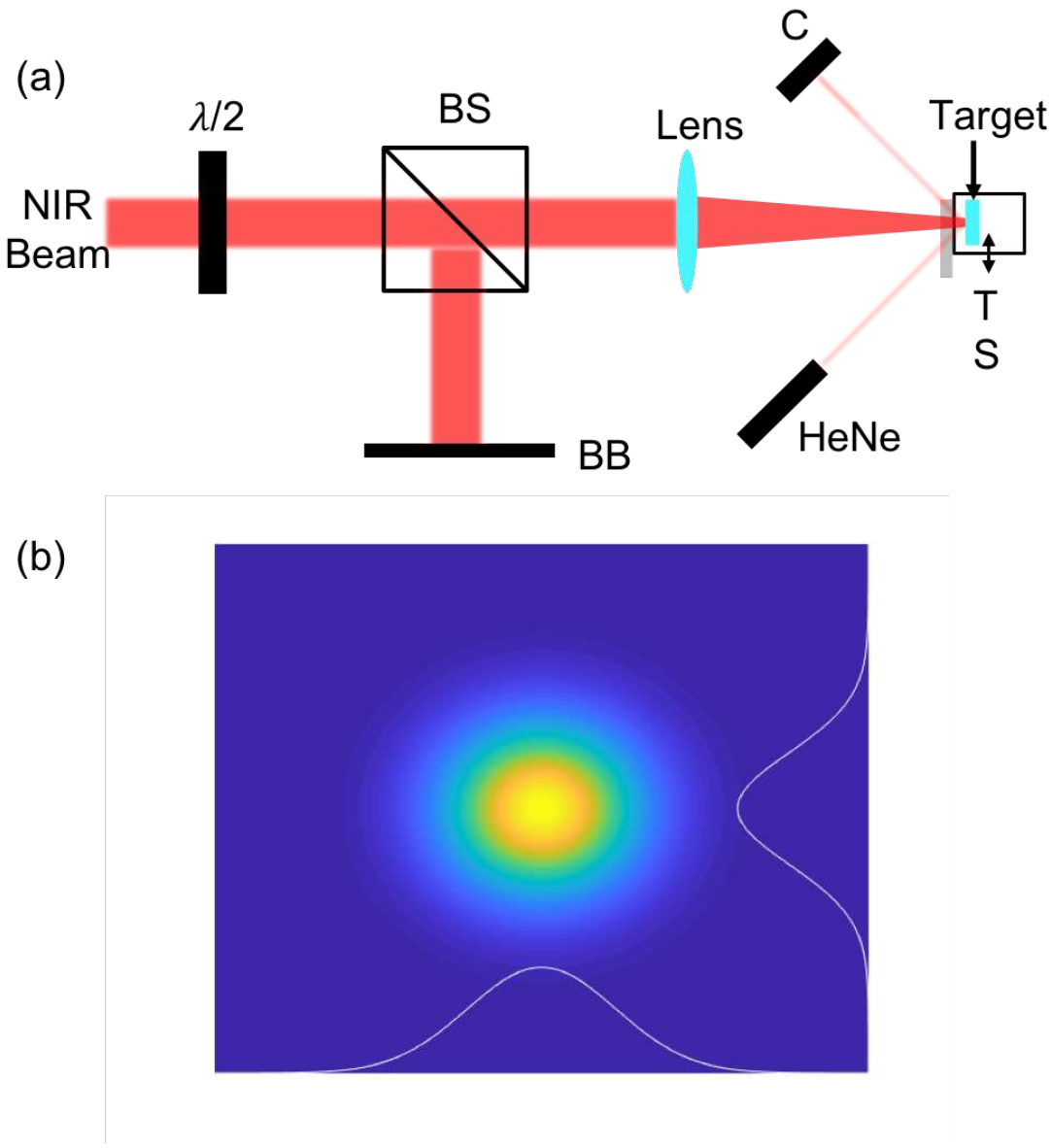

Figure 3.12: a) A schematic of the LIDT setup. $\lambda/2$: half waveplate, BS: beam splitter, BB: beam block, C: camera, TS: linear translation stage. b) A reconstruction of the amplified 1.6 µm beam profile from the fitted knife edge data. The beam has a waist radius of 106 µm along its x-axis and 114 µm along its y-axis.

3.8 LIDT Results and Discussion

The results of damage threshold measurements for various optical coating designs and low OH fused silica are reported in Table 3.1. Also present in this table are the band gaps for the high index material used in the coating as well as the band gap for bulk fused silica. The optical coatings were fabricated by Dinesh Patel at Colorado State University using ion beam sputtering deposition. Drew Schiltz designed the coatings, optimizing for either reflectance (HR) or high transmittance (AR) at 1.6 μm while maintaining a high damage threshold suitable for high power laser operation. The coatings are designed as quarter-wave "stacks", in which the layer thickness of the deposited material is approximately one quarter wavelength of the light of interest. By varying the material of each layer, and thereby the index of refraction, light reflected at the interfaces of differing materials can be made to constructively or destructively interfere, providing either exceptionally high reflectance or transmittance over a wavelength range of interest. For more information on the design of the optical coatings, refer to [145]. To the authors knowledge, these are the first reported results of threshold damage fluence at 1.6 μm with picoseconds duration pulses.

Table 3.1 reports the damage thresholds of various Ta_2O_5/SiO_2 HR, Y_2O_3/SiO_2 HR , and HfO_2/SiO_2 HR optical coating designs, and a HfO_2/SiO_2 AR coating. As a reference, the damage threshold of low OH IR fused silica (IRFS) was also measured. These values correspond to the highest fluence at which no damage was observed.

Table 3.1: Measured damage threshold of for HR: high reflection and AR: anti-reflection optical coatings at λ=1.6 μm.

Substrate	Material Band Gap (eV)	Damage Threshold (J/cm^2)
IRFS	9	5.86 ± 1.61
Ta_2O_5/SiO_2 HR	3.5	4.88 ± 1.40
Y_2O_3/SiO_2 HR	5.1	8.47 ± 2.42
HfO_2/SiO_2 HR	5.1	8.67 ± 2.42
HfO_2/SiO_2 AR	5.1	7.79 ± 2.21

To understand the damage mechanism of materials, the following rate equation is typically used to model the density of conduction band electrons [158]

$$\frac{\partial n_e}{\partial t} = W_{PI}\big(I(t)\big) + W_{AV}\big(I(t), n_e(t)\big) - W_R\big(n_e(t), t\big) \tag{3.53}$$

In the above equation, the term W_{PI} is referred to as the photoionization rate, W_{AV} is the avalanche ionization rate, and W_R is the relaxation rate of electrons out of the conduction band. This last term is typically defined as

$$W_R = \frac{n_e(t)}{\tau_R} \tag{3.54}$$

where τ_R is the relaxation time for all processes which support decay of electrons from the conduction band and is determined from experimental data. [158] Damage occurs when the density of free electrons reaches the critical plasma density which is the point when the plasma frequency corresponds to the incident laser frequency.

The accepted model for photoionization was described by Keldysh. [159] Based on this work, photoionization can be caused by either tunnel ionization or multi-photon ionization, and the dominate ionization mechanism can be characterized by the Keldysh parameter γ.

$$\gamma = \frac{\omega}{e}\sqrt{\frac{m_e c n \varepsilon_0 E_g}{I_0}} \tag{3.55}$$

where ω is the laser frequency, e is the electron charge, m_e is the electron reduced mass, c is the speed of light, n is the material index of refraction, ε_0 is the permittivity of free space, E_g is the material band gap, and I_0 is the peak laser intensity. For cases when γ<1.5, tunnel ionization is the dominate process, when γ>1.5 multi-photon dominates, and when γ is near 1.5 both processes contribute. Briefly, tunnel ionization occurs when a strong electric field suppresses the potential barrier of an atom enough to allow a valence electron to tunnel through the reduced potential barrier into the conduction band. Multi-photon ionization occurs when

multiple photons with energy below the ionization potential are simultaneously incident on an atom, causing it to ionize.

Avalanche ionization is the other key effect which promotes electrons to the conduction band. This process occurs when an electron in the conduction band absorbs radiation up to the point when it has a kinetic energy equal to the band gap. This energetic electron then collisionally ionizes a valence electron, and the process repeats, now with an additional conduction band electron. From equation (3.53), It can be seen that the rate of avalanche ionization is dependent upon the number of conduction band electrons, $n_e(t)$. Therefore, in pulse durations on the order of a few picoseconds, photoionization acts as a seed for avalanche ionization. An accurate description for this process is still a source of research. [160–162] Many of the proposed models are phenomenological and therefore trying to discern an accurate understanding of the physics of this process across many wavelengths and pulse durations is difficult.

The results in Table 3.1 illustrate two features which are important for understanding the damage mechanisms of optical coatings and bulk material. The first is that the damage threshold of the samples is observed to scale with the band gap of the material, with the obvious exception that the bulk fused silica did not have the highest damage threshold. The unexpected lower damaged threshold of fused silica will need to be corroborated in the future. This band gap dependent relation appears to be consistent with other shorter wavelength LIDT measurements of materials with differing band gaps [148, 163, 164].

The second feature these results demonstrate is that the damage threshold for dielectric materials increases as the laser wavelength increases. The results reported here at λ = 1.6 μm are higher than those reported for lower wavelengths with similar pulse duration [147, 163], following the wavelength dependent scaling reported for shorter wavelengths. [148, 149, 164] At a pulse duration of ~3 ps, Stuart et al. found the LIDT of fused silica to be ~1.5 J/cm^2 at 526 nm and ~3 J/cm^2 at 1.053 μm. Our results follow closely with this wavelength dependent scaling and demonstrate one of the first results in a new wavelength regime for LIDT. Yet other studies have reported that this trend shows an opposite behavior at longer wavelengths, in the mid-

IR. [149] The measurement reported here provides an important benchmark for understanding the wavelength dependence of optical damage.

While typically a complex model is necessary for an accurate assessment of LIDT, Gamaly et al. derived a relatively simple relation to describe LIDT of dielectric materials in the ultrafast (< 1 ps), high intensity (~10^{14} W/cm^2) regime. [146] In this regime, the laser-matter interaction is characterized by the condition that the pulse duration is significantly shorter than the electron-ion energy transfer time and the heat conduction time. In this way the ions remain cold during the interaction process and all absorbed laser energy is transferred to electron thermal energy. With sufficient pulse intensity, electron energies can exceed the Fermi energy, and electrons are liberated from the target. This creates a charge separation that pulls ions from the target leading to ablation of the material. From the analysis in [146], the following equations were derived to characterize the damage fluence of a dielectric material in this ultrafast, high intensity regime.

$$F_{th}^{d} = \frac{3}{4}\left(\epsilon_b + J_i\right)\frac{l_s n_e}{A} \tag{3.56}$$

$$\frac{A}{l_s} \approx \frac{2\omega}{c}\left(1 + \frac{1}{n} + \frac{1}{2n^2}\right)^{-1} \tag{3.57}$$

Here, ϵ_b is the binding energy of ions to the lattice, J_i is the ionization potential, n_e is the electron number density, A/l_s is the ratio of the absorption to skin depth, ω is the laser frequency, and n is the index of refraction.

This model is notable in that it predicts the damage threshold within this intensity and pulse duration regime is only dependent on radiation wavelength and material properties, i.e. band gap and index of refraction. While the laser conditions used to derive equation (3.56) do not precisely match the laser conditions used to obtain the above results, it still serves as a good guide for assessing damage fluence and follows closely with the trends seen in these results. If we employ equation (3.56) to predict the damage fluence of fused silica at 1.6 μm, we find that the model predicts a LIDT of 4.8 J/cm^2. While this value is lower than the measured value shown in Table 3.1, it is important to remember that this model was based on approximations using

higher intensities and shorter pulses than those used in this experiment. Furthermore, if one looks at Gamaly et al's own assessment of the model's predictions, which uses data from [160] for 526 nm and 1.053 μm, and [3] for 825 nm, we see good agreement for pulse durations below 1 ps and above 10 ps (a separate long pulse duration approximation was also made in [146] but isn't shown here). Notably, the model is least accurate in the 1-10 ps regime and under predicts LIDT at longer wavelengths. Therefore, we would expect to measure a higher value than equation (3.56) predicts.

3.9 Summary

A NIR OPCPA laser system was developed which is tunable from λ = 1.5 - 2 μm and capable of producing pulse energies up to 5 mJ at 100 Hz repetition rate with an uncompressed pulse duration of ~2.5 ps. This laser was used to perform LIDT testing on bulk fused silica and various high damage threshold optical coatings designed for operation at λ = 1.6 μm. These results indicate a relation between laser wavelength, material band gap, and LIDT and are the first reported results that the author knows of at this wavelength and pulse duration. These findings help to inform the mechanisms of LID and will provide important information for future optical coating designs for eye safe lasers.

Chapter 4

Summary

The development of high energy ultrafast lasers at ever higher repetitions rates is a key technology for enabling numerous scientific, medical and industrial applications. Techniques for producing the energetic x-rays, gamma rays, isotopes, and neutrons necessary for these applications have been demonstrated by current high energy, low repetition rate ultrashort pulse laser systems. The increased repetition rate and high pulse energy of new high average power ultrafast lasers, such as the one described in this dissertation, will provide a higher flux of photons and energetic particles. This will make materials processing, x-ray imaging procedures, and medical therapies time and cost efficient, and will ease experimental stability requirements by decreasing data acquisition times. Besides enabling specific applications, high repetition rates open new opportunities for the incorporation of machine learning to provide feedback in experiments with high energy lasers. These feedback controls may be used not only to maintain the long-term stability of a laser system or experiment but also provide the potential to efficiently optimize experiments over large parameter spaces.

This dissertation demonstrated the first CPA laser capable of producing >1 J of pulse energy with a pulse duration below 5 ps at a repetition rate of 500 Hz. This laser system was further expanded to obtain an initial, short runtime demonstration of joule-level energies at 1 kHz. The approach for achieving >1 J, picosecond pulses at kHz-level repetition rates utilized a diode-pumped cryogenically-cooled, thick-disk Yb:YAG active mirror multi-pass amplifier. This design takes advantage of the enhanced material and spectroscopic properties of Yb:YAG when cooled to cryogenic temperature while maintaining the efficient heat removal characteristic of thin-disk amplifiers.

This CPA laser was used to demonstrate soft x-ray lasing in Ni-like molybdenum at a record repetition rate of 400 Hz. 1 J pulses exiting the compressor were focused to a high aspect ratio line onto a polished molybdenum target at a grazing incidence angle of 29 degrees. Strong

lasing was observed at 18.9 nm and runs of 4000 consecutive shots were recorded. The 400 Hz results demonstrated here constitute the highest repetition rate, tabletop SXRL to date, and provides a potential source for laboratory scale SXRL experiments.

Additionally, a 100 Hz picosecond cryogenic Yb:YAG version of this laser was used as the pump source for a near-infrared (NIR) OPCPA laser which was tunable between 1.5 and 2 μm. This laser was used to perform laser induced damage testing (LIDT) of optical coatings at 1.6 μm. This system consisted of a ~100 μJ, sub-ps Yb:KYW regenerative amplifier which was used to generate NIR pulses in an initial DFG stage. The generated NIR pulses were subsequently amplified in three OPA stages to obtain a maximum pulse energy of 5 mJ. The three stages of OPA were pumped by λ = 1.03 μm, 50 mJ, ~5 ps pulses from a cryogenically cooled Yb:YAG CPA laser. Both the NIR OPCPA laser and 1.03 μm CPA pump laser were seeded by a common Yb:KYW oscillator allowing for passive temporal synchronization of pump and signal pulses. λ = 1.6 μm, ~2.5 ps pulses were used to conduct LIDT measurements on a number of high damage threshold optical coatings designed for operation near this wavelength. These constitute the first reported results of short pulse LIDT of optical coatings at this wavelength, providing an important benchmark for understanding LIDT mechanisms in this wavelength regime.

Bibliography

[1] Donna Strickland and Gerard Mourou. Compression of amplified chirped optical pulses. *Optics Communications*, 56(3):219–221, December 1985.

[2] P. F. Moulton. Spectroscopic and laser characteristics of Ti:Al2O3. *J. Opt. Soc. Am. B*, 3(1):125–133, Jan 1986.

[3] M. D. Perry, D. Pennington, B. C. Stuart, G. Tietbohl, J. A. Britten, C. Brown, S. Herman, B. Golick, M. Kartz, J. Miller, H. T. Powell, M. Vergino, and V. Yanovsky. Petawatt laser pulses. *Opt. Lett.*, 24(3):160–162, Feb 1999.

[4] Colin Danson, David Hillier, Nicholas Hopps, and David Neely. Petawatt class lasers worldwide. *High Power Laser Science and Engineering*, 3:e3, 2015.

[5] Yuxi Chu, Xiaoyan Liang, Lianghong Yu, Yi Xu, Lu Xu, Lin Ma, Xiaoming Lu, Yanqi Liu, Yuxin Leng, Ruxin Li, and Zhizhan Xu. High-contrast 2.0 petawatt Ti:sapphire laser system. *Opt. Express*, 21(24):29231–29239, Dec 2013.

[6] Tae Jun Yu, Seong Ku Lee, Jae Hee Sung, Jin Woo Yoon, Tae Moon Jeong, and Jongmin Lee. Generation of high-contrast, 30 fs, 1.5 PW laser pulses from chirped-pulse amplification Ti:sapphire laser. *Opt. Express*, 20(10):10807–10815, May 2012.

[7] Zebiao Gan, Lianghong Yu, Shuai Li, Cheng Wang, Xiaoyan Liang, Yanqi Liu, Wenqi Li, Zhen Guo, Zutao Fan, Xiaolong Yuan, Lu Xu, Zhengzheng Liu, Yi Xu, Jun Lu, Haihe Lu, Dingjun Yin, Yuxin Leng, Ruxin Li, and Zhizhan Xu. 200 J high efficiency Ti:sapphire chirped pulse amplifier pumped by temporal dual-pulse. *Opt. Express*, 25(5):5169–5178, Mar 2017.

[8] Wenqi Li, Zebiao Gan, Lianghong Yu, Cheng Wang, Yanqi Liu, Zhen Guo, Lu Xu, Min Xu, Yin Hang, Yi Xu, Jianye Wang, Pei Huang, He Cao, Bo Yao, Xiaobo Zhang, Lingru Chen, Yunhai Tang, Shuai Li, Xingyan Liu, Shanming Li, Mingzhu He, Dinjun Yin, Xiaoyan Liang,

Yuxin Leng, Ruxin Li, and Zhizhan Xu. 339 J high-energy Ti: sapphire chirped-pulse amplifier for 10 PW laser facility. *Opt. Lett.*, 43(22):5681–5684, Nov 2018.

[9] Yasukazu Izawa, Noriaki Miyanaga, Junji Kawanaka, and Koichi Yamakawa. High power lasers and their new applications. *J. Opt. Soc. Korea*, 12(3):178–185, Sep 2008.

[10] WP Leemans, J Daniels, A Deshmukh, AJ Gonsalves, A Magana, HS Mao, DE Mittelberger, K Nakamura, JR Riley, D Syversrud, et al. Bella laser and operations. *Proc. of PAC2013*, page THYAA11097, 2013.

[11] Yong Wang, Shoujun Wang, Alex Rockwood, Bradley M. Luther, Reed Hollinger, Alden Curtis, Chase Calvi, Carmen S. Menoni, and Jorge J. Rocca. 0.85 PW laser operation at 3.3 hz and high-contrast ultrahigh-intensity λ = 400 nm second-harmonic beamline. *Opt. Lett.*, 42(19):3828–3831, Oct 2017.

[12] E. Sistrunk, T. Spinka, A. Bayramian, S. Betts, R. Bopp, S. Buck, K. Charron, J. Cupal, R. Deri, M. Drouin, A. Erlandson, E. S. Fulkerson, J. Horner, J. Horacek, J. Jarboe, K. Kasl, D. Kim, E. Koh, L. Koubikova, R. Lanning, W. Maranville, C. Marshall, D. Mason, J. Menapace, P. Miller, P. Mazurek, A. Naylon, J. Novak, D. Peceli, P. Rosso, K. Schaffers, D. Smith, J. Stanley, R. Steele, S. Telford, J. Thoma, D. VanBlarcom, J. Weiss, P. Wegner, B. Rus, and C. Haefner. All Diode-Pumped, High-repetition-rate Advanced Petawatt Laser System (HAPLS). In *Conference on Lasers and Electro-Optics*, page STh1L.2. Optical Society of America, 2017.

[13] Junji Kawanaka, Koichi Yamakawa, Hajime Nishioka, and Ken ichi Ueda. 30-mJ, diode-pumped, chirped-pulse Yb:YLF regenerative amplifier. *Opt. Lett.*, 28(21):2121–2123, Nov 2003.

[14] Kyung-Han Hong, Juliet T. Gopinath, Darren Rand, Aleem M. Siddiqui, Shu-Wei Huang, Enbang Li, Benjamin J. Eggleton, John D. Hybl, Tso Yee Fan, and Franz X. Kärtner. High-

energy, kHz-repetition-rate, ps cryogenic Yb:YAG chirped-pulse amplifier. *Opt. Lett.*, 35(11):1752–1754, Jun 2010.

[15] Dimitrios N. Papadopoulos, Alain Pellegrina, Lourdes Patricia Ramirez, Patrick Georges, and Frédéric Druon. Broadband high-energy diode-pumped Yb:KYW multipass amplifier. *Opt. Lett.*, 36(19):3816–3818, Oct 2011.

[16] J. Tümmler, R. Jung, H. Stiel, P. V. Nickles, and W. Sandner. High-repetition-rate chirped-pulse-amplification thin-disk laser system with joule-level pulse energy. *Opt. Lett.*, 34(9):1378–1380, May 2009.

[17] Robert Jung, Johannes Tümmler, Thomas Nubbemeyer, and Ingo Will. Thin-disk ring amplifier for high pulse energy. *Opt. Express*, 24(5):4375–4381, Mar 2016.

[18] Luis E. Zapata, Hua Lin, Anne-Laure Calendron, Huseyin Cankaya, Michael Hemmer, Fabian Reichert, W. Ronny Huang, Eduardo Granados, Kyung-Han Hong, and Franz X. Kärtner. Cryogenic Yb:YAG composite-thin-disk for high energy and average power amplifiers. *Opt. Lett.*, 40(11):2610–2613, Jun 2015.

[19] Chun-Lin Chang, Peter Krogen, Kyung-Han Hong, Luis E. Zapata, Jeffrey Moses, Anne-Laure Calendron, Houkun Liang, Chien-Jen Lai, Gregory J. Stein, Phillip D. Keathley, Guillaume Laurent, and Franz X. Kärtner. High-energy, kHz, picosecond hybrid Yb-doped chirped-pulse amplifier. *Opt. Express*, 23(8):10132–10144, Apr 2015.

[20] Thomas Metzger, Alexander Schwarz, Catherine Yuriko Teisset, Dirk Sutter, Alexander Killi, Reinhard Kienberger, and Ferenc Krausz. High-repetition-rate picosecond pump laser based on a Yb:YAG disk amplifier for optical parametric amplification. *Opt. Lett.*, 34(14):2123–2125, Jul 2009.

[21] Hanieh Fattahi, Ayman Alismail, Haochuan Wang, Jonathan Brons, Oleg Pronin, Theresa Buberl, Lénárd Vámos, Gunnar Arisholm, Abdallah M. Azzeer, and Ferenc Krausz. High-

power, 1-ps, all-Yb:YAG thin-disk regenerative amplifier. *Opt. Lett.*, 41(6):1126–1129, Mar 2016.

[22] Darren A. Rand, Scot E. J. Shaw, Juan R. Ochoa, Daniel J. Ripin, Andrew Taylor, Tso Yee Fan, Hector Martin, Scott Hawes, Jim Zhang, Samvel Sarkisyan, Eric Wilson, and Paul Lundquist. Picosecond pulses from a cryogenically cooled, composite amplifier using Yb:YAG and Yb:GSAG. *Opt. Lett.*, 36(3):340–342, Feb 2011.

[23] Daniel E. Miller, Luis E. Zapata, Daniel J. Ripin, and Tso Yee Fan. Sub-picosecond pulses at 100 W average power from a Yb:YLF chirped-pulse amplification system. *Opt. Lett.*, 37(13):2700–2702, Jul 2012.

[24] Jakub Novák, Jonathan T. Green, Thomas Metzger, Tomáš Mazanec, Bedřich Himmel, Martin Horáček, Zbyněk Hubka, Robert Boge, Roman Antipenkov, František Batysta, Jack A. Naylon, Pavel Bakule, and Bedřich Rus. Thin disk amplifier-based 40 mJ, 1 kHz, picosecond laser at 515 nm. *Opt. Express*, 24(6):5728–5733, Mar 2016.

[25] Jonathan Fischer, Alexander-Cornelius Heinrich, Simon Maier, Julian Jungwirth, Daniele Brida, and Alfred Leitenstorfer. 615 fs pulses with 17 mJ energy generated by an Yb:thin-disk amplifier at 3 kHz repetition rate. *Opt. Lett.*, 41(2):246–249, Jan 2016.

[26] Thomas Nubbemeyer, Martin Kaumanns, Moritz Ueffing, Martin Gorjan, Ayman Alismail, Hanieh Fattahi, Jonathan Brons, Oleg Pronin, Helena G. Barros, Zsuzsanna Major, Thomas Metzger, Dirk Sutter, and Ferenc Krausz. 1 kW, 200 mJ picosecond thin-disk laser system. *Opt. Lett.*, 42(7):1381–1384, Apr 2017.

[27] Sandro Klingebiel, Christoph Wandt, Christoph Skrobol, Izhar Ahmad, Sergei A. Trushin, Zsuzsanna Major, Ferenc Krausz, and Stefan Karsch. High energy picosecond Yb:YAG CPA system at 10 Hz repetition rate for pumping optical parametric amplifiers. *Opt. Express*, 19(6):5357–5363, Mar 2011.

[28] F. X. Morrissey, T. Y. Fan, D. E. Miller, and D. Rand. Picosecond kilohertz-class cryogenically cooled multistage Yb-doped chirped pulse amplifier. *Opt. Lett.*, 42(4):707–710, Feb 2017.

[29] Bruno E. Schmidt, Arvid Hage, Torsten Mans, François Légaré, and Hans Jakob Wörner. Highly stable, 54 mJ Yb-Innoslab laser platform at 0.5 kW average power. *Opt. Express*, 25(15):17549–17555, Jul 2017.

[30] Clemens Herkommer, Peter Krötz, Sandro Klingebiel, Christoph Wandt, Dominik Bauer, Knut Michel, Reinhard Kienberger, and Thomas Metzger. Towards a Joule-Class Ultrafast Thin-Disk Based Amplifier at Kilohertz Repetition Rate. In *Conference on Lasers and Electro-Optics*, page SM4E.3. Optical Society of America, 2019.

[31] Federico J. Furch, Brendan A. Reagan, Bradley M. Luther, Alden H. Curtis, Shaun P. Meehan, and Jorge J. Rocca. Demonstration of an all-diode-pumped soft x-ray laser. *Opt. Lett.*, 34(21):3352–3354, Nov 2009.

[32] Brendan A. Reagan, Cory Bamgarten, Keith Wernsing, Herman Bravo, Mark Woolston, Alden Curtis, Federico J. Furch, Bradley M. Luther, Dinesh Patel, Carmen S. Menoni, and Jorge J. Rocca. 1 Joule, 100 Hz Repetition Rate, Picosecond CPA Laser for Driving High Average Power Soft X-Ray Lasers. In *CLEO: 2014*, page SM1F.4. Optical Society of America, 2014.

[33] Cory Baumgarten, Michael Pedicone, Herman Bravo, Hanchen Wang, Liang Yin, Carmen S Menoni, Jorge J Rocca, and Brendan A Reagan. 1 J, 0.5 kHz repetition rate picosecond laser. *Optics letters*, 41(14):3339–3342, 2016.

[34] A. H. Curtis, B. A. Reagan, K. A. Wernsing, F. J. Furch, B. M. Luther, and J. J. Rocca. Demonstration of a compact 100 Hz, 0.1 J, diode-pumped picosecond laser. *Opt. Lett.*, 36(11):2164–2166, Jun 2011.

[35] A. Giesen, H. Hügel, A. Voss, K. Wittig, U. Brauch, and H. Opower. Scalable concept for diode-pumped high-power solid-state lasers. *Applied Physics B*, 58(5):365–372, May 1994.

[36] Marco Kienel, Michael Müller, Arno Klenke, Jens Limpert, and Andreas Tünnermann. 12 mJ kW-class ultrafast fiber laser system using multidimensional coherent pulse addition. *Optics letters*, 41(14):3343–3346, 2016.

[37] Michael Mueller, Arno Klenke, Henning Stark, Joachim Buldt, Thomas Gottschall, Andreas Tünnermann, and Jens Limpert. 1.8-kW 16-channel ultrafast fiber laser system. In *Fiber Lasers XV: Technology and Systems*, volume 10512, page 1051208. International Society for Optics and Photonics, 2018.

[38] Anne-Laure Calendron, Hüseyin Çankaya, and Franz X. Kärtner. High-energy kHz Yb:KYW dual-crystal regenerative amplifier. *Opt. Express*, 22(20):24752–24762, Oct 2014.

[39] E. Caracciolo, M. Kemnitzer, A. Guandalini, F. Pirzio, A. Agnesi, and J. Aus der Au. High pulse energy multiwatt Yb:CaAlGdO4 and Yb:CaF2 regenerative amplifiers. *Opt. Express*, 22(17):19912–19918, Aug 2014.

[40] M. Siebold, S. Bock, U. Schramm, B. Xu, J. L. Doualan, P. Camy, and R. Moncorgé. Yb:CaF2 — a new old laser crystal. *Applied Physics B*, 97(2):327–338, Oct 2009.

[41] C. W. Siders and C. Haefner. High-power lasers for science and society." white paper presented to the national academy of science committee on the opportunities in the science, applications, and technology of intense ultrafast lasers. Technical Report LLNL-TR-704407, Lawrence Livermore National Laboratory, Oct 2016.

[42] G. Mourou, G. Korn, W. Sandner, and J. Collier. Science and technology with ultra-intense lasers. Technical report, Extreme Light Infrastructure, 2011.

[43] S. Herriot. Active adaptive control of high-energy, high-repetition-rate, short-pulse lasers. Technical Report 16-ERD-038, Lawrence Livermore National Laboratory, 2018.

[44] Anne-Laure Calendron, Joachim Meier, Michael Hemmer, Luis E. Zapata, Fabian Reichert, Huseyin Cankaya, Damian N. Schimpf, Yi Hua, Guoqing Chang, Aram Kalaydzhyan, and et al. Laser system design for table-top X-ray light source. *High Power Laser Science and Engineering*, 6:e12, 2018.

[45] David Atwood. *Soft X-Rays and Extreme Ultraviolet Radition*. Cambridge University Press, 2000.

[46] M. Hentschel, R. Kienberger, Ch. Spielmann, G. A. Reider, N. Milosevic, T. Brabec, P. Corkum, U. Heinzmann, M. Drescher, and F. Krausz. Attosecond metrology. *Nature*, 414(6863):509–513, 2001.

[47] Iris D. Young, Mohamed Ibrahim, Ruchira Chatterjee, Sheraz Gul, Franklin D. Fuller, Sergey Koroidov, Aaron S. Brewster, Rosalie Tran, Roberto Alonso-Mori, Thomas Kroll, Tara Michels-Clark, Hartawan Laksmono, Raymond G. Sierra, Claudiu A. Stan, Rana Hussein, Miao Zhang, Lacey Douthit, Markus Kubin, Casper de Lichtenberg, Long Vo Pham, Håkan Nilsson, Mun Hon Cheah, Dmitriy Shevela, Claudio Saracini, Mackenzie A. Bean, Ina Seuffert, Dimosthenis Sokaras, Tsu-Chien Weng, Ernest Pastor, Clemens Weninger, Thomas Fransson, Louise Lassalle, Philipp Bräuer, Pierre Aller, Peter T. Docker, Babak Andi, Allen M. Orville, James M. Glownia, Silke Nelson, Marcin Sikorski, Diling Zhu, Mark S. Hunter, Thomas J. Lane, Andy Aquila, Jason E. Koglin, Joseph Robinson, Mengning Liang, Sébastien Boutet, Artem Y. Lyubimov, Monarin Uervirojnangkoorn, Nigel W. Moriarty, Dorothee Liebschner, Pavel V. Afonine, David G. Waterman, Gwyndaf Evans, Philippe Wernet, Holger Dobbek, William I. Weis, Axel T. Brunger, Petrus H. Zwart, Paul D. Adams, Athina Zouni, Johannes Messinger, Uwe Bergmann, Nicholas K. Sauter, Jan Kern, Vittal K. Yachandra, and Junko Yano. Structure of photosystem II and substrate binding at room temperature. *Nature*, 540:453–457, 11 2016.

[48] F. Calegari, D. Ayuso, A. Trabattoni, L. Belshaw, S. De Camillis, S. Anumula, F. Frassetto, L. Poletto, A. Palacios, P. Decleva, J. B. Greenwood, F. Martín, and M. Nisoli. Ultrafast elec-

tron dynamics in phenylalanine initiated by attosecond pulses. *Science*, 346(6207):336–339, 2014.

[49] Jeffrey L. Krause, Kenneth J. Schafer, and Kenneth C. Kulander. High-order harmonic generation from atoms and ions in the high intensity regime. *Phys. Rev. Lett.*, 68:3535–3538, Jun 1992.

[50] D. L. Matthews, P. L. Hagelstein, M. D. Rosen, M. J. Eckart, N. M. Ceglio, A. U. Hazi, H. Medecki, B. J. MacGowan, J. E. Trebes, B. L. Whitten, E. M. Campbell, C. W. Hatcher, A. M. Hawryluk, R. L. Kauffman, L. D. Pleasance, G. Rambach, J. H. Scofield, G. Stone, and T. A. Weaver. Demonstration of a Soft X-Ray Amplifier. *Phys. Rev. Lett.*, 54:110–113, Jan 1985.

[51] M. D. Rosen, P. L. Hagelstein, D. L. Matthews, E. M. Campbell, A. U. Hazi, B. L. Whitten, B. MacGowan, R. E. Turner, R. W. Lee, G. Charatis, Gar. E. Busch, C. L. Shepard, and P. D. Rockett. Exploding-Foil Technique for Achieving a Soft X-Ray Laser. *Phys. Rev. Lett.*, 54:106–109, Jan 1985.

[52] T. N. Lee, E. A. McLean, and R. C. Elton. Soft x-ray lasing in neonlike germanium and copper plasmas. *Phys. Rev. Lett.*, 59:1185–1188, Sep 1987.

[53] B. J. MacGowan, M. D. Rosen, M. J. Eckart, P. L. Hagelstein, D. L. Matthews, D. G. Nilson, T. W. Phillips, J. H. Scofield, G. Shimkaveg, J. E. Trebes, R. S. Walling, B. L. Whitten, and J. G. Woodworth. Observation of soft x-ray amplification in neonlike molybdenum. *Journal of Applied Physics*, 61(12):5243–5248, 1987.

[54] Joseph Nilsen and James H Scofield. Wavelengths of neon-like 3p→ 3s x-ray laser transitions. *Physica Scripta*, 49(5):588–591, may 1994.

[55] J H Scofield and B J MacGowan. Energies of nickel-like 4d to 4plaser lines. *Physica Scripta*, 46(4):361–364, oct 1992.

[56] B. J. MacGowan, S. Maxon, P. L. Hagelstein, C. J. Keane, R. A. London, D. L. Matthews, M. D. Rosen, J. H. Scofield, and D. A. Whelan. Demonstration of soft x-ray amplification in nickel-like ions. *Phys. Rev. Lett.*, 59:2157–2160, Nov 1987.

[57] B. J. MacGowan, S. Maxon, L. B. Da Silva, D. J. Fields, C. J. Keane, D. L. Matthews, A. L. Osterheld, J. H. Scofield, G. Shimkaveg, and G. F. Stone. Demonstration of x-ray amplifiers near the carbon K edge. *Phys. Rev. Lett.*, 65:420–423, Jul 1990.

[58] B. J. MacGowan, L. B. Da Silva, D. J. Fields, C. J. Keane, J. A. Koch, R. A. London, D. L. Matthews, S. Maxon, S. Mrowka, A. L. Osterheld, J. H. Scofield, G. Shimkaveg, J. E. Trebes, and R. S. Walling. Short wavelength x-ray laser research at the Lawrence Livermore National Laboratory. *Physics of Fluids B: Plasma Physics*, 4(7):2326–2337, 1992.

[59] Richard A. London. Beam optics of exploding foil plasma x-ray lasers. *The Physics of Fluids*, 31(1):184–192, 1988.

[60] Joseph Nilsen, Brian J. MacGowan, Luiz B. Da Silva, and Juan C. Moreno. Prepulse technique for producing low-Z Ne-like x-ray lasers. *Phys. Rev. A*, 48:4682–4685, Dec 1993.

[61] Yurii V Afanas'ev and V N Shlyaptsev. Formation of a population inversion of transitions in Ne-like ions in steady-state and transient plasmas. *Soviet Journal of Quantum Electronics*, 19(12):1606–1612, dec 1989.

[62] P. V. Nickles, V. N. Shlyaptsev, M. Kalachnikov, M. Schnürer, I. Will, and W. Sandner. Short Pulse X-ray Laser at 32.6 nm Based on Transient Gain in Ne-like Titanium. *Phys. Rev. Lett.*, 78:2748–2751, Apr 1997.

[63] T. Boehly, M. Russotto, R. S. Craxton, R. Epstein, B. Yaakobi, L. B. Da Silva, J. Nilsen, E. A. Chandler, D. J. Fields, B. J. MacGowan, D. L. Matthews, J. H. Scofield, and G. Shimkaveg. Demonstration of a narrow-divergence x-ray laser in neonlike titanium. *Phys. Rev. A*, 42:6962–6965, Dec 1990.

[64] Roisin Keenan, James Dunn, Vyacheslav N Shlyaptsev, Raymond F Smith, Pravesh K Patel, and Dwight F Price. Efficient pumping schemes for high average brightness collisional x-ray lasers. In *Soft X-Ray Lasers and Applications V*, volume 5197, pages 213–221, 2003.

[65] R. Keenan, J. Dunn, P. K. Patel, D. F. Price, R. F. Smith, and V. N. Shlyaptsev. High-Repetition-Rate Grazing-Incidence Pumped X-Ray Laser Operating at 18.9 nm. *Phys. Rev. Lett.*, 94:103901, Mar 2005.

[66] B. M. Luther, Y. Wang, M. A. Larotonda, D. Alessi, M. Berrill, M. C. Marconi, J. J. Rocca, and V. N. Shlyaptsev. Saturated high-repetition-rate 18.9-nm tabletop laser in nickellike molybdenum. *Opt. Lett.*, 30(2):165–167, Jan 2005.

[67] Y. Wang, M. A. Larotonda, B. M. Luther, D. Alessi, M. Berrill, V. N. Shlyaptsev, and J. J. Rocca. Demonstration of high-repetition-rate tabletop soft-x-ray lasers with saturated output at wavelengths down to 13.9 nm and gain down to 10.9 nm. *Phys. Rev. A*, 72:053807, Nov 2005.

[68] D. Alessi, B. M. Luther, Y. Wang, M. A. Larotonda, M. Berrill, and J. J. Rocca. High repetition rate operation of saturated table-top soft x-ray lasers in transitions of neon-like ions near 30 nm. *Opt. Express*, 13(6):2093–2098, Mar 2005.

[69] JJ Rocca, Y Wang, MA Larotonda, BM Luther, M Berrill, and D Alessi. Saturated 13.2 nm high-repetition-rate laser in nickellike cadmium. *Optics Letters*, 30(19):2581–2583, 2005.

[70] D. H. Martz, D. Alessi, B. M. Luther, Y. Wang, D. Kemp, M. Berrill, and J. J. Rocca. High-energy 13.9 nm table-top soft-x-ray laser at 2.5 Hz repetition rate excited by a slab-pumped Ti: sapphire laser. *Opt. Lett.*, 35(10):1632–1634, May 2010.

[71] D. Alessi, D. H. Martz, Y. Wang, M. Berrill, B. M. Luther, and J. J. Rocca. Gain-saturated 10.9 nm tabletop laser operating at 1 Hz repetition rate. *Opt. Lett.*, 35(3):414–416, Feb 2010.

[72] D. Alessi, Y. Wang, B. M. Luther, L. Yin, D. H. Martz, M. R. Woolston, Y. Liu, M. Berrill, and J. J. Rocca. Efficient Excitation of Gain-Saturated Sub-9-nm-Wavelength Tabletop Soft-X-Ray Lasers and Lasing Down to 7.36 nm. *Phys. Rev. X*, 1:021023, Dec 2011.

[73] F. Pedaci, Y. Wang, M. Berrill, B. Luther, E. Granados, and J. J. Rocca. Highly coherent injection-seeded 13.2 nm tabletop soft x-ray laser. *Opt. Lett.*, 33(5):491–493, Mar 2008.

[74] Y. Wang, E. Granados, F. Pedaci, D. Alessi, B. Luther, M. Berrill, and J. J. Rocca. Phase-coherent, injection-seeded, table-top soft-X-ray lasers at 18.9 nm and 13.9 nm. *Nature Photonics*, 2:94–98, 01 2008.

[75] Y. Wang, E. Granados, M. A. Larotonda, M. Berrill, B. M. Luther, D. Patel, C. S. Menoni, and J. J. Rocca. High-Brightness Injection-Seeded Soft-X-Ray-Laser Amplifier Using a Solid Target. *Phys. Rev. Lett.*, 97:123901, Sep 2006.

[76] Courtney A. Brewer, Fernando Brizuela, Przemyslaw Wachulak, Dale H. Martz, Weilun Chao, Erik H. Anderson, David T. Attwood, Alexander V. Vinogradov, Igor A. Artyukov, Alexander G. Ponomareko, Valeriy V. Kondratenko, Mario C. Marconi, Jorge J. Rocca, and Carmen S. Menoni. Single-shot extreme ultraviolet laser imaging of nanostructures with wavelength resolution. *Opt. Lett.*, 33(5):518–520, Mar 2008.

[77] Fernando Brizuela, Sergio Carbajo, Anne Sakdinawat, David Alessi, Dale H. Martz, Yong Wang, Bradley Luther, Kenneth A. Goldberg, Iacopo Mochi, David T. Attwood, Bruno La Fontaine, Jorge J. Rocca, and Carmen S. Menoni. Extreme ultraviolet laser-based table-top aerial image metrology of lithographic masks. *Opt. Express*, 18(14):14467–14473, Jul 2010.

[78] Weilun Chao, Bruce D. Harteneck, J. Alexander Liddle, Erik H. Anderson, and David T. Attwood. Soft X-ray microscopy at a spatial resolution better than 15 nm. *Nature*, 435(7046):1210–1213, 2005.

[79] J. Filevich, K. Kanizay, M. C. Marconi, J. L. A. Chilla, and J. J. Rocca. Dense plasma diagnostics with an amplitude-division soft-x-ray laser interferometer based on diffraction gratings. *Opt. Lett.*, 25(5):356–358, Mar 2000.

[80] Mark E. Siemens, Qing Li, Margaret M. Murnane, Henry C. Kapteyn, Ronggui Yang, Erik H. Anderson, and Keith A. Nelson. High-frequency surface acoustic wave propagation in nanostructures characterized by coherent extreme ultraviolet beams. *Applied Physics Letters*, 94(9):093103, 2009.

[81] P. W. Wachulak, M. G. Capeluto, M. C. Marconi, C. S. Menoni, and J. J. Rocca. Patterning of nano-scale arrays by table-top extreme ultraviolet laser interferometric lithography. *Opt. Express*, 15(6):3465–3469, Mar 2007.

[82] P. Wachulak, M. Grisham, S. Heinbuch, D. Martz, W. Rockward, D. Hill, J. J. Rocca, C. S. Menoni, E. Anderson, and M. Marconi. Interferometric lithography with an amplitude division interferometer and a desktop extreme ultraviolet laser. *J. Opt. Soc. Am. B*, 25(7):B104–B107, Jul 2008.

[83] H. Bravo, B. T. Szapiro, P. W. Wachulak, M. C. Marconi, W. Chao, E. H. Anderson, C. S. Menoni, and J. J. Rocca. Demonstration of Nanomachining With Focused Extreme Ultraviolet Laser Beams. *IEEE Journal of Selected Topics in Quantum Electronics*, 18(1):443–448, Jan 2012.

[84] Brendan A. Reagan, Wei Li, Lukasz Urbanski, Keith A. Wernsing, Chase Salsbury, Cory Baumgarten, Mario C. Marconi, Carmen. S. Menoni, and Jorge J. Rocca. Hour-long continuous operation of a tabletop soft x-ray laser at 50-100 Hz repetition rate. *Opt. Express*, 21(23):28380–28386, Nov 2013.

[85] Xiaoming Zeng, Kainan Zhou, Yanlei Zuo, Qihua Zhu, Jingqin Su, Xiao Wang, Xiaodong Wang, Xiaojun Huang, Xuejun Jiang, Dongbin Jiang, Yi Guo, Na Xie, Song Zhou, Zhaohui

Wu, Jie Mu, Hao Peng, and Feng Jing. Multi-petawatt laser facility fully based on optical parametric chirped-pulse amplification. *Opt. Lett.*, 42(10):2014–2017, May 2017.

[86] Gilles Chériaux, Erhard Gaul, Roman Antipenkov, Ted Borger, Jonathan Tyler Green, František Batysta, Gavin Friedman, Axel Jochmann, Daniel Kramer, Bedrich Rus, et al. kJ-10 PW class laser system at 1 shot a minute (Conference Presentation). In *High Power Lasers for Fusion Research V*, volume 10898, page 1089806. International Society for Optics and Photonics, 2019.

[87] Hanieh Fattahi, Helena G. Barros, Martin Gorjan, Thomas Nubbemeyer, Bidoor Alsaif, Catherine Y. Teisset, Marcel Schultze, Stephan Prinz, Matthias Haefner, Moritz Ueffing, Ayman Alismail, Lénárd Vámosrd Vámos, Alexander Schwarz, Oleg Pronin, Jonathan Brons, Xiao Tao Geng, Gunnar Arisholm, Marcelo Ciappina, Vladislav S. Yakovlev, Dong-Eon Kim, Abdallah M. Azzeer, Nicholas Karpowicz, Dirk Sutter, Zsuzsanna Major, Thomas Metzger, and Ferenc Krausz. Third-generation femtosecond technology. *Optica*, 1(1):45–63, Jul 2014.

[88] M.D. Fayer. Dynamics of liquids, molecules, and proteins measured with ultrafast 2D IR vibrational echo chemical exchange spectroscopy. *Annual Review of Physical Chemistry*, 60(1):21–38, 2009. PMID: 18851709.

[89] Bradley M. Luther, Kathryn M. Tracy, Michael Gerrity, Susannah Brown, and Amber T. Krummel. 2D IR spectroscopy at 100 kHz utilizing a Mid-IR OPCPA laser source. *Opt. Express*, 24(4):4117–4127, Feb 2016.

[90] Zsuzsanna Heiner, Li Wang, Valentin Petrov, and Mark Mero. Broadband vibrational sum-frequency generation spectrometer at 100 kHz in the 950-1750 cm^{-1} spectral range utilizing a $LiGaS_2$ optical parametric amplifier. *Opt. Express*, 27(11):15289–15297, May 2019.

[91] N. Bigler, J. Pupeikis, S. Hrisafov, L. Gallmann, C. R. Phillips, and U. Keller. High-power OPCPA generating 1.7 cycle pulses at 2.5 μm. *Opt. Express*, 26(20):26750–26757, Oct 2018.

[92] B. W. Mayer, C. R. Phillips, L. Gallmann, and U. Keller. Mid-infrared pulse generation via achromatic quasi-phase-matched OPCPA. *Opt. Express*, 22(17):20798–20808, Aug 2014.

[93] Tenio Popmintchev, Ming-Chang Chen, Dimitar Popmintchev, Paul Arpin, Susannah Brown, Skirmantas Ališauskas, Giedrius Andriukaitis, Tadas Balčiunas, Oliver D. Mücke, Audrius Pugzlys, Andrius Baltuška, Bonggu Shim, Samuel E. Schrauth, Alexander Gaeta, Carlos Hernández-García, Luis Plaja, Andreas Becker, Agnieszka Jaron-Becker, Margaret M. Murnane, and Henry C. Kapteyn. Bright Coherent Ultrahigh Harmonics in the keV X-ray Regime from Mid-Infrared Femtosecond Lasers. *Science*, 336(6086):1287–1291, 2012.

[94] T. Tajima and J. M. Dawson. Laser electron accelerator. *Phys. Rev. Lett.*, 43:267–270, Jul 1979.

[95] C. Joshi. Laser-Driven Plasma Accelerators Operating in the Self-Guided, Blowout Regime. *IEEE Transactions on Plasma Science*, 45(12):3134–3146, Dec 2017.

[96] A. Pukhov and J. Meyer-ter Vehn. Laser wake field acceleration: the highly non-linear broken-wave regime. *Applied Physics B*, 74(4):355–361, Apr 2002.

[97] A. J. Gonsalves, K. Nakamura, J. Daniels, C. Benedetti, C. Pieronek, T. C. H. de Raadt, S. Steinke, J. H. Bin, S. S. Bulanov, J. van Tilborg, C. G. R. Geddes, C. B. Schroeder, Cs. Tóth, E. Esarey, K. Swanson, L. Fan-Chiang, G. Bagdasarov, N. Bobrova, V. Gasilov, G. Korn, P. Sasorov, and W. P. Leemans. Petawatt Laser Guiding and Electron Beam Acceleration to 8 GeV in a Laser-Heated Capillary Discharge Waveguide. *Phys. Rev. Lett.*, 122:084801, Feb 2019.

[98] W. Leemans. Report of Workshop on Laser Technology for k-BELLA and Beyond. Technical report, Lawrence Berkeley National Laboratory, 2017.

[99] E Sistrunk, DA Alessi, A Bayramian, K Chesnut, A Erlandson, TC Galvin, D Gibson, H Nguyen, B Reagan, K Schaffers, et al. Laser Technology Development for High Peak

Power Lasers Achieving Kilowatt Average Power and Beyond. In *Short-pulse High-energy Lasers and Ultrafast Optical Technologies*, volume 11034, page 1103407. International Society for Optics and Photonics, 2019.

[100] A. Klenke, M. Müller, H. Stark, F. Stutzki, C. Hupel, T. Schreiber, A. Tünnermann, and J. Limpert. Coherently combined 16-channel multicore fiber laser system. *Opt. Lett.*, 43(7):1519–1522, Apr 2018.

[101] J. R. Klauder, A. C. Price, S. Darlington, and W. J. Albersheim. The Theory and Design of Chirp Radars. *Bell System Technical Journal*, 39(4):745–808, 1960.

[102] John Kerr LL.D. Xl. a new relation between electricity and light: Dielectrified media birefringent. *The London, Edinburgh, and Dublin Philosophical Magazine and Journal of Science*, 50(332):337–348, 1875.

[103] R. Ell, U. Morgner, F. X. Kärtner, J. G. Fujimoto, E. P. Ippen, V. Scheuer, G. Angelow, T. Tschudi, M. J. Lederer, A. Boiko, and B. Luther-Davies. Generation of 5-fs pulses and octave-spanning spectra directly from a Ti:sapphire laser. *Opt. Lett.*, 26(6):373–375, Mar 2001.

[104] Treacy E. Optical pulse compression with diffraction gratings. *IEEE Journal of Quantum Electronics*, 5(9):454–458, Septmeber 1969.

[105] E.B. Treacy. Compression of picosecond light pulses. *Physics Letters A*, 28(1):34 – 35, 1968.

[106] O. Martinez. 3000 times grating compressor with positive group velocity dispersion: Application to fiber compensation in 1.3-1.6 μm region. *IEEE Journal of Quantum Electronics*, 23(1):59–64, January 1987.

[107] Walter Koechner. *Solid-State Laser Engineering*. Springer, 2006.

[108] S. Yarema and D. Milam. Gain saturation in phosphate laser glasses. *IEEE Journal of Quantum Electronics*, 18(11):1941–1946, Nov 1982.

[109] M.J. Weber. Science and technology of laser glass. *Journal of Non-Crystalline Solids*, 123(1):208 – 222, 1990. XVth International Congress on Glass.

[110] W. Simmons, J. Hunt, and W. Warren. Light propagation through large laser systems. *IEEE Journal of Quantum Electronics*, 17(9):1727–1744, Sep 1981.

[111] W. Krupke. Induced-emission cross sections in neodymium laser glasses. *IEEE Journal of Quantum Electronics*, 10(4):450–457, April 1974.

[112] M Kanskar, T Earles, TJ Goodnough, E Stiers, D Botez, and LJ Mawst. 73% CW power conversion efficiency at 50 W from 970 nm diode laser bars. *Electronics Letters*, 41(5):245–247, 2005.

[113] Sébastien Chénais, Frédéric Druon, Sébastien Forget, François Balembois, and Patrick Georges. On thermal effects in solid-state lasers: The case of ytterbium-doped materials. *Progress in quantum electronics*, 30(4):89–153, 2006.

[114] R. L. Aggarwal, D. J. Ripin, J. R. Ochoa, and T. Y. Fan. Measurement of thermo-optic properties of Y3Al5O12, Lu3Al5O12, YAIO3, LiYF4, LiLuF4, BaY2F8, KGd(WO4)2, and KY(WO4)2 laser crystals in the 80–300 K temperature range. *Journal of Applied Physics*, 98(10):103514, 2005.

[115] N. V. Kuleshov, A. A. Lagatsky, A. V. Podlipensky, V. P. Mikhailov, and G. Huber. Pulsed laser operation of Yb-doped KY(WO4)2 and KGd(WO4)2. *Opt. Lett.*, 22(17):1317–1319, Sep 1997.

[116] K. Ogawa, Y. Akahane, M. Aoyama, K. Tsuji, S. Tokita, J. Kawanaka, H. Nishioka, and K. Yamakawa. Multi-millijoule, diode-pumped, cryogenically-cooled Yb:KY(WO4)2 chirped-pulse regenerative amplifier. *Opt. Express*, 15(14):8598–8602, Jul 2007.

[117] Hsiao hua Liu, John Nees, and Gérard Mourou. Directly diode-pumped Yb:KY(WO4)2 regenerative amplifiers. *Opt. Lett.*, 27(9):722–724, May 2002.

[118] Anthony E. Siegman. *Lasers*. University Science Books, 1986.

[119] G. Machinet, P. Sevillano, F. Guichard, R. Dubrasquet, P. Camy, J.-L. Doualan, R. Moncorgé, P. Georges, F. Druon, D. Descamps, and E. Cormier. High-brightness fiber laser-pumped 68 fs–2.3 W Kerr-lens mode-locked Yb:CaF2 oscillator. *Opt. Lett.*, 38(20):4008–4010, Oct 2013.

[120] A. Pugžlys, G. Andriukaitis, A. Baltuška, L. Su, J. Xu, H. Li, R. Li, W. J. Lai, P. B. Phua, A. Marcinkevičius, M. E. Fermann, L. Giniūnas, R. Danielius, and S. Ališauskas. Multi-mJ, 200-fs, cw-pumped, cryogenically cooled, Yb,Na:CaF2 amplifier. *Opt. Lett.*, 34(13):2075–2077, Jul 2009.

[121] F. Brunner, T. Südmeyer, E. Innerhofer, F. Morier-Genoud, R. Paschotta, V. E. Kisel, V. G. Shcherbitsky, N. V. Kuleshov, J. Gao, K. Contag, A. Giesen, and U. Keller. 240-fs pulses with 22-W average power from a mode-locked thin-disk Yb:KY$(WO_4)_2$ laser. *Opt. Lett.*, 27(13):1162–1164, Jul 2002.

[122] F. Brunner, G. J. Spühler, J. Aus der Au, L. Krainer, F. Morier-Genoud, R. Paschotta, N. Lichtenstein, S. Weiss, C. Harder, A. A. Lagatsky, A. Abdolvand, N. V. Kuleshov, and U. Keller. Diode-pumped femtosecond Yb:KGd$(WO_4)_2$ laser with 1.1-W average power. *Opt. Lett.*, 25(15):1119–1121, Aug 2000.

[123] JE Geusic, HM Marcos, and LeGrand Van Uitert. Laser oscillations in Nd-doped yttrium aluminum, yttrium gallium and gadolinium garnets. *Applied Physics Letters*, 4(10):182–184, 1964.

[124] Jun Dong, Michael Bass, Yanli Mao, Peizhen Deng, and Fuxi Gan. Dependence of the Yb3+ emission cross section and lifetime on temperature and concentration in yttrium aluminum garnet. *J. Opt. Soc. Am. B*, 20(9):1975–1979, Sep 2003.

[125] Lee M Frantz and John S Nodvik. Theory of pulse propagation in a laser amplifier. *Journal of Applied Physics*, 34(8):2346–2349, 1963.

[126] J. Körner, V. Jambunathan, J. Hein, R. Seifert, M. Loeser, M. Siebold, U. Schramm, P. Sikocinski, A. Lucianetti, T. Mocek, and M. C. Kaluza. Spectroscopic characterization of Yb3+-doped laser materials at cryogenic temperatures. *Applied Physics B*, 116(1):75–81, 2014.

[127] D. C. Brown, R. L. Cone, , and R. W. Equall. Yb:YAG absorption at ambient and cryogenic temperatures. *IEEE Journal of Selected Topics in Quantum Electronics*, 11(3):604–612, May 2005.

[128] A. Giesen and J. Speiser. Fifteen Years of Work on Thin-Disk Lasers: Results and Scaling Laws. *IEEE Journal of Selected Topics in Quantum Electronics*, 13(3):598–609, May 2007.

[129] Jan-Philipp Negel, André Loescher, Andreas Voss, Dominik Bauer, Dirk Sutter, Alexander Killi, Marwan Abdou Ahmed, and Thomas Graf. Ultrafast thin-disk multipass laser amplifier delivering 1.4 kW (4.7 mJ, 1030 nm) average power converted to 820 W at 515 nm and 234 W at 343 nm. *Opt. Express*, 23(16):21064–21077, Aug 2015.

[130] Knut Michel; Christian Grebing; Clemens Herkommer; Sandro Klingebiel; Peter Krötz; Stephan Prinz; Marcel Schultze; Sebastian Stark; Catherine Y. Teisset; Christoph Wandt; Thomas Metzger. High-energy ultrafast thin-disk amplifiers. In *Solid State Lasers XXVIII: Technology and Devices*, volume 10896, page 108960Y, 2019.

[131] Tso Yee Fan. Laser beam combining for high-power, high-radiance sources. *IEEE Journal of selected topics in Quantum Electronics*, 11(3):567–577, 2005.

[132] S. Szatmari and P. Simon. Interferometric multiplexing scheme for excimer amplifiers. *Optics Communications*, 98(1):181 – 192, 1993.

[133] Shian Zhou, Frank W Wise, and Dimitre G Ouzounov. Divided-pulse amplification of ultrashort pulses. *Optics letters*, 32(7):871–873, 2007.

[134] Federico Pirzio, Etienne Caracciolo, Matthias Kemnitzer, Annalisa Guandalini, Florian Kienle, Juerg Aus der Au, and Antonio Agnesi. Performance of Yb:Sc2SiO5 crystal in diode-pumped femtosecond oscillator and regenerative amplifier. *Opt. Express*, 23(10):13115–13120, May 2015.

[135] O. E. Martinez, J. P. Gordon, and R. L. Fork. Negative group-velocity dispersion using refraction. *J. Opt. Soc. Am. A*, 1(10):1003–1006, Oct 1984.

[136] H. Kogelnik. Coupled wave theory for thick hologram gratings. *The Bell System Technical Journal*, 48(9):2909–2947, Nov 1969.

[137] A. Galvanauskas, M. E. Fermann, D. Harter, K. Sugden, and I. Bennion. All-fiber femtosecond pulse amplification circuit using chirped bragg gratings. *Applied Physics Letters*, 66(9):1053–1055, 1995.

[138] Kai-Hsiu Liao, Ming-Yuan Cheng, Emilie Flecher, Vadim I. Smirnov, Leonid B. Glebov, and Almantas Galvanauskas. Large-aperture chirped volume bragg grating based fiber cpa system. *Opt. Express*, 15(8):4876–4882, Apr 2007.

[139] Raymond J Beach, Eric C Honea, Camille Bibeau, Stephen A Payne, Howard Powell, William F Krupke, and Steven B Sutton. High average power scaleable thin-disk laser. *U. S. Patent 6347109*, Feb 12, 2012.

[140] Dmitrii Kouznetsov and Jean-François Bisson. Role of undoped cap in the scaling of thin-disk lasers. *J. Opt. Soc. Am. B*, 25(3):338–345, Mar 2008.

[141] Mu Wang, Guangzhi Zhu, Xiao Zhu, Yongqian Chen, Jing Dong, Hailin Wang, and Yefeng Qian. Thickness optimization for an anti-ASE cap in a thin disk laser considering dioptric power and aberration-induced loss. *J. Opt. Soc. Am. B*, 35(3):583–592, Mar 2018.

[142] Brendan A. Reagan, Mark Berrill, Keith A. Wernsing, Cory Baumgarten, Mark Woolston, and Jorge J. Rocca. High-average-power, 100-hz-repetition-rate, tabletop soft-x-ray lasers at sub-15-nm wavelengths. *Phys. Rev. A*, 89:053820, May 2014.

[143] Brendan A. Reagan, Cory Baumgarten, Mark Berrill, Keith A. Wernsing, Mark Woolston, Lukasz Urbanski, Wei Li, Mario C. Marconi, Vyacheslav N. Slyaptsev, Carmen S. Menoni, and Jorge J. Rocca. Advances in high average power, 100 hz repetition rate table-top soft x-ray lasers. In Jorge Rocca, Carmen Menoni, and Mario Marconi, editors, *X-Ray Lasers 2014*, pages 11–19, Cham, 2016. Springer International Publishing.

[144] Russell L McCally, Jennifer Bonney-Ray, Zenaida De La Cruz, and W Richard Green. Corneal endothelial injury thresholds for exposures to 1.54 μm radiation. *Health Physics*, 92(3):205–211, March 2007.

[145] Drew Schiltz. Advancements in the optical damage resistance of ion beam sputter deposited interference coatings for high energy lasers. Master's thesis, Colorado State Univeristy, 2015.

[146] E. G. Gamaly, A. V. Rode, B. Luther-Davies, and V. T. Tikhonchuk. Ablation of solids by femtosecond lasers: Ablation mechanism and ablation thresholds for metals and dielectrics. *Physics of Plasmas*, 9(3):949–957, 2002.

[147] B. C. Stuart, M. D. Feit, A. M. Rubenchik, B. W. Shore, and M. D. Perry. Laser-induced damage in dielectrics with nanosecond to subpicosecond pulses. *Phys. Rev. Lett.*, 74:2248–2251, Mar 1995.

[148] A.P. Joglekar, H. Liu, G.J. Spooner, E. Meyhöfer, G. Mourou, and A.J. Hunt. A study of the deterministic character of optical damage by femtosecond laser pulses and applications to nanomachining. *Applied Physics B*, 77(1):25–30, Aug 2003.

[149] D. M. Simanovskii, H. A. Schwettman, H. Lee, and A. J. Welch. Midinfrared optical breakdown in transparent dielectrics. *Phys. Rev. Lett.*, 91:107601, Sep 2003.

[150] Robert W Boyd. *Nonlinear optics*. Elsevier, 2003.

[151] H.J. Liu, G.F. Chen, W. Zhao, Y.S. Wang, T. Wang, and S.H. Zhao. Phase matching analysis of noncollinear optical parametric process in nonlinear anisotropic crystals. *Optics Communications*, 197(4):507 – 514, 2001.

[152] D. Kraemer, R. Hua, M. L. Cowan, K. Franjic, and R. J. Dwayne Miller. Ultrafast noncollinear optical parametric chirped pulse amplification in KTiOAsO4. *Opt. Lett.*, 31(7):981–983, Apr 2006.

[153] Audrius Dubietis, Gintaras Tamošauskas, Rosvaldas Šuminas, Vytautas Jukna, and Arnaud Couairon. Ultrafast supercontinuum generation in bulk condensed media (invited review). *arXiv preprint arXiv:1706.04356*, 2017.

[154] Alexander L. Gaeta. Catastrophic collapse of ultrashort pulses. *Phys. Rev. Lett.*, 84:3582–3585, Apr 2000.

[155] Gadi Fibich and Alexander L. Gaeta. Critical power for self-focusing in bulk media and in hollow waveguides. *Opt. Lett.*, 25(5):335–337, Mar 2000.

[156] F. DeMartini, C. H. Townes, T. K. Gustafson, and P. L. Kelley. Self-steepening of light pulses. *Phys. Rev.*, 164:312–323, Dec 1967.

[157] O. D. Mücke, D. Sidorov, P. Dombi, A. Pugžlys, A. Baltuška, S. Ališauskas, V. Smilgevičius, J. Pocius, L. Giniūnas, R. Danielius, and N. Forget. Scalable Yb-MOPA-driven carrier-envelope phase-stable few-cycle parametric amplifier at 1.5 μm. *Opt. Lett.*, 34(2):118–120, Jan 2009.

[158] Detlev Ristau. *Laser-Induced Damage in Optical Materials*. CRC Press, 2015.

[159] L. V. Keldysh. Ionization in the field of a strong electromagnetic wave. *Sov. Phys. JETP*, 20(5):1307–1314, 1965.

[160] B. C. Stuart, M. D. Feit, S. Herman, A. M. Rubenchik, B. W. Shore, and M. D. Perry. Nanosecond-to-femtosecond laser-induced breakdown in dielectrics. *Phys. Rev. B*, 53:1749–1761, Jan 1996.

[161] An-Chun Tien, Sterling Backus, Henry Kapteyn, Margaret Murnane, and Gérard Mourou. Short-pulse laser damage in transparent materials as a function of pulse duration. *Phys. Rev. Lett.*, 82:3883–3886, May 1999.

[162] Xuchuan Shang, Rongzhu Zhang, and Ping Ma. Analysis of avalanche mechanisms in short-pulses laser-induced damage. *Optics & Laser Technology*, 42(1):243–246, 2010.

[163] M. Mero, J. Liu, W. Rudolph, D. Ristau, and K. Starke. Scaling laws of femtosecond laser pulse induced breakdown in oxide films. *Phys. Rev. B*, 71:115109, Mar 2005.

[164] Chris B Schaffer, André Brodeur, and Eric Mazur. Laser-induced breakdown and damage in bulk transparent materials induced by tightly focused femtosecond laser pulses. *Measurement Science and Technology*, 12(11):1784–1794, oct 2001.